

12-15-2014

# Fabrication and Characterization of Novel Electrodes for Solid Oxide Fuel Cell for Efficient Energy Conversion

Yu Chen

*University of South Carolina - Columbia*

Follow this and additional works at: <https://scholarcommons.sc.edu/etd>

 Part of the [Mechanical Engineering Commons](#)

---

## Recommended Citation

Chen, Y.(2014). *Fabrication and Characterization of Novel Electrodes for Solid Oxide Fuel Cell for Efficient Energy Conversion*. (Doctoral dissertation). Retrieved from <https://scholarcommons.sc.edu/etd/2954>

This Open Access Dissertation is brought to you by Scholar Commons. It has been accepted for inclusion in Theses and Dissertations by an authorized administrator of Scholar Commons. For more information, please contact [dillarda@mailbox.sc.edu](mailto:dillarda@mailbox.sc.edu).

FABRICATION AND CHARACTERIZATION OF NOVEL  
ELECTRODES FOR SOLID OXIDE FUEL CELL FOR EFFICIENT  
ENERGY CONVERSION

by

Yu Chen

Bachelor of Science  
Anhui University, 2007

Master of Engineering  
University of Science and Technology of China, 2010

---

Submitted in Partial Fulfillment of the Requirements

For the degree of Doctor of Philosophy in

Mechanical Engineering

College of Engineering and Computing

University of South Carolina

2014

Accepted by:

Fanglin (Frank) Chen, Major Professor

Kenneth Reifsnider, Committee Member

Prasun Majumdar, Committee Member

Kyle S. Brinkman, Committee Member

Lacy Ford, Vice Provost and Dean of Graduate Studies

© Copyright by Yu Chen, 2014  
All rights Reserved

## ACKNOWLEDGEMENTS

I would like to thank my advisor, Dr. Fanglin (Frank) Chen, who led me to the solid oxide fuel cell area and has provided me his knowledge, experience and insightful guidance all while encouraging me with unwavering support before and during my doctoral study. I would also like to thank my thesis committee, Dr. Kenneth Reifsnider, Dr. Prasun Majumdar, and Dr. Kyle Brinkman, for their invaluable suggestion and continuous support during my PhD study. Financial supports from National Science Foundation (award no. 1210792), NASA EPSCoR (Award Number NNX 10AN33A), the SC Space Grant Consortium, the HeteroFoam Center (Award Number DE-SC0001061), the 973 Project (2012CB215404) and the National Natural Science Foundation of China NSCF (51261120378) are greatly appreciated.

I would also like to thank the colleagues for their assistance and contributions to my work. It is a great time to spend my study here with friends who were or are at the Department of Mechanical Engineering: Fei Zhao, Qiang Liu, Guoliang Xiao, Chao Jin, Daan Cui, Jacob Bunch, Jeffery Baker, Shumin Fang, Sirikanda Nuansaeng, Lei Zhang, Chenghao Yang, Xihui Dong, Siwei Wang, Lingling Zhang, Cong Ren, Zhibin Yang, Tong Liu, Yao Wang, Libin Lei, and other friends in the Horizon Building. Special appreciation is given to Yanxiang Zhang and Ye Lin for their efforts on calculation and TEM analysis.

Finally, I would like to express my great gratitude to my wife and my little girl for their help, understanding and support. I would also like to thank my parents for their selfless and endless support.

## ABSTRACT

Solid oxide fuel cells (SOFCs) have been considered as one of the most promising technologies for future energy conversion since they can in principle be operated with fuels ranging from H<sub>2</sub> to any hydrocarbon fuel. However, the system cost and coking (when using hydrocarbon as fuel) issues for the state-of-art electrode materials/designs often limit their further application. The objective of this Ph.D dissertation is aiming at overcoming these problems and accelerating SOFC commercialization.

One approach to cost reduction is lowering the SOFC operating temperature to below 800 or even 600 °C, so that inexpensive materials can be used and quick start-up and SOFC durability can be improved. However, the overall electrochemical performance of an SOFC system will significantly decrease with a reduced operating temperature due to increased ohmic resistance of the electrolyte and polarization resistances of the electrode reactions. Ohmic resistance could be reduced by decreasing thickness of the electrolyte or using electrolyte with high ionic conductivity. Polarization resistance could be reduced by applying novel microstructured electrodes. Here we have fabricated a novel hierarchically oriented porous anode-supported solid oxide fuel cell with thin Gd<sub>0.1</sub>Ce<sub>0.9</sub>O<sub>2</sub> (GDC) electrolyte by freeze-drying tape-casting and drop-coating. Three dimensional (3D) X-ray microscopy and subsequent analysis have demonstrated that the substrate has a graded open and straight pore/channel structure. The diameter of pore size

on the bottom and top surface, porosity distribution along thickness direction and tortuosity factor have been determined by SEM and calculation with help of Matlab. The novel microstructure is expected to facilitate gas diffusion in the anode during fuel cell operation. The cell performance at low temperature ranging from 500-600 °C has been evaluated systematically. SOFCs with such Ni-GDC anode, GDC film (30 μm) electrolyte, and La<sub>0.6</sub>Sr<sub>0.4</sub>Co<sub>0.2</sub>Fe<sub>0.8</sub>O<sub>3</sub>-GDC (LSCF-GDC) cathode show significantly enhanced cell power output of 1.021 W cm<sup>-2</sup> at 600 °C using H<sub>2</sub> as fuel and ambient air as oxidant.

Since cathode has been the center of the focus in the electrode development largely because oxygen reduction is more difficult to activate in SOFCs operating at commercially relevant temperature. Consequently, it is critically important to develop new cathode material or novel cathode microstructures with low polarization loss to maintain sufficient high electrochemical activity to enable SOFC operating at temperatures of below 600 °C. We have prepared SOFCs with hierarchically porous nano cathode network by a novel vacuum-free infiltration and subsequent freeze-drying combustion. The straight open GDC cathode skeleton and NiO-GDC anode substrate prepared by freeze-drying tape-casting facilitate mass transport while the nano cathode catalyst promotes the electrochemical reactions. The cell with straight open electrodes and hierarchically porous cathode network demonstrates a maximum power density of 0.65 Wcm<sup>-2</sup> at 500 °C and impressive stability for more than 500 h at 400 °C using H<sub>2</sub> as fuel and ambient air as oxidant. The simple and cost-effective fabrication process is expected to significantly impact the SOFC operability and accelerate its commercialization.

Another advantage of SOFCs compared with other energy conversion systems is the capability of direct utilization of hydrocarbon fuel. However, carbon species adsorb strongly on Ni surface and thus blocks the active site for electrochemical reactions, resulting in rapid performance degradation. In this research, we present an innovative and simple design for enhancing the coking resistance of the conventional nickel cermet SOFC anode. A thin nanoscale samaria doped ceria (SDC) catalyst layer has been deposited on the wall surface of the Ni-yttria-stabilized zirconia (Ni-YSZ) anode internal gas diffusion channel (5-200  $\mu\text{m}$  in size) via a combination of freeze-drying tape-casting and vacuum-free infiltration. The efficiency for catalyst infiltration has been significantly improved by using hierarchically porous anode structure with open and straight channels. Single cells with nanoscale SDC layer show very stable cell performance and a peak power density of  $0.65 \text{ Wcm}^{-2}$  at  $800 \text{ }^\circ\text{C}$  using methane as fuel, more than one order of magnitude higher than that for the cells using Ni-YSZ anode without the SDC catalyst layer. High resolution transmission electron microscopy (HRTEM) analysis indicates that nanoscale SDC layer can prevent the formation or growth of nickel carbide (onset of coking).

## TABLE OF CONTENTS

ACKNOWLEDGEMENTS .....	iii
ABSTRACT .....	v
LIST OF TABLES .....	x
LIST OF FIGURES .....	xi
CHAPTER 1 INTRODUCTION .....	1
1.1 BACKGROUND ABOUT SOLID OXIDE FUEL CELLS .....	1
1.2 POLARIZATION LOSS.....	6
1.3 PROGRESS OF SOFCS WITH Ni-BASED ANODES OPERATING WITH METHANE FUELS .....	11
1.4 OBJECTIVE AND STRUCTURE OF THIS DISSERTATION.....	15
CHAPTER 2 FABRICATION AND CHARACTERIZATION OF NOVEL FUNCTIONALITY GRADED POROUS ELECTRODE FOR INTERMEDIATE TEMPERATURE SOLID OXIDE FUEL CELL BY FREEZE-DRYING TAPE- CASTING .....	17
2.1 BACKGROUND .....	17
2.2 EXPERIMENTAL .....	21
2.3 RESULTS AND DISCUSSION .....	23
2.4 SUMMARY .....	37
CHAPTER 3 HIERARCHICALLY ORIENTED MACROPOROUS ANODE- SUPPORTED SOLID OXIDE FUEL CELL WITH THIN CERIA ELECTROLYTE FILM.....	39
3.1 BACKGROUND .....	39
3.2 EXPERIMENTAL SECTION .....	41

3.3 RESULTS AND DISCUSSION .....	43
3.4 CONCLUSIONS.....	52
CHAPTER 4 LOW TEMPERATURE SOLID OXIDE FUEL CELLS WITH HIERARCHICALLY POROUS CATHODE NANO-NETWORK.....	54
4.1 BACKGROUND .....	54
4.2 EXPERIMENTAL.....	56
4.3 RESULTS AND DISCUSSION .....	59
4.4 CONCLUSIONS.....	72
CHAPTER 5 DIRECT-METHANE SOLID OXIDE FUEL CELL WITH HIERARCHICALLY POROUS Ni-BASED ANODE DEPOSITED WITH NANO CATALYST LAYER .....	73
5.1 BACKGROUND .....	73
5.2 EXPERIMENTAL.....	76
5.3 RESULTS AND DISCUSSION .....	77
5.4 CONCLUSIONS.....	95
FUTURE WORK.....	96
REFERENCES .....	100

## LIST OF TABLES

Table 1.1 Features of single cell configurations[9] .....	5
Table 2.1 Tortuosity factors of solid and pore phases along z, y, x axes. Five subdomains with a size of $1750\mu\text{m}\times 1750\mu\text{m}\times 500\mu\text{m}$ are extracted randomly from the entire domain for use of calculation.....	34
Table 3.1 Tortuosity factors of pore phases along z, y, x axes. Three subdomains with a size of $896\mu\text{m}\times 896\mu\text{m}\times 550\mu\text{m}$ are extracted randomly from the scanning regions for calculation. ....	47
Table 3.2 Comparison of maximum cell power density and interfacial polarization resistance measured at $600\text{ }^{\circ}\text{C}$ of anode supported cells based on GDC or $\text{Sm}_{0.2}\text{Ce}_{0.8}\text{O}_2$ (SDC) thin film electrolytes.....	51
Table 4.1 Peak power density ( $P_{max}$ ) and polarization resistance ( $R_p$ ) at $500\text{ }^{\circ}\text{C}$ for SOFCs with hydrogen as fuel.....	61

## LIST OF FIGURES

Figure 1.1 Summary of fuel cell types[5] .....	1
Figure 1.2 Working principle of SOFC[7].....	2
Figure 1.3 Temperature dependence of the electrical conductivity of the $ZrO_2$ - $M_2O_3$ systems. 9SSZ: 9 mol% $Sc_2O_3$ - $ZrO_2$ , 9YbSZ: 9 mol% $Yb_2O_3$ - $ZrO_2$ , 9YSZ: 9 mol% $Y_2O_3$ - $ZrO_2$ [8]. .....	4
Figure 1.4 Calculated concentration polarization of anode-supported solid oxide fuel cell[10] .....	8
Figure 1.5 Calculated activation polarization of solid oxide fuel cell[10] .....	9
Figure 1.6 Typical polarization curve for solid oxide fuel cells .....	10
Figure 1.7 Models of $CH_4$ decomposition and elimination of carbon deposition by applied voltage over Ni-YSZ interface[27]. .....	13
Figure 1.8 Schematic diagram of a SOFC with a catalyst layer during operation on $CH_4$ - $O_2$ gas mixture.....	14
Figure 1.9 Schematic illustration of an anode microstructure coated with SDC[33]. .....	15
Figure 2.1 Cross-section scanning electron micrograph (a) and surface view (b) of 30 vol% solids YSZ oxide aqueous freeze-tape-casted substrate frozen at $-50\text{ }^\circ\text{C}$ [42]. .....	19
Figure 2.2 Modified freeze-tape casting apparatus[42]. .....	20

Figure 2.3 Cross-section SEM images of Ni-YSZ substrates with solid loading of: (a) 15 vol%, (b) 20 vol% and (c) 25 vol%; and (d) the pore size distribution for respective substrate. ....	23
Figure 2.4 Cross-section SEM images for Ni-YSZ substrates frozen at (a) -70 °C, (b) -60 °C and (c) -50 °C; and (d) pore size distributions for respective substrate. ....	25
Figure 2.5 Cross-section SEM images for Ni-YSZ substrate prepare from different pulling rate: (a) 36 mm min <sup>-1</sup> ; (b) 48 mm min <sup>-1</sup> and (c) 60 mm min <sup>-1</sup> ; and (d) pore size distributions for respective substrate. ....	26
Figure 2.6 Reconstructed 3D microstructure of porous Ni-YSZ electrode. The bright/dark region represents solid/pore phase. ....	28
Figure 2.7 Gray level histogram of the 3D XCT data.....	29
Figure 2.8 Distributions of local porosity and inner surface area along z axis. Error bar represents standard deviation.....	30
Figure 2.9 Visualization of the field $\psi$ distribution in a 3D subdomain extracted from the entire domain. a, b, and c show the field distributions in the pore phase network, when the network is enforced a constant potential difference on the boundaries of z axis, y axis, and x axis, respectively. Similarly, d, e, and f show the field distributions in the solid phase network (Ni+YSZ) along z axis, y axis, and x axis, respectively. Further, tortuosity factors of solid phase and pore phase along z, y, x axes can be calculated by using the field distributions. Colors from red to blue proportionally represent the field potential from high to low.....	32
Figure 2.10 Streamlines of the field flux $-\sigma_0 \nabla \psi$ in the 3D subdomain shown in Fig. 4. a, b, and c show the streamlines in the pore phase network, when the network is enforced a constant potential difference on the boundaries of z axis, y axis, and x axis, respectively. Similarly, d, e, and f show the streamlines in the solid phase network (Ni+YSZ), when the network is enforced a constant potential difference on the boundaries of z axis, y axis, and x axis, respectively. ....	32
Figure 2.11 SEM images of cross section view of the cell (a) and (b), and surface view of electrolyte YSZ (c).....	35
Figure 2.12 (a) <i>IV</i> and <i>IP</i> curves of cell measured at different temperatures using hydrogen as fuel and ambient air as oxidant; (b) Comparison of <i>IV</i> and <i>IP</i> curves of cells prepared by either dry-pressing or freeze-tape-casting method measured at 800 °C.....	35
Figure 2.13 (a) Impedance spectra of cells tested at different temperature under open circuit conditions (b) comparison of impedance spectra of cells fabricated by either dry-pressing or freeze tape-casting method measured at 800 °C.....	36

Figure 3.1 (a) Typical cross-section view of sintered substrate made through freeze-drying tape-casting; (b) Surface view of the top part in (a); (c) Surface view of the bottom part in (a) (Bar=100  $\mu\text{m}$ ); and (d) 3-D X-ray microscopy image of the anode substrate with a dimension of 3.03mm\*3.72mm\*0.55 mm. .... 44

Figure 3.2 Re-constructed 3D microstructure images from the three different subdomains (a, b and c) of porous NiO-GDC substrates. The blue/blank regions within the 3D images represent solid/pore phases. (d) Distribution of the local porosity along z axis for the three different subdomains (a), (b) and (c). .... 46

Figure 3.3 Shrinkage of GDC film on NiO-GDC sintered at different temperatures, with NiO-GDC substrates made by either freeze-drying tape-casting or dry-pressing. Insets are surface views of GDC film on freeze-drying tape-casted substrate sintered at different temperatures. .... 48

Figure 3.4 SEM images of cross sectional views of the cell after fuel cell testing. (a) anode/electrolyte/cathode interfaces; (b) anode/electrolyte interface and (c) cathode/electrolyte interface ..... 49

Figure 4.1 (a) Typical *I-V* and *I-P* curves and (b) Electrochemical impedance spectra for the cell with hierarchically porous rough SSC-GDC cathode nano-network prepared from the FC-G method at 400, 450 and 500  $^{\circ}\text{C}$ , respectively. (c) Power density as a function of time at 400  $^{\circ}\text{C}$  for the cell with SSC-GDC cathode made from the FC-G method operated at a constant current load of 0.33  $\text{Acm}^{-2}$ . .... 60

Figure 4.2 3D X-ray microscopic image (a) for the cell consisting of anode (bottom layer), electrolyte (middle layer) and cathode (top layer) ( $a_1$ ) and cross-sectional view of X-ray microscopic image showing internal gas diffusion channel ( $a_2$ ). Reconstructed 3D image for single cell (b), SEM images for the cross-section of the cell (c), the cathode (d,e), and high resolution TEM (HRTEM) image for the surface of SSC-GDC cathode after electrochemical measurement (f). .... 63

Figure 4.3 The SSC-GDC cathodes prepared by (a) traditional combustion method without glycine as the chelating agent (TC), (b) traditional combustion method with glycine as the chelating agent (TC-G), (c) freeze-drying combustion without glycine as the chelating agent (FC), and (d) freeze-drying combustion with glycine as the chelating agent (FC-G). Insets are enlarged SSC particles views respectively. .... 63

Figure 4.4 Distributions of a general field within the 3D pore domains of anode (a) and cathode (b). Colors scale with the potential of the field. .... 64

Figure 4.5 (a) XRD pattern for SSC-GDC electrode heat-treated at 1000  $^{\circ}\text{C}$  and (b) Selected area electron diffraction (SAED) pattern for the SSC-GDC cathode particles heat-treated at 1000  $^{\circ}\text{C}$ . .... 65

Figure 4.6 (a) XRD pattern, (b) low magnification SEM, (c) high magnification SEM and (d) Bright field (BF) TEM and (e) High resolution TEM (HRTEM) for the SSC powder prepared by freeze-drying combustion method. The powder was heat-treated at 1000 °C for 2 h. .... 67

Figure 4.7 XRD patterns for SSC powders prepared by (a) traditional combustion without glycine as the chelating agent (TC), (b) traditional combustion with glycine as the chelating agent (TC-G), (c) freeze-drying combustion without glycine as the chelating agent (FC) and (d) freeze-drying combustion with glycine as the chelating agent (FC-G). The pattern (A) is from 20 to 80 degree. The pattern (B) is the zoomed area around the highest peak. .... 68

Figure 4.8 SEM images (high magnification) for SSC powders (heat-treated at 1000 °C/2h ) by (a) traditional combustion without glycine as the chelating agent (TC), (b) traditional combustion with glycine as the chelating agent (TC-G), (c) freeze-drying combustion without glycine as the chelating agent (FC) and (d) freeze-drying combustion with glycine as the chelating agent (FC-G). .... 69

Figure 4.9 Bright field TEM images (high magnification) for SSC powder (heat-treated at 1000 °C/2h ) by (a) traditional combustion without glycine as the chelating agent (TC), (b) traditional combustion with glycine as the chelating agent (TC-G), (c) freeze-drying combustion without glycine as the chelating agent (FC) and (d) freeze-drying combustion with glycine as the chelating agent (FC-G). .... 70

Figure 4.10 *I-V* and *I-P* curves (A) and Electrochemical impedance spectra curves (B) at 600 °C for the cell with SSC-GDC cathode prepared by (a) traditional-combustion with no glycine (TC), (b) traditional-combustion with glycine (TC-G), (c) freeze-drying combustion with no glycine (FC) and (d) freeze-drying combustion with glycine (FC-G) method, respectively .... 71

Figure 5.1 (a) 3D X-ray microscopy image (with a dimension of 3.20mm\*3.80mm\*0.74 mm); (b) cross-sectional image; (c) reconstructed 3D microstructure, The blue/blank regions represent solid/pore phase; (d) porosity distribution of the porous Ni-YSZ(SDC)|YSZ; (e) Visualization of a general field within the porous channels of the Ni-YSZ(SDC)|YSZ, when the field is conducted along the thickness direction. Colors from red to blue proportionally represent the field potential from high to low. .... 79

Figure 5.2 (a) Reconstructed 3D microstructure of porous Ni-YSZ anode substrate. The blue/blank regions represent solid/pore phase; (b) Porosity distribution of the Ni-YSZ anode substrate along the thickness direction .... 80

Figure 5.3 SEM images of cell after measurement (a, b) and SDC-covered anode (c, d, e and f). The (c) and (d) show images for the area near electrolyte while (e) and (f) show images for the anode bulk. .... 82

Figure 5.4 SEM images for the anode (without SDC layer) adjacent to electrolyte (a) and (b) the NiO-YSZ particles in the square area in (a) ..... 83

Figure 5.5 Open circuit voltage (OCV) curve for the cell without catalyst layer (a) and with catalyst layer (b) when operated with either 3 vol% humidified H<sub>2</sub> or CH<sub>4</sub>. ..... 84

Figure 5.6 Cell performance of cell without (a) and with (b) SDC catalyst layer. Inset in (a) are the IV and IP curves for cell at 800 °C. Inset in (b) are the *I-V-P* curves for cell at 700, 750 and 800 °C, respectively. The H<sub>2</sub> flow was controlled at 40 sccm while the oxidant was ambient air. .... 85

Figure 5.7 *I-V* and *I-P* curves (a), electrochemical impedance spectroscopy of cells with anode deposited with (red) and without (black) SDC catalyst layer (b) and stability measurement of cell with SDC catalyst layer when using H<sub>2</sub> or methane as fuel (c)..... 86

Figure 5.8 Raman spectra of different anodes after electrochemical measurement using either H<sub>2</sub> or CH<sub>4</sub> as fuel. The anodes in spectra (i), (ii) and (iii) were fabricated by freeze-drying tape-casting, while anode in spectrum (iv) was fabricated by dry-pressing..... 88

Figure 5.9 (a) The SAED patterns for the blank Ni-YSZ anode (without SDC layer) after treatment with CH<sub>4</sub> (Inset is the Bright Field (BF) image of the area selected for the SAED); (b) BF image of the anode aggregates (Red circled area showed small nano Ni<sub>x</sub>C<sub>y</sub> particles on the big YSZ particles); (c) HRTEM-image of one single crystalline Ni<sub>x</sub>C<sub>y</sub> particle sitting on YSZ particle and the corresponding Fast Fourier Transform (FFT) images for the selected A and B regions (Simulation of SAED using Ni<sub>3</sub>C and YSZ were also shown for comparison); (d) and (e) HRTEM-images of other Ni<sub>x</sub>C<sub>y</sub> particles with different sizes sitting on the YSZ particle in different area; (f) HR-image for one single Ni<sub>x</sub>C<sub>y</sub> particle dropped from the YSZ particle..... 89

Figure 5.10 (a) Cross-section SEM image for Ni-YSZ anode bulk with gas diffusion channel deposited without the SDC catalyst layer after operation on H<sub>2</sub>; (b) SEM image for anode without the SDC catalyst layer on channel wall after operation on CH<sub>4</sub>..... 92

Figure 5.11 The SEM (a), Bright Field (BF) image (b and c) of the Ni-YSZ anode with nanoscale SDC catalyst layer after operating in CH<sub>4</sub> (3% H<sub>2</sub>O) for 400 h, the HRTEM image of the surface of the SDC nano particles (d and e) (The corresponding FFT images and simulation SAED based on SDC and Ni<sub>3</sub>C in similar zone axis were also shown)... 92

Figure 5.12 EDX results for the Ni-YSZ anode with SDC layer after operation with CH<sub>4</sub> (3% H<sub>2</sub>O) at 800 °C for 400 h..... 93

Figure 5.13 (a) HRTEM image for the Ni particles zone from the Ni-YSZ anode with SDC as catalyst layer after operating in CH<sub>4</sub> (3% H<sub>2</sub>O) for 400 h. (FFT images and corresponding d-spacing in different area were also shown at left.) ..... 95

# CHAPTER 1 INTRODUCTION

## 1.1 BACKGROUND ABOUT SOLID OXIDE FUEL CELLS

Fuel cells are energy conversion devices that convert the chemical energy stored in fuel directly to electrical energy without the need for combustion as an intermediate step, showing much higher efficiency[1]. They can be considered as a “factory” which consumes fuel and directly generates electricity without the combustion process. They can produce electricity as long as fuels are supplied[2]. There are five major types of fuel cells defined by the electrolyte materials (Figure 1.1): polymer electrolyte membrane fuel cell (PEMFC), alkaline fuel cell (AFC), phosphoric acid fuel cell (PAFC), molten carbonate fuel cell (MCFC) and solid oxide fuel cell (SOFC). Each fuel cell has its own unique chemical reaction process according to different application requirements[3, 4]. The detail reaction for each type of fuel cell can be found in the book written by Ryan O’Hayre et al[2].

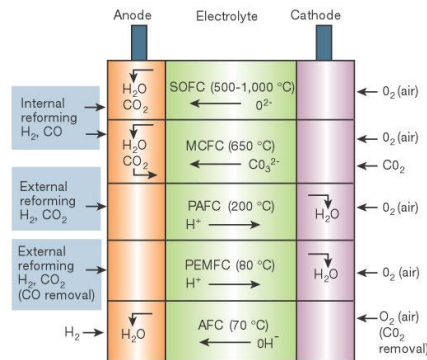


Figure 1.1 Summary of fuel cell types[5]

Solid oxide fuel cells (SOFCs) are the most efficient devices for conversion of chemical fuels because of their high efficiency, low pollutions, and quietness[6]. Because of high operation temperatures (800-1000 °C), some hydrocarbon fuels such as natural gas can be used directly without need for expensive and external reformer. Figure 1.2 shows the working principle for SOFCs based on oxygen-ion conducting electrolyte.

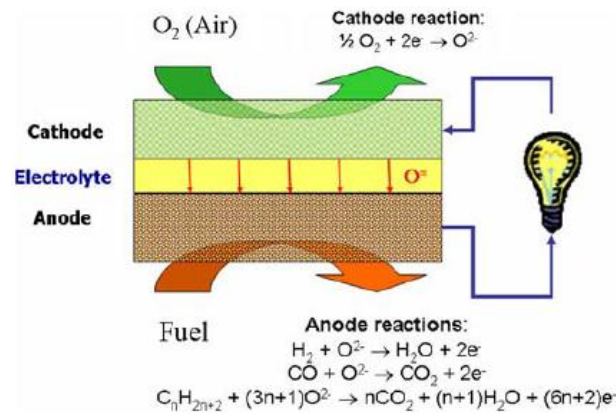


Figure 1.2 Working principle of SOFC[7].

The cathode operates in an oxidizing environment of air or oxygen and participates in oxygen reduction reaction:



O<sub>2</sub> first reaches the effective functional layer (10 μm adjacent to electrolyte) and then is reduced to oxygen ions, combining two electrons from external circuit. There are several requirements for the cathode in solid oxide fuel cells:

- (a) High electronic conductivity;
- (b) Chemical and structural stability in oxidizing environment during fabrication and cell operation process;

- (c) Thermal expansion behavior needs to match well with other cell components;
- (d) Compatibility and acceptable reactivity with the electrolyte and interconnection materials;
- (e) Sufficient porosity to facilitate oxygen transport from the gas phase to the cathode/electrolyte interface.

In the very beginning stages of SOFC development, platinum (Pt) was used as a cathode since other materials are not available. However, Pt is expensive and not practical for commercialization. Extensive investigations on cathodes were then moved to lanthanum strontium manganite (LSM) based perovskite, in spite of the issues like degradation, reactions with YSZ[7].

The anode must be stable in the reducing environment, must be electronically conducting, and must have sufficient porosity to allow the transport of the fuel to and the transport of the products of fuel oxidation away from the electrolyte/anode interface where the fuel oxidation reaction takes place. The most conventional anode material for anode is Ni- yttria stabilized zirconia (YSZ). YSZ prevents sintering of the nickel particles, decreases the anode thermal expansion coefficient and provides better connection between the anode and electrolyte.

The fluorite-structured oxide materials such as YSZ, rare earth doped ceria have been widely investigated as electrolyte for SOFCs. The yttrium oxide stabilizes the high temperature cubic phase in zirconium and also produces oxygen vacancies. The oxygen ion conductivity in YSZ can be attributed to these oxygen vacancies. The temperature dependence of electrical conductivity for zirconia based oxide is shown in Figure 1.3[8]. YSZ, which has been used extensively in SOFCs, shows a conductivity of 0.14 S/cm at

1000 °C. Scandia-doped zirconia (SSZ) has a higher conductivity and at 780 °C its value corresponds to that of YSZ at 1000 °C. The relationship between the temperature and electrolyte thickness as shown in Figure 1.03 suggests that at 700 °C, the thickness of the electrolyte should be less than 50 μm for YSZ and ytterbia-doped zirconia (YbSZ) systems, while an electrolyte as thick as 150 μm could be used for SSZ. Therefore, applications about thin film electrolyte have attracted much more attention, which will be the focus of the following chapters.

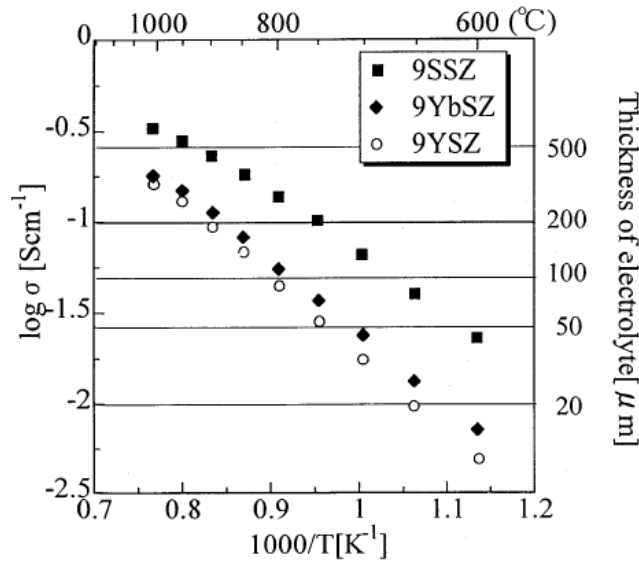


Figure 1.3 Temperature dependence of the electrical conductivity of the  $ZrO_2-M_2O_3$  systems. 9SSZ: 9 mol%  $Sc_2O_3-ZrO_2$ , 9YbSZ: 9 mol%  $Yb_2O_3-ZrO_2$ , 9YSZ: 9 mol%  $Y_2O_3-ZrO_2$ [8].

Single cells can be designed as electrolyte-supported, anode-supported, or cathode-supported. The key features of each configuration are summarized in Table 1.1[9].

The most popular design for SOFCs is anode-supported cell with thin electrolyte and thin cathode layer since they can be potentially operated at a lower temperature. By lowering temperature to 700 °C, conventional stainless steel can be used for interconnectors. For the anode-supported cell, it is advantageous that the ohmic resistance

is lower than that of the electrolyte-supported cell because much thinner electrolyte films can be employed. However, the contribution of the concentration polarization to voltage losses at high current densities will be significant since the thick anode prevents the supply of reactant gases to the electrochemical reaction sites at the anode/electrolyte interface. In thick porous anodes, the momentum of fuel gas is nearly zero and the fuel supply to the electrolyte is carried out mainly by diffusion of the reactant species.

Table 1.1 Features of single cell configurations[9]

Cell configuration	Advantage	Disadvantage
Electrolyte-supported	Strong structural support; Good gas-tightness	Higher resistance, high operation temperature
Anode-supported	Highly conductive anode; Lower operation temperature due to thin electrolyte	Potential anode reoxidation; Gas diffusion resistance due to thick anode
Cathode-supported	Lower operation temperature due to thin electrolyte	Lower conductivity; Gas diffusion limitation due to thick cathode

The overall performance of SOFC single cell is determined by various polarizations: namely ohmic, activation, and concentration. The main contribution to the ohmic polarization is due to the electrolyte. A high ionic conductivity and a small electrolyte thickness are the desired characteristics of the solid electrolyte to minimize the ohmic contribution. In electrode-supported cells, with a 10  $\mu\text{m}$  thick YSZ film as the electrolyte, the area specific resistance of the electrolyte is only about  $0.05 \Omega\text{cm}^2$  at  $800 \text{ }^\circ\text{C}$  thus making an efficient operation of an SOFC potentially at such a low temperature. However, it is usually observed that despite a low ohmic contribution, the area specific resistance of the cell as a whole may be several times larger. The reason is that activation

and concentration polarizations can often outweigh the ohmic contribution. Thus, the minimization of the overall area specific resistance of cells requires an optimization of parameters which govern the activation and concentration polarization effects. In this thesis, we are focusing on the development of anode-supported cell with thin electrolyte film. We are aiming at feasibility of SOFC single cells operated at intermediate or low temperature by monitoring the electrode structure.

## 1.2 POLARIZATION LOSS

Polarization is a voltage loss or overpotential, which is a function of current density. Three dominant polarizations are ohmic polarization, concentration polarization, activation polarization and transport polarization.

Under open circuit conditions, the Nernst potential,  $E$  or open circuit voltage (OCV), appears between the anode and the cathode, can be determined by

$$E = -\frac{\Delta G}{nF} \quad (1.2),$$

where  $n$  is the number of electrons participating in electrode reactions,  $F$  is Faraday constant,  $\Delta G$  is the net Gibbs free energy change of the reaction. When the flow rate of fuel and oxidant are sufficiently high such that the fuel and oxidant compositions are fixed, the Nernst voltage  $E$  is not the function of current. However, when the fuel and oxidant compositions are not fixed, the OCV itself must be treated as a function of current density. The voltage can be determined by:

$$V(i) = E(i) - \eta(i) = E(i) - \eta_{ohm} - \eta_{con} - \eta_{act} - \eta_{trans} \quad (1.3),$$

where  $V$  is the voltage across the external load,  $\eta$  is the polarization or overpotential, and is a function of current. It consists of a number of terms: ohmic polarization  $\eta_{ohm}$ ,

concentration polarization  $\eta_{con}$ , activation polarization  $\eta_{act}$ , and gas transport polarization  $\eta_{trans}$ . The details can be found in the book written by Singhal et al[9].

The ohmic polarization  $\eta_{ohm}$  is mostly coming from electrolyte since electrode materials for anode-supported SOFC are highly electron conductive.

The anodic and cathodic concentration polarization is then determined by[9]

$$\eta_{conc}^a = -\frac{RT}{2F} \ln\left(1 - \frac{i}{i_{as}}\right) + \frac{RT}{2F} \ln\left(1 + \frac{P_{H_2} i}{P_{H_2O} i_{as}}\right) \quad (1.4),$$

$$\eta_{conc}^c = -\frac{RT}{4F} \ln\left(1 - \frac{i}{i_{cs}}\right) \quad (1.5),$$

where  $R$  is the gas constant,  $T$  is the absolute temperature,  $\eta_{conc}^a$  is the concentration polarization from anode,  $i$  is the current density,  $i_{as}$  and  $i_{cs}$  is the limiting current density for anode and cathode, respectively, which has the following forms[2],

$$i_{as} = nFD_a^0 \frac{\rho_a}{\tau_a} \frac{c_R^0}{\delta_a} \quad (1.6),$$

$$i_{cs} = nFD_c^0 \frac{\rho_c}{\tau_c} \frac{c_R^0}{\delta_c} \quad (1.7),$$

$D_a^0$  and  $D_c^0$  are the reactant diffusivity in pure pore phase or free pore space in anode and cathode, respectively.  $\rho_a$  and  $\rho_c$  is the porosity, while  $\tau_a$  and  $\tau_c$  are the tortuosity factor for anode and cathode, respectively.  $c_R^0$  is the reactant concentration in the flow channel, and  $\delta$  is the thickness of the diffusion layer in the electrode. It can be seen that the anode with higher porosity and lower tortuosity can produce a higher limiting current density, thus a lower concentration polarization or overpotential can be expected. For anode-supported SOFC single cells, the anode concentration polarization is much higher than that of the

cathode because of its much higher thickness than that of cathode. Figure 1.4 shows the calculated concentration potential curves for anode-supported SOFC[10].

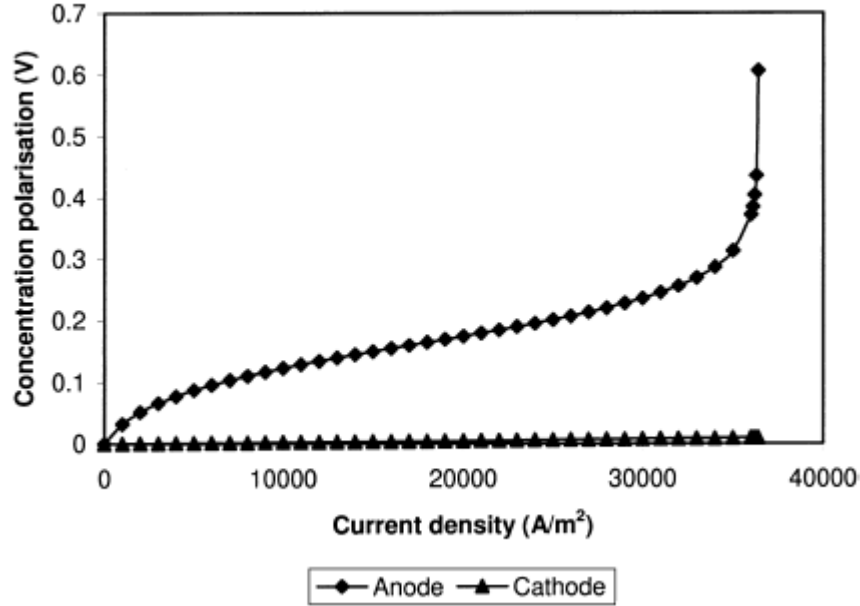


Figure 1.4 Calculated concentration polarization of anode-supported solid oxide fuel cell[10]

Activation polarization can be regarded as the extra potential necessary to overcome the energy barrier of the rate-determining step of the reaction to a value such that the electrode reaction proceeds at a desired rate. The activation polarization is normally expressed by the well-known Butler-Volmer equation[2]:

$$i = i_0 \left\{ \exp\left(\beta \frac{n_e F \eta_{act}}{RT}\right) - \exp\left(- (1 - \beta) \frac{n_e F \eta_{act}}{RT}\right) \right\} \quad (1.8),$$

where  $\beta$  is the transfer coefficient and  $i_0$  is the exchange current density. The transfer coefficient is considered as the fraction of the change in polarization that leads to a change in the reaction rate constant, and its value is usually 0.5 for the fuel cell. The exchange current density is the forward and reverse electrode reaction rate at the

equilibrium potential. Higher exchange current density indicates a higher electrochemical reaction rate and better cell performance.

When  $\beta=0.5$ , the activation overpotential  $\eta_{act}$  can be expressed as follows:

$$\eta_{act} = \frac{2RT}{n_e F} \sinh^{-1} \left( \frac{i}{2i_0} \right) \quad (1.9),$$

Under high activation polarization, the activation overpotential can be simplified as Tafel equation,

$$\eta_{act} = -\left(\frac{RT}{\beta n_e F}\right) \ln i_0 + \left(\frac{RT}{\beta n_e F}\right) \ln i \quad (1.10),$$

Under low activation polarization, the activation overpotential can be described as

$$\eta_{act} = \frac{RT}{n_e F i_0} i \quad (1.11),$$

which is the linear current-potential relation. The calculated anode and cathode activation polarization can be found in Figure 1.5[10]. It is shown that cathode polarization is obviously higher than that for anode due to the lower exchange current density.

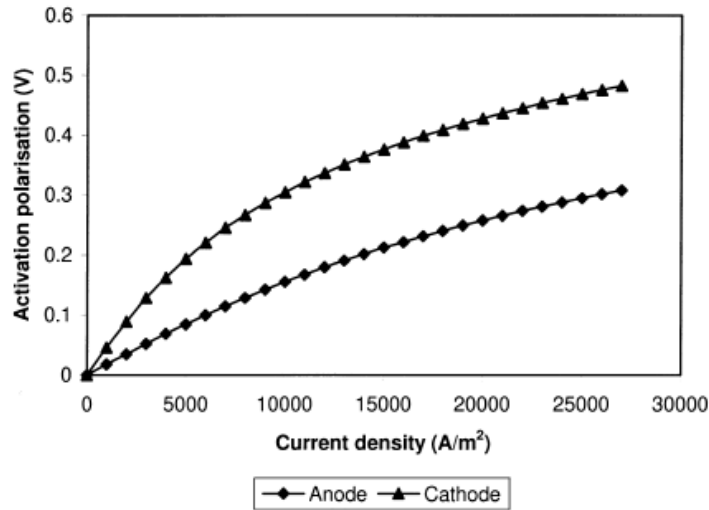


Figure 1.5 Calculated activation polarization of solid oxide fuel cell[10]

The exchange current density is determined by the following equation[2]:

$$i_o = nFc_R^* f \exp\left(-\frac{\Delta G}{RT}\right) \quad (1.12),$$

$c_R^*$  is the reactant surface concentration,  $f_l$  is the decay rate to products.  $\Delta G^*$  is the activation barrier.

The gas diffusion resistances from anode or cathode can be estimated by[11]

$$R_{Diffusion(anode)} = \left(\frac{RT}{2F}\right)^2 \delta_a \frac{1}{D_{H_2O,H_2}} \frac{\tau_a}{\rho_a} \left( \frac{1}{p_{H_2}} + \frac{1}{p_{H_2O}} \right) \times (1.0133 \times 10^5 \frac{Pa}{atm})^{-1} \quad (1.13),$$

or

$$R_{Diffusion(cathode)} = \left(\frac{RT}{4F}\right)^2 \delta_c \frac{1}{D_{O_2,N_2}} \frac{\tau_c}{\rho_c} \left( \frac{1}{p_{O_2}(cathode)} - 1 \right) \times (1.013 \times 10^5 \frac{Pa}{atm})^{-1} \quad (1.14),$$

where  $\delta_a$  and  $\delta_c$  are the thickness of the anode and cathode,  $D_{H_2O,H_2}$  is the binary diffusivity for a mixture of H<sub>2</sub>O and H<sub>2</sub> while  $D_{O_2,N_2}$  is the binary diffusivity for a mixture of O<sub>2</sub> and N<sub>2</sub>.

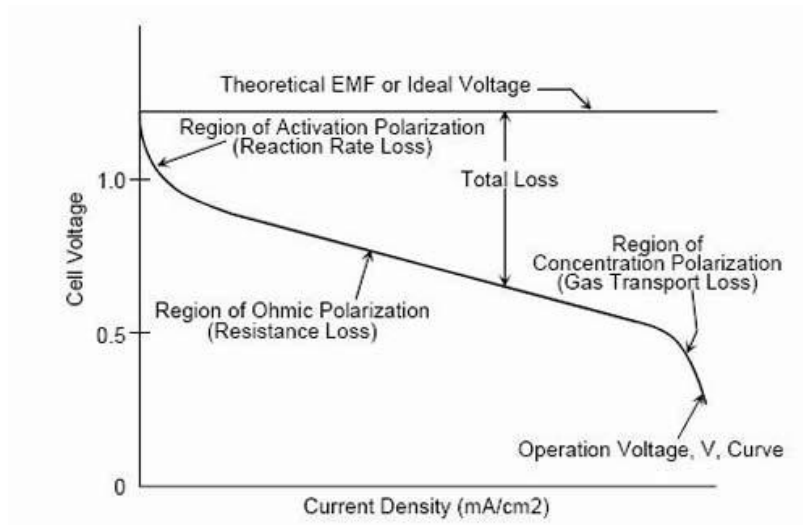


Figure 1.6 Typical polarization curve for solid oxide fuel cells

By ruling out all the polarization losses, the cell voltage vs current density can be shown in Figure 1.6. At low current density region, the voltage drop can be attributed to the kinetics of chemical reactions, i.e. activation polarization. After that, the linear drop with increasing current density is due to the electrolyte resistance. The final voltage drop at high current density is due to the concentration loss or gas transport loss. Therefore, a low activation and concentration polarization loss would lead to a high cell output. In this thesis, we are proposing a novel design of electrodes with extremely low polarization loss for SOFCs.

### 1.3 PROGRESS OF SOFCs WITH Ni-BASED ANODES OPERATING WITH METHANE FUELS

Natural gas (methane) has already been widely used as an important energy source in numerous applications, such as heating or cooking by direct combustion, and the generation of electricity by gas turbines or steam turbines[12], fuel for combustion engines in vehicles[13], hydrogen production via steam reforming[14]. However, the direct utilization of methane by aforementioned applications can increase the CO<sub>2</sub> emissions. One of the promising solutions is the development of SOFC technology, which can efficiently and cleanly convert the chemical energy of methane directly into electric power without the limitation of the Carnot cycle[15]. However, the anodes often suffer from coking when methane is fed into SOFCs system since state-of-art Ni cermet anodes are an excellent catalyst for methane cracking[16-18]. Carbon species adsorb strongly on Ni surface and thus block the active site for electrochemical reactions[19], resulting in rapid performance degradation. In addition, the sulfur in fuel gas could cause serious poisoning effects on the nickel cermet anodes[16]. To mitigate these problems,

substantial efforts have been devoted, including addition of other gases, application of polarization current, deposition of an anode catalyst layer and surface modification.

### *1.3.1 Addition of steam or CO<sub>2</sub> into fuel.*

By addition of oxygen-containing species, like steam, CO<sub>2</sub>, the O/C ratio can be increased, thus suppressing coking formation over the anode. Steam/C ratios greater than the thermodynamic minimum have been demonstrated to be necessary to avoid coking or crack of the anode[20]. In some cases, however, the actual steam/C ratio for effectively avoiding coke formation was drastically different from that predicted from the thermodynamic calculations[21]. The big discrepancy can be attributed to the fact that thermodynamic calculations do not account for the impact of reaction kinetics[22, 23]. In the thermodynamic calculations, a significant assumption is that the rates of the carbon deposition and carbon removal processes are sufficiently rapid to achieve equilibrium; however, in some cases, the microstructure that was assigned to reaction kinetics may significantly affect the coking resistance of the electrode.

Some researchers also attempted to suppress the coke formation over nickel cermet anodes by adding O<sub>2</sub> or CO<sub>2</sub> into the methane fuel gas[24]. However, the challenge is that the amount of oxidant added should be kept to a minimum because an increase in the amounts of such oxidants may increase the polarization resistances and reduce the power density; furthermore, an excessive amount of oxygen also increases the risk of reoxidation of the Ni-based anodes, which results in an irreversible effect on the operational stability of the cell.

### 1.3.2 Application of polarization current.

For SOFCs, application of polarization indicates that oxygen in the form of  $O^{2-}$  is transporting through cathode to anode. The  $O^{2-}$  will react with the fuel and carbon species when methane is fed into system[25, 26]. Figure 1.7 shows the possible reaction mechanism for the optimal metal-oxide interface of SOFCs[27]. Under OCV conditions, coking occurred on the Ni surface. When the cell was applied with a polarization current, the  $O^{2-}$  conducted through the YSZ electrolyte could spill over from the Ni-YSZ interface to the Ni surface, and the supplied  $O^{2-}$  could consequently effectively react with the coking on the Ni surface. The deposited carbon on the Ni surface was believed to be totally eliminated if the amounts of  $O^{2-}$  supplied were appropriately controlled. However, as mentioned by McIntosh et al[23], it is not possible to prevent carbon formation by a high  $O^{2-}$  flux through the electrolyte.  $O^{2-}$  can only be responsible for carbon removal in the region near the functional area,  $10\ \mu\text{m}$  adjacent to electrolyte. The coking in the anode bulk can not be alleviated.

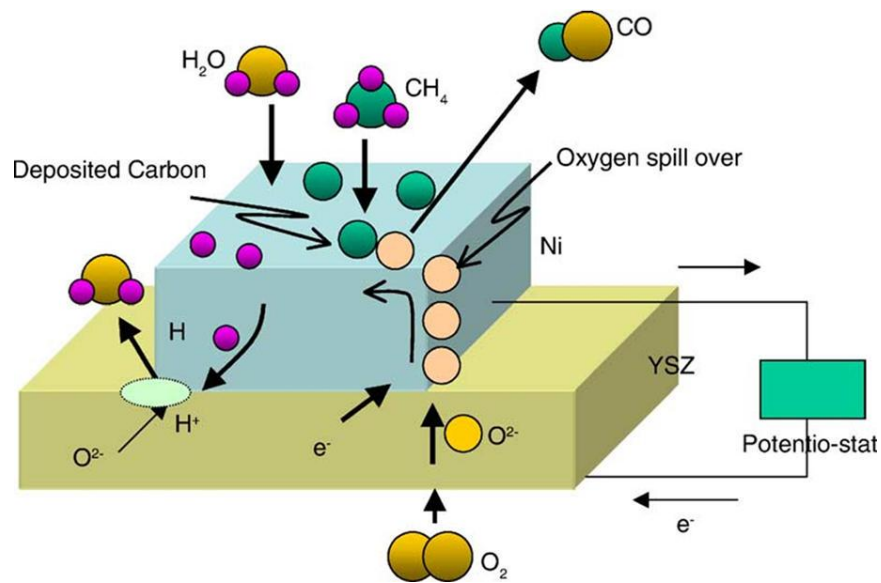


Figure 1.7 Models of  $CH_4$  decomposition and elimination of carbon deposition by applied voltage over Ni-YSZ interface[27].

### 1.3.3 Deposition of anode catalyst layer

The deposition of a catalyst layer with high activity for reforming/partial oxidation of hydrocarbons and good resistance toward coking on Ni cermets was also proposed to increase the operational stability and performance of hydrocarbon-fueled SOFCs[28-30]. As shown in Figure 1.8, methane and oxygen were first converted into CO and H<sub>2</sub> over catalyst layer, and then CO and H<sub>2</sub> diffuse to the anode, where they are electrochemically oxidized to produce H<sub>2</sub>O, CO<sub>2</sub> and electricity. A higher cell performance was expected by introducing the anode catalyst layer because of the higher electrochemical activities of CO and H<sub>2</sub>.

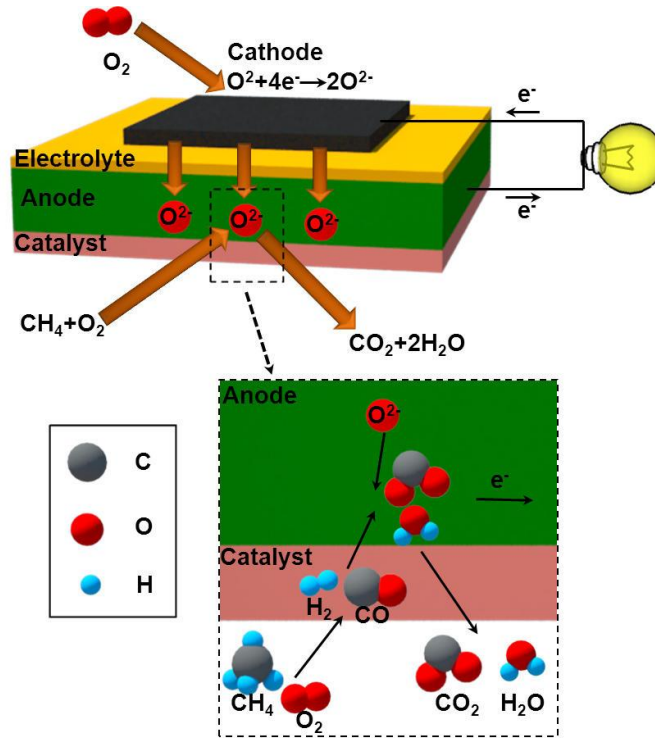


Figure 1.8 Schematic diagram of a SOFC with a catalyst layer during operation on CH<sub>4</sub>-O<sub>2</sub> gas mixture.

Recently, Suzuki et al reported the use of pure ceria as the catalyst layer for low temperature SOFCs operated on methane[31]. A very promising cell performance has been obtained at temperature as low as 449 °C. This study showed the promising performance of the CeO<sub>2</sub> catalyst layer for a fuel cell operated on methane-steam fuel.

#### 1.3.4 Surface modification

Surface modification on Ni cermet surface is another option for development of high electrocatalytic activity and coking resistance toward methane [32, 33].

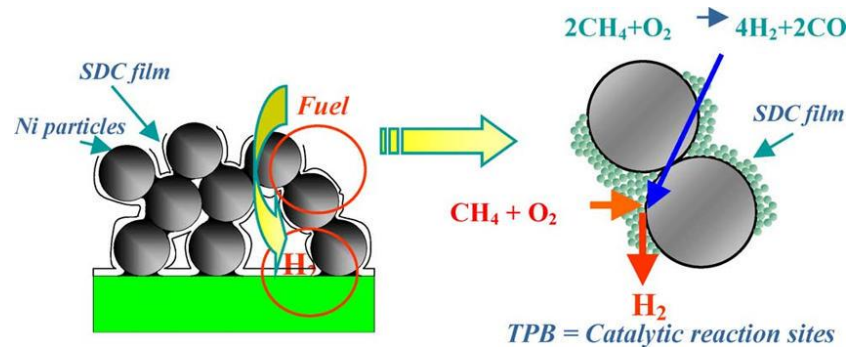


Figure 1.9 Schematic illustration of an anode microstructure coated with SDC[33].

Rare earth doped CeO<sub>2</sub> is a good promoter for Ni-based cermet anodes of SOFCs due to its advantageously high electrocatalytic activity and redox properties to suppress the coke formation[34]. The mechanisms for the improved coking resistance and the catalytic performance were illustrated in Figure 1.9[33]. The Sm<sub>0.2</sub>Ce<sub>0.8</sub>O<sub>1.9</sub> (SDC) thin film by infiltration provided individual ionic pathway, thus the coking on the triple phase boundary (TPB) sites was more readily oxidized by O<sup>2-</sup> over the anode[35].

#### 1.4 OBJECTIVE AND STRUCTURE OF THIS DISSERTATION

According to all the equations mentioned above, the concentration, activation and transportation polarization are all related to the microstructure of electrode, such as porosity, tortuosity factor etc. Therefore, an anode-supported SOFC consisting of more

porous and less tortuous substrate is expected to show better performance, indicating a feasibility of operation of SOFC at low temperature. Based on the novel open and straight anode structure, we propose a novel design for enhancing the cell performance and stability when using direct methane as fuel.

In this work, freeze-drying tape-casting has been proposed to fabricate the novel open straight electrodes for SOFC. In Chapter 2, the effects of freeze-drying tape-casting processing parameters such as solid loading, freezing bed temperature and tape pulling rate on the morphology of substrate have been investigated. The novel structured substrate has been fabricated and characterized by 3D X-ray microscope. In Chapter 3, we have explored the feasibility of fabrication of anode supported cell with thin ceria based electrolyte film using commercial powder, because of the high shrinkage of such substrate. Since the cathode is the center of the focus in the electrode development largely because oxygen reduction is more difficult to activate in SOFCs, in Chapter 4, we developed a novel cathode microstructure with low polarization loss by combining freeze-drying tape-casting and freeze-drying combustion. In Chapter 5, based on the novel pore structure, we have investigated the influence of surface channel modification via ceria solution infiltration on the cell performance. Further, we studied the electrochemical performance and long term stability for the cell deposited with SDC nano catalyst layer when using methane as fuel.

# CHAPTER 2 FABRICATION AND CHARACTERIZATION OF NOVEL FUNCTIONALITY GRADED POROUS ELECTRODE FOR INTERMEDIATE TEMPERATURE SOLID OXIDE FUEL CELL BY FREEZE-DRYING TAPE-CASTING

## 2.1 BACKGROUND

Currently, there are two basic geometric designs for SOFC development: electrolyte supported and electrode supported solid oxide fuel cells [6]. The ohmic resistance for electrolyte (typically yttria stabilized zirconia, YSZ) supported cells contributes largely due to the thickness of electrolyte ( $> 100 \mu\text{m}$ ), and thus such cells usually are designed for operation at high temperature such as  $1000 \text{ }^\circ\text{C}$ . For electrode supported cells, the electrolyte thickness can be decreased to  $10\text{-}20 \mu\text{m}$ , which decreases ohmic resistance significantly [36, 37]. Therefore, as demonstrated in Chapter 1, electrode supported cells are more suitable for operation at intermediate or low temperature in principle. However, the polarization resistance, especially concentration polarization may rise significantly resulting from the resistance to mass transport through thick electrode. In addition, for Ni-based anode, the insufficient removal of water steam during high temperature operation in SOFC can also result in Ni oxidation and agglomeration [38].

It has been recently reported that the electrode structure can be modified to minimize both activation and concentration polarization [39-41]. Suzuki et al [39] have reported a power density of greater than  $1 \text{ Wcm}^{-2}$  at  $600 \text{ }^\circ\text{C}$  with a conventional but high porous nickel cermet anode supported solid oxide fuel cell by controlling the microstructure of the anode. Providing sufficient porosity of the anode leads to significant improvement of the cell performance. Othman et al [40] also reported a high-performance micro tubular SOFC, which demonstrates a power density of up to  $2.32 \text{ Wcm}^{-2}$  at  $600 \text{ }^\circ\text{C}$ . The results were achieved by increasing the effective anode porosity through adjustment of co-extrusion parameters. The presence of fingerlike pores in the asymmetric anode layer significantly improves the gas diffusion by functioning as a bunch of hundreds of micro-channels in the anode, which subsequently increases the cell performance. It has been concluded that both porosity and microstructure played important roles in cell performance enhancement.

Given the traditional techniques, the method to engineering pore structure is limited to manipulation of thermal fugitive particle orientation and stability during slurry preparation. The generation of graded pores is often accomplished by lamination of layers with different microstructures, however, leading to complexity and cost. Freeze-drying tape-casting, which combines tape-casting and freeze-casting process to form and control complex pore structure, has been applied in the field of manufacturing catalyst support structures, solid oxide fuel cells and filtration membranes [42-44]. The freeze-drying tape-casting process not only allows tailoring of continuously graded pores through the entire cross section but also allows for long-range alignment of pores from the surface which is not readily seen in freeze casting through the use of small dies[42]. The typical

microstructure of the ceramic cross-section view and surface view can be found in Figure 2.1[42].

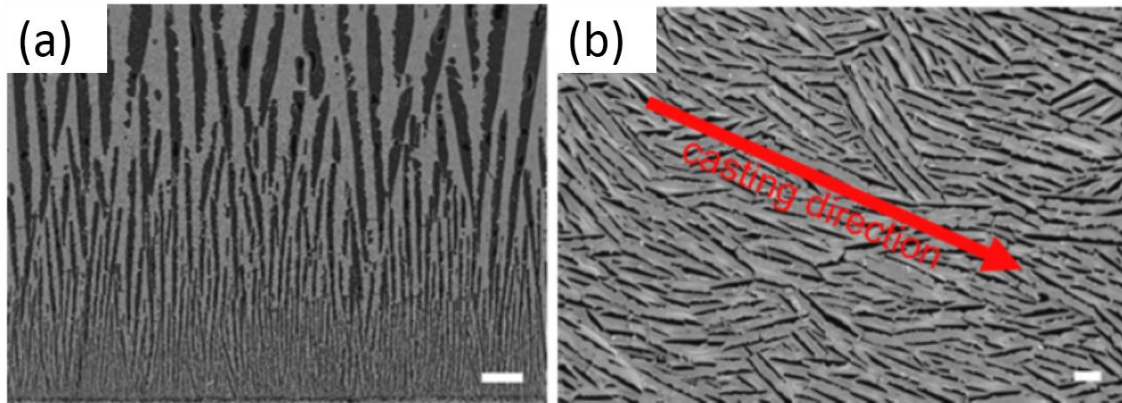


Figure 2.1 Cross-section scanning electron micrograph (a) and surface view (b) of 30 vol% solids YSZ oxide aqueous freeze-tape-casted substrate frozen at  $-50\text{ }^{\circ}\text{C}$ [42].

In freeze-drying tape-casting process, aqueous ceramic slurry is first prepared and then casted onto a Mylar carrier film. Similar to traditional tape casting, the slurry contains certain amount of organic binders that make the tape strong after solvent evaporation for handling and subsequently sintering. The slurry can be typically frozen in several minutes, eliminating particles precipitation in the traditional process, and resulting in homogeneity of composition of the product. After the solidification process, the tape is subsequently punched and freeze dried under a vacuum for quick solvent removal through sublimation, where the frozen liquid transforms from a solid to a gas without an intermediate liquid phase. The sublimation process eliminates capillary forces due to liquid-vapor transitions, thus alleviating the issues like warping[42]. The apparatus can be shown in Figure 2.2.

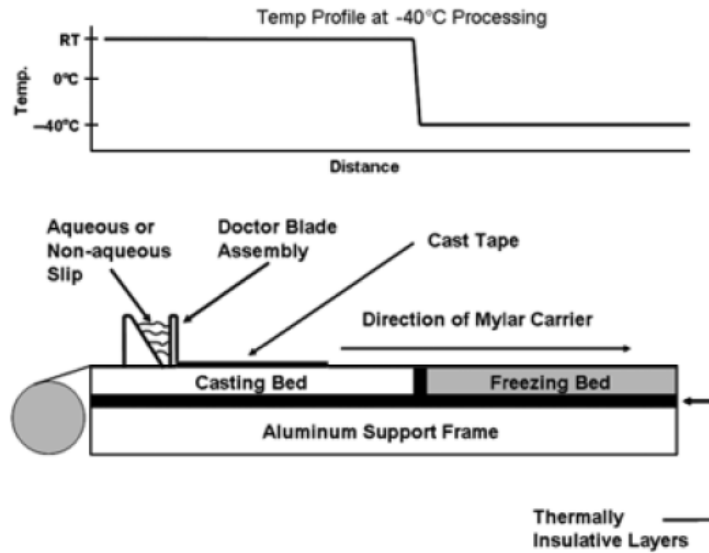


Figure 2.2 Modified freeze-drying tape-casting apparatus[42].

A continuously graded pores and long-range alignment of acicular pores (shown in Figure 2.1, in the range of 5 to 100  $\mu\text{m}$ ), which are very helpful for gas delivery in electrodes, can be obtained through freeze-drying tape-casting process. However, freeze-drying tape-casting always creates macro pores in both the bottom and top of anode substrates, dramatically increasing the difficulty in applying effective thin electrolyte film. Introduction of a thin anode functional layer has shown to be an effective method to overcome this limitation and improve the adhesion between electrode and electrolyte [45, 46]. In addition, the length of triple phase boundary (TPB) can be extended, thus resulting in more effective sites for electrochemical reaction. The NASA Glenn Research Center has developed a novel cell design and freeze-drying tape-casting technique to produce solid oxide fuel cells, predicting to exceed a specific power density of  $1.0 \text{ kW kg}^{-1}$  [43, 47]. Their bi-electrode supported cells are symmetrically prepared by taking two green parts cut from the same freeze-tape-casted YSZ scaffold, depositing a thin electrolyte layer between the tapes, and laminating the tapes together, forming the YSZ tri-layer. The

Ni nitrates for anode and stoichiometric solutions of Sr-doped LaFeO<sub>3</sub> for cathode were infiltrated into the YSZ scaffold without the use of vacuum. The symmetric design balanced mechanical stress and improved strength upon thermal cycling. One of the concerns with this design is the use of the wet infiltration techniques for the electrode fabrication. The metal Ni (nano size) is susceptible to sintering to large particles at high temperature during the cell operation.

In this chapter, we aimed to prepare solid oxide fuel cells by freeze-drying tape-casting with the conventional cell materials but with hierarchically oriented electrode substrates. The effects of solid loading, freezing bed temperature and casting tape pulling rate on the morphology of the electrode substrate have been investigated. The button cells fabricated in this chapter consist of NiO-YSZ (mass ratio = 6:4) for the anode support and the functional layer, YSZ for the electrolyte and (La<sub>0.75</sub>Sr<sub>0.25</sub>)<sub>0.95</sub>MnO<sub>3</sub> (LSM)-YSZ for the cathode. All materials used are commercially available. The microstructure features, pore size and size distributions and electrochemical performance of cells have been systematically evaluated.

## 2.2 EXPERIMENTAL

### 2.2.1 Fabrication and characterization of substrates and single cells

NiO (Sigma-Aldrich, USA) and YSZ (8YSZ, Tosoh Company, Japan) powders were selected as the preliminary materials for use in this study. The water based NiO-YSZ suspensions were prepared with an ammonium polyacrylate dispersant (Darvan C-N, R.T. Vanderbilt Co., Inc., Norwalk, CT) and thickener (Vanzan, R.T. Vanderbilt Co., Inc., Norwalk, CT) and an acrylic latex emulsion binder system (Duramax HA-12, Rohm & Haas, Philadelphia, PA). After frozen about 30 minutes, the substrate was punched into

several pellets with diameter of about 19 mm on the freezing bed. The pellets were frozen in a vacuum freeze dryer at -30 °C under 18 mtor for 12 h. The pellets were first sintered at a constant heating rate of 1 °C min<sup>-1</sup> to 600 °C and then of 2 °C min<sup>-1</sup> to 1100 °C. A functional layer was prepared by air-brushing method and then sintered at 800 °C for 2 h. The YSZ electrolyte film was prepared by drop-coating method. Then the anode substrate with functional layer and electrolyte layer was co-sintering at 1400 °C for 5 h. The LSM-YSZ composite cathode with an effective area of 0.33 cm<sup>2</sup> was prepared by a screen-printing method and then sintered at 1100 °C for 2 h. For the microstructure study, the Ni-YSZ substrates without YSZ film were prepared by sintering the green substrates at 1400 °C for 5 h and then reducing at 800 °C for 12 h.

### 2.2.2 Characterization

The microstructure of the Ni-YSZ anode substrate was characterized using a scanning electron microscope (SEM, FEI Quanta 200) and 3D X-ray microscope. The unique feature of 3D X-ray microscope is that this is nondestructive (as opposed to destructive techniques such as SEM/FIB-SEM) and hence allow following of specimen before and after any changes (such as reduction or loading). Pore size, pore size distribution and porosity of the Ni-YSZ substrate was determined by a mercury intrusion method (Micromeritics AutoPore IV 9500). In-house Matlab code was developed to calculate porosity along the thickness direction and the tortuosity factor of the Ni-YSZ anode substrate fabricated from the freeze-drying tape-casting process[48]. The current density-voltage curves as well as the impedance spectra were measured with a four probe method using a multi-channel Versa STAT (Princeton Applied Research) at the operating temperature range from 700 °C to 800 °C. The high temperature fuel cell testing system

can be seen in our previous work [49]. Humidified hydrogen gas (3 % H<sub>2</sub>O / 97% H<sub>2</sub>) was used as fuel while ambient air was used as oxidant. Hydrogen flow rate was controlled at 40 sccm by a mass flow controller (APEX, Alicat Scientific). The cell polarization resistance ( $R_p$ ) was determined from the difference between the low and high frequency intercepts of the impedance spectra with the real axis in the Nyquist plot.

## 2.3 RESULTS AND DISCUSSION

### 2.3.1 Novel microstructure of Ni-YSZ prepared by freeze-drying tape-casting.

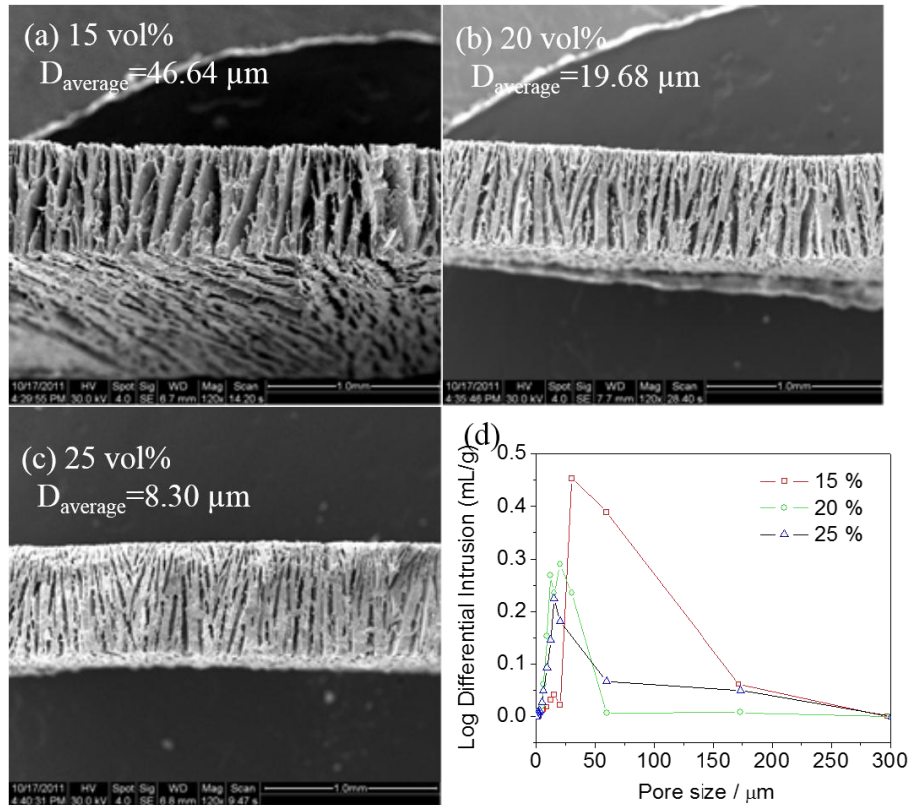


Figure 2.3 Cross-section SEM images of Ni-YSZ substrates with solid loading of: (a) 15 vol%, (b) 20 vol% and (c) 25 vol%; and (d) the pore size distribution for respective substrate.

In the aqueous freeze-tape-cast process, micron-sized ice crystals start to form on the side of anode substrate which is adjacent to the Mylar film and then grow larger and

larger towards the top of the tape. A natural gradient in porosity can be formed after the ice crystals have been removed by sublimation in a freeze-dryer under vacuum. Therefore, it is necessary to investigate how the processing parameters such as solid loading, freezing bed temperature and tape pulling rate affect the morphology of the casted tape.

Figure 2.3 shows the morphology features, pore size and pore size distribution of Ni-YSZ substrates with different solid loading varied from 15 vol% to 25 vol% while keeping the freezing bed temperature at  $-60\text{ }^{\circ}\text{C}$  and the tape pulling rate at  $48\text{ mm min}^{-1}$ . The graded pores grew perpendicularly to the freezing bed. There seems to be a loss of pore size, alignment and continuity with the increase in the solid loading of the slurry. The porosities of substrates are 60.88 %, 49.01 % and 37.57 % when the solid loading are 15 vol%, 20 vol% and 25 vol%, respectively. During the solidification of the slurry, the slurry changed into ice crystals and ceramic walls because the ceramic particles were rejected by the growing ice crystals[50]. The small ice crystals can develop into large crystals in the lower solid loading slurry while the pores in freeze-drying tape-casted samples are generated by sublimation of the ice crystals. Therefore, as shown in Figure 2.3, the substrate with lower solid loading has larger pores and porosity. The pore size distribution of the substrates with different solid loading can be seen in Figure 2.3 (d). The average pore sizes for the substrates with solid loading of 15 vol%, 20 vol% and 25 vol% are approximate 46.64, 19.68 and 8.30  $\mu\text{m}$ , respectively. The effect of solid loading on the microstructure can be attributed to the following reasons. On one hand, the bottom of the slurry on the casted tape was frozen first so that ice crystals grew very fast with finer ice crystal resulted from the temperature gradient due to the temperature at the bottom of the slurry was lower than that at top of slurry. On the other hand, the

interaction between ceramics and ice crystals became stronger and the growth of ice crystals was hindered by the ceramic particles in the higher solid loading slurry.

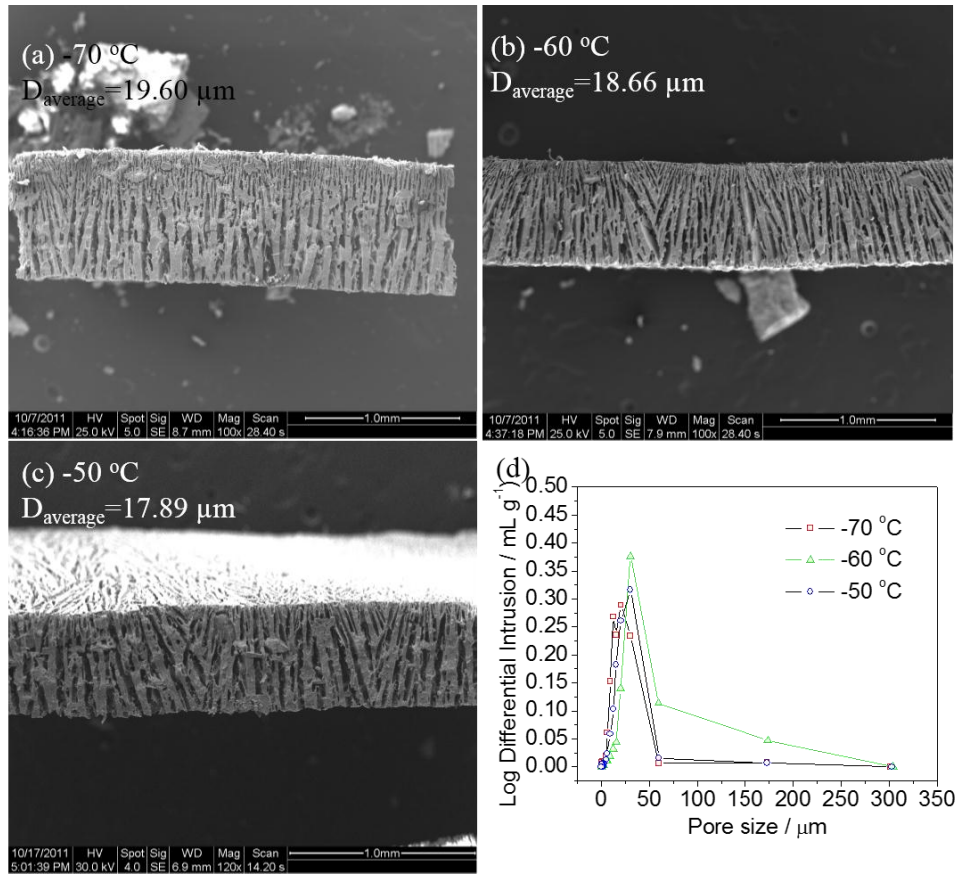


Figure 2. 4 Cross-section SEM images for Ni-YSZ substrates frozen at (a) -70 °C, (b) -60 °C and (c) -50 °C; and (d) pore size distributions for respective substrate.

Figure 2.4 shows the effect of freezing bed temperature (-70 °C, -60 °C and -50 °C) on the morphology, pore size and pore size distribution of Ni-YSZ substrates while keeping the solid loading at 20 vol% and the tape pulling rate at 48  $\text{mm min}^{-1}$ . All of them show similar pore size (around 18  $\mu\text{m}$ ) and similar pore size distribution behavior since the solid loadings are kept same. However, the difference in microstructure is obvious. Pores grown on lower temperatures show better ordering with uniform pore size and shape. Lower freezing bed temperature can lead to faster growth rate of the ice crystals and

introduce some dendritic growth of the ice crystals, as shown in Figure 2.4 (a); however, this is also accompanied by a discontinuity of porosity.

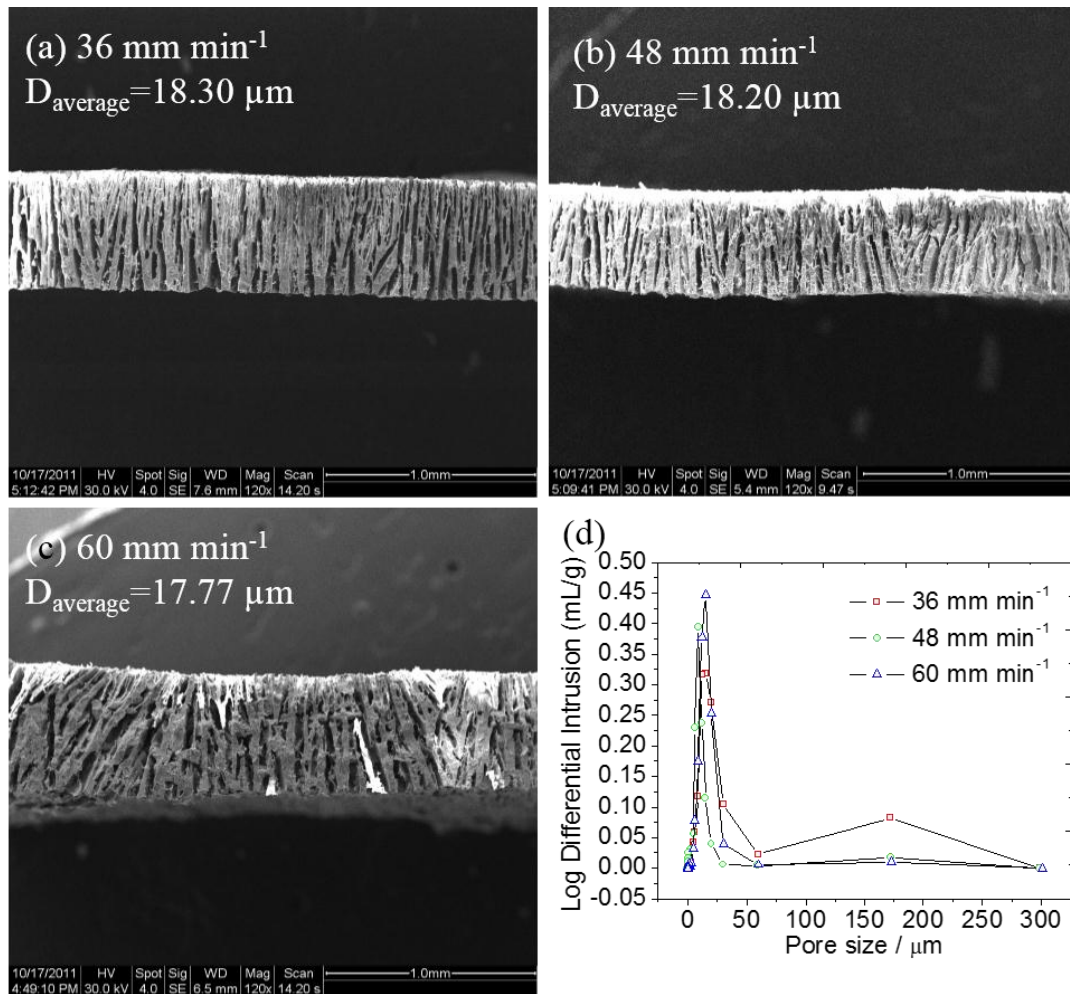


Figure 2. 5 Cross-section SEM images for Ni-YSZ substrate prepare from different pulling rate: (a) 36 mm min<sup>-1</sup>; (b) 48 mm min<sup>-1</sup> and (c) 60 mm min<sup>-1</sup>; and (d) pore size distributions for respective substrate.

Figure 2.5 shows the effect of pulling rate (36, 48, 60 mm min<sup>-1</sup>) on the microstructure, pore size and pore size distribution of Ni-YSZ substrates while keeping the solid loading at 20 vol% and the freezing bed temperature at -60 °C. There are also distinct differences in the morphology of the Ni-YSZ substrate although the pore size (around 18 μm) and distribution characteristics are very similar. Slower tape pulling rate

results in higher growth rate of the ice crystals, leading to less tortuous acicular finer pores in the low-temperature region in the substrate, which is helpful for subsequent fabrication of an interlayer or dense electrolyte film on the surface of the substrate.

In short summary, this research showed that the processing parameters during the freeze-drying tape-casting have significant influence on the porosity and morphology of the Ni-YSZ substrates. Lower solid loading leads to larger porosity. The freezing bed temperature and pulling rate affect the growth rate of the ice crystals in the casted tape. Higher ice crystal growth rate results in straight and less tortuous finer pores. Consequently, slurry with solid loading of 20 vol%, freezing bed temperature of  $-70\text{ }^{\circ}\text{C}$  and the tape pulling rate of  $48\text{ mm min}^{-1}$  have been chosen in this work to fabricate solid oxide fuel cells for electrochemical evaluation.

### *2.3.2 Geometric analysis of reconstructed 3D Ni-YSZ electrode*

#### *2.3.2.1 Phase Segmentation of the raw XCT data*

The anode substrate has been scanned by 3D X-ray computed tomography (XCT). The raw XCT data consists of 994 gray images, corresponding to the 2D slices along x axis in sequence. The interval step between images is  $4.53\text{ }\mu\text{m}$ , the same as the resolution of image. Accordingly, the 3D microstructure can be reconstructed by directly stacking the gray images along x axis in sequence. Figure 2.6 shows the reconstruction result. The size of matrix is  $4970\times 4455\times 500\text{ }\mu\text{m}$ . It is noted that the 3D microstructure is essentially a 3D numerical matrix containing voxel integers from 0 to 255. And thus, the phases can not be identified yet. Further, the image segmentation is needed based on the gray level matrix.

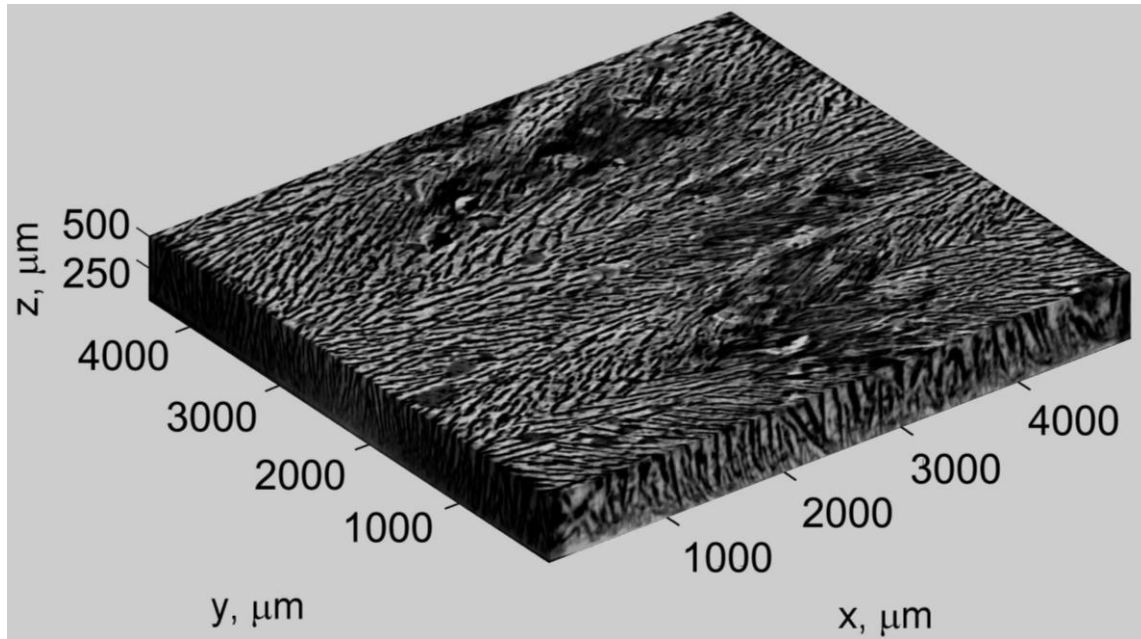


Figure 2. 6 Reconstructed 3D microstructure of porous Ni-YSZ electrode. The bright/dark region represents solid/pore phase.

Figure 2.7 shows the gray level histogram of the 3D matrix. It is clearly shown that there is a sharp peak at  $\sim 0$  gray levels, representing pore phase. Ni and YSZ characteristic peaks can not be distinguished since the contrast between Ni and YSZ is not obvious. Accordingly, only the solid phases (Ni and YSZ) and pore phase can be segmented. The two-phase segmentation is performed by using Otsu's method. The algorithm assumes that the image to be thresholded contains two classes of pixels then calculates the optimum threshold separating those two classes so that their combined spread (intra-class variance) is minimal. The optimum threshold has been determined as 96 for the solid-pore segmentation. The voxels whose gray value is below 96 were identified as pore phase. The other voxels whose gray value higher than 96 were identified as solid phase.

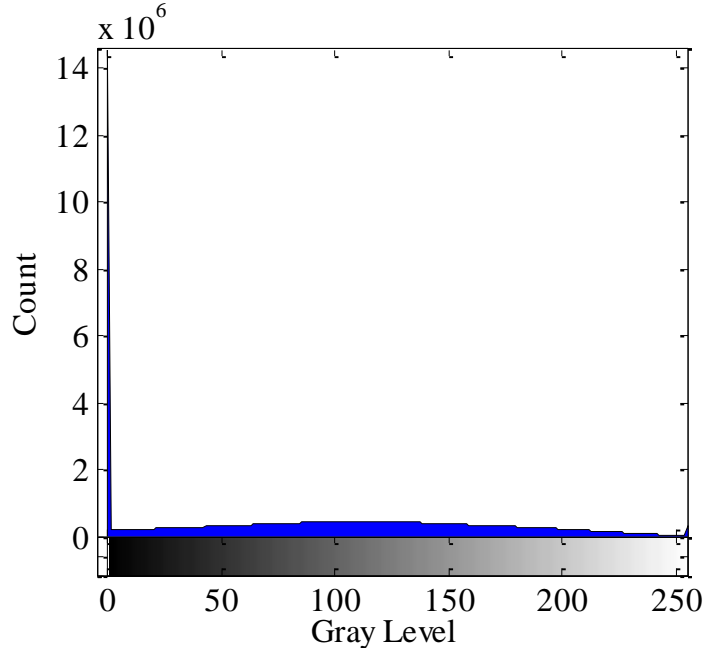


Figure 2. 7 Gray level histogram of the 3D XCT data.

#### 2.3.2.2. Local porosity and inner surface area along thickness direction

Local porosity and inner surface area have been calculated based on the segmented 3D matrix. To obtain their distributions along thickness direction (z axis as shown in Figure 2.06), 2D slices are extracted from the segmented 3D matrix perpendicular to z axis, and then 2D stereological method is employed. Local porosity has been calculated as the number fraction of pore pixels in 2D slice. Inner surface area,  $\mu\text{m}^2/\mu\text{m}^3$  is calculated by using random test lines in 2D slice,

$$area = \langle 2Seg_i / L_i \rangle \quad (2.1),$$

where  $Seg_i$  represents the number of intersections between a test line  $i$  and inner surface.

$L_i$  represents the length of test line  $i$ . Figure 2.08 shows the calculation results, showing that local porosity and inner surface area are hierarchically distributed along thickness direction.

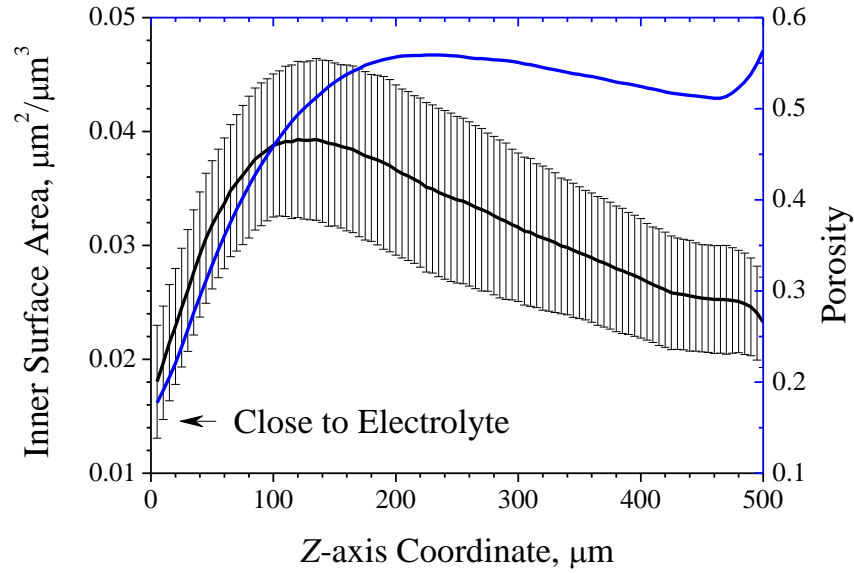


Figure 2. 8 Distributions of local porosity and inner surface area along z axis. Error bar represents standard deviation.

### 2.3.2.3. Tortuosity factors of solid phase and pore phase

In general, tortuosity factor of a conducting medium (solid phase for charges conducting or pore phase for gas diffusion) is defined as,

$$\tau = \phi \sigma_0 / \sigma_{\text{eff}} \quad (2.2)$$

where  $\phi$  is the volume fraction of conducting medium,  $\sigma_0$  is the conductivity or diffusivity of pure conducting medium, and  $\sigma_{\text{eff}}$  is the effective conductivity or diffusivity of the porous conducting medium.  $\sigma_{\text{eff}}$  can be 'measured' numerically by the solving of potential field within the conducting network. The potential obeys Laplace's equation,

$$\Delta \psi = 0 \quad (2.3)$$

By enforcing a constant potential difference on the domain boundaries of z axis, y axis, or x axis, the potential field distribution for a particular boundary condition is solved, then the current or flux density through the network can be calculated, and thus the

conductivity or diffusivity ratio,  $\sigma_0/\sigma_{\text{eff}}$  is obtained, which is independent of boundary conditions. Accordingly, the corresponding tortuosity factor in particular direction can be calculated. Detail description is published elsewhere[51].

In-house Matlab code is written to solve the Laplace's equation within 3D network. To solve the Laplace's equation within the entire 3D matrix for solid or pore phase, about  $4.4 \times 10^7$  algebraic equations should be solved, in addition to the requirement of huge space for data storage. For example, it needs full performance of a 4 GB RAM computer to solve the equation within a 50 pixels  $\times$  50 pixels  $\times$  100 pixels subdomain. By using the high performance computing cluster of University of South Carolina, we can tackle a subdomain with a size of 350 pixels  $\times$  350 pixels  $\times$  100 pixels (that is  $1750\mu\text{m} \times 1750\mu\text{m} \times 500\mu\text{m}$ ). Five  $1750\mu\text{m} \times 1750\mu\text{m} \times 500\mu\text{m}$  subdomains are extracted randomly from the entire domain followed by calculation. It is verified that the domain size of  $1750\mu\text{m} \times 1750\mu\text{m} \times 500\mu\text{m}$  is sufficient to calculate tortuosity factor accurately.

Figure 2.9 shows the calculated field distributions for the various boundary conditions within the pore network (a, b, c) and the solid network (d, e, f) of a  $1750\mu\text{m} \times 1750\mu\text{m} \times 500\mu\text{m}$  subdomain. It is shown that the patterns of field distribution are quite different for different boundary conditions, indicating that tortuosity factor for the 3D matrix is sensitive to conducting direction. The tortuosity can be further visualized by computing the streamline of field flux,  $-\sigma_0 \nabla \psi$ . The streamlines are a family of curves that are tangent to the velocity of flux. And thus, they are usually used to visualize conducting path. For example, Figure 2.10 a, b, and c show the streamlines with pore space when the pore network is enforced a constant potential difference on the boundaries of z axis, y axis, and x axis, respectively. It is shown that the streamlines along z axis are

more fluent than those along y axis and x axis. The streamlines along y axis are the most tortuous. The similar tendency is also observed for solid network, as shown in Figure 2.10 d, e, and f.

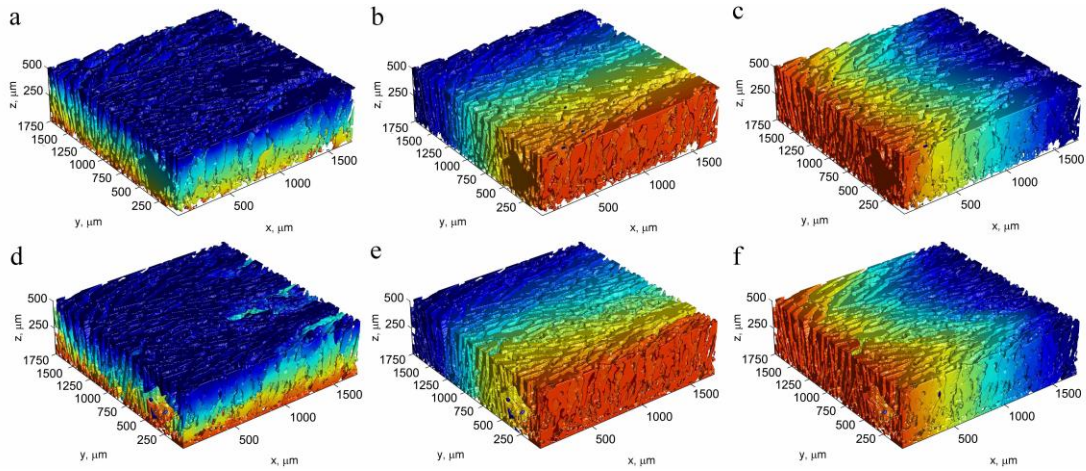


Figure 2. 9 Visualization of the field  $\psi$  distribution in a 3D subdomain extracted from the entire domain. a, b, and c show the field distributions in the pore phase network, when the network is enforced a constant potential difference on the boundaries of z axis, y axis, and x axis, respectively. Similarly, d, e, and f show the field distributions in the solid phase network (Ni+YSZ) along z axis, y axis, and x axis, respectively. Further, tortuosity factors of solid phase and pore phase along z, y, x axes can be calculated by using the field distributions. Colors from red to blue proportionally represent the field potential from high to low.

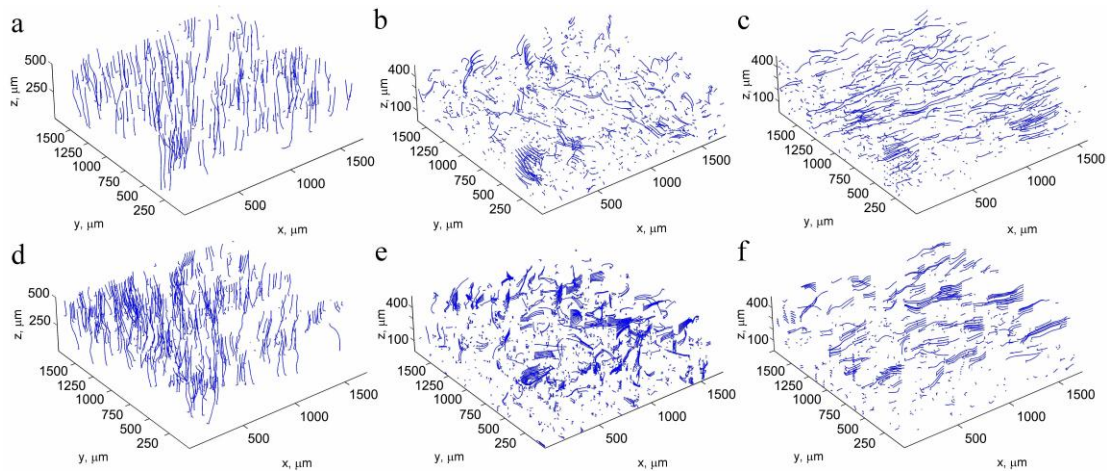


Figure 2. 10 Streamlines of the field flux  $-\sigma\nabla\psi$  in the 3D subdomain shown in Fig. 4. a, b, and c show the streamlines in the pore phase network, when the network is enforced a

constant potential difference on the boundaries of z axis, y axis, and x axis, respectively.

Similarly, d, e, and f show the streamlines in the solid phase network (Ni+YSZ), when the network is enforced a constant potential difference on the boundaries of z axis, y axis, and x axis, respectively.

Table 2.1 shows the statistical result of tortuosity factors for the five subdomains. It is shown that  $\tau_z < \tau_x < \tau_y$  for both solid phase and pore phase. Accordingly, the composite electrode is geometrically anisotropic. And it is of natural beauty to note that the conducting tortuosity for charges conducting and gas diffusion along thickness direction is smaller than any other direction.

### 2.3.3 Electrochemical performance of button Ni-YSZ supported SOFCs

Figure 2.11 shows the microstructure features of the anode-supported solid oxide cells and the surface view of the YSZ electrolyte. The cell has a thick anode gas delivery layer, a thin anode functional layer, a thin dense YSZ layer and a thin porous LSM-YSZ layer with thickness of about 450, 15, 10 and 20  $\mu\text{m}$ , respectively. The novel acicular and perpendicular pore structures can be seen in Fig 2.11 (a) and (b), similar like the ones reported by others[42]. Figure 2.11 (c) shows the surface view of the YSZ electrolyte. No big pin-pores are observable. The dense YSZ electrolyte is well adhered to the electrodes. The presence of open and straight pores in the anode substrate is expected to facilitate mass transport of the reactants to the TPB in the functional layer, thus accelerating the electrochemical reactions in the electrode.

Table 2. 1 Tortuosity factors of solid and pore phases along z, y, x axes. Five subdomains with a size of  $1750\mu\text{m}\times 1750\mu\text{m}\times 500\mu\text{m}$  are extracted randomly from the entire domain for use of calculation.

Sample No.	Solid Phase			Pore Phase		
	$\tau_z$	$\tau_y$	$\tau_x$	$\tau_z$	$\tau_y$	$\tau_x$
#1	1.6775	10.5993	1.9765	1.3216	5.4486	1.6843
#2	1.6805	8.9273	2.0636	1.4139	5.2537	1.8114
#3	1.6612	8.8215	2.0838	1.3984	5.0260	1.8484
#4	1.6446	7.7540	2.1062	1.4984	5.1858	1.9455
#5	1.6183	6.6421	2.2548	1.8212	4.8090	2.1261
Average $\pm$						
Standard	$1.6564 \pm$	$8.5488 \pm$	$2.0970 \pm$	$1.4970 \pm$	$5.1446 \pm$	$1.8831 \pm$
Deviation	0.0257	1.4739	0.1010	0.1951	0.2412	0.1649

Figure 2.12 (a) shows the cell voltage, current and power output curves of cells at different temperatures. Figure 2.12 (b) compares the cell power output of cells prepared by either dry-pressing or freeze-drying tape-casting method. As shown in Figure 2.12 (a), the cell peak power densities are 0.60, 0.95 and 1.28  $\text{Wcm}^{-2}$  at 700, 750 and 800 °C, respectively, almost doubled the cell output values previously reported at similar testing conditions with similar cell materials [52]. Under similar testing conditions, the cell power output for cells fabricated by freeze-tape-casting method is much higher than that of cells fabricated by dry-pressing method (Figure 2.12 (b)). The cell performance is even higher than the previous study of the anode with ceria oxide modification [53], further

demonstrating the advantage of the novel acicular pore structure in the hydrogen electrode substrate.

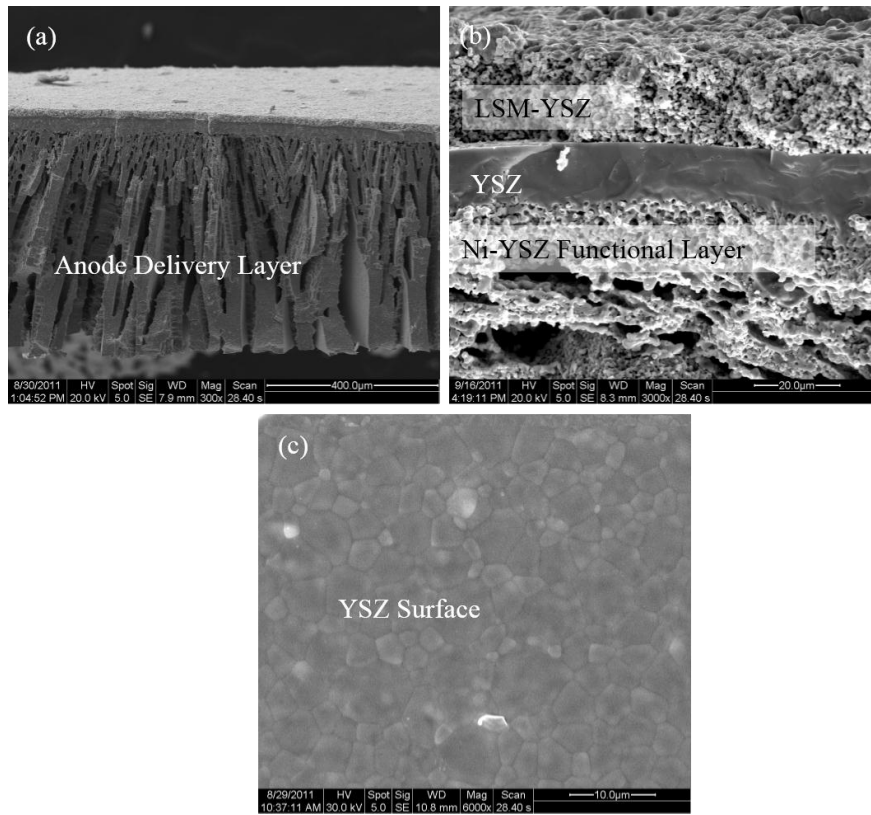


Figure 2. 11 SEM images of cross section view of the cell (a) and (b), and surface view of electrolyte YSZ (c)

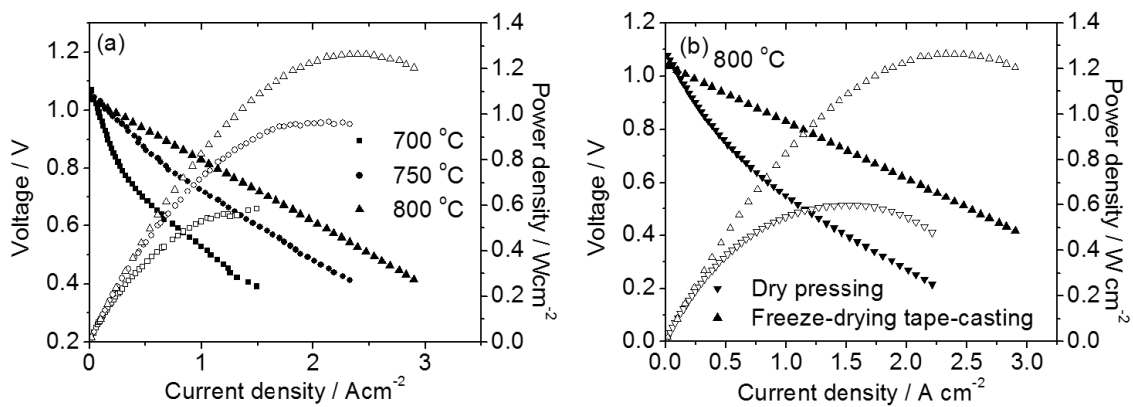


Figure 2. 12 (a) *IV* and *IP* curves of cell measured at different temperatures using hydrogen as fuel and ambient air as oxidant; (b) Comparison of *IV* and *IP* curves of cells prepared by either dry-pressing or freeze-drying tape-casting method measured at 800 °C.

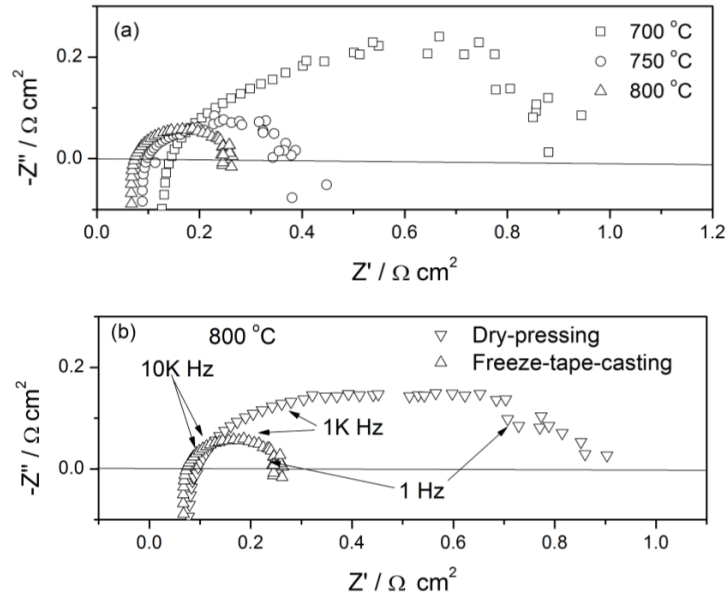


Figure 2. 13 (a) Impedance spectra of cells tested at different temperature under open circuit conditions (b) comparison of impedance spectra of cells fabricated by either dry-pressing or freeze tape-casting method measured at 800 °C

Figure 2.13 (a) shows the electrochemical impedance spectra of cells measured at different temperatures under open circuit conditions. The cell ohmic resistance ( $R_{\Omega}$ ), corresponding to the high frequency intercept of the impedance spectra with the real axis in the Nyquist plot, is 0.14, 0.10 and 0.08  $\Omega \text{ cm}^2$  at 700, 750 and 800 °C, respectively. The cell polarization resistance ( $R_p$ ), determined from the difference between the high and low frequency intercepts of the impedance spectra with the real axis, is about 0.80, 0.32 and 0.17  $\Omega \text{ cm}^2$  at 700, 750 and 800 °C, respectively.

Comparing to the interfacial resistance of the cells fabricated by dry-pressing and other publications [54-57], the total cell electrode polarization resistances in this study are much lower. The cell electrode polarization resistance comes from the resistance of the gas diffusion and gas conversion, i.e., gas diffusion and electrochemical conversion in both the anode and the cathode. Since the materials for both the anode and the cathode, and microstructure and thickness for cathode are almost identical, the decrease in the cell

polarization resistance could be attributed to the enhancement of the anode performance, probably due to the decreased hydrogen/water diffusion limit. The gas diffusion resistance through the anode can be estimated by the following equation [41, 58]:

$$R_{Diffusion(anode)} = \left(\frac{RT}{2F}\right)^2 l_a \frac{1}{D_{H_2O,H_2}} \frac{\tau_a}{\rho_a} \left( \frac{1}{p_{H_2}} + \frac{1}{p_{H_2O}} \right) \times (1.0133 \times 10^5 \frac{Pa}{atm})^{-1} \quad (2.4)$$

where  $R_{Diffusion(anode)}$  is the gas diffusion resistance in the anode,  $R$  is the universal gas constant,  $T$  is the absolute temperature,  $F$  is the Faraday's constant,  $l_a$  is the anode thickness,  $D_{H_2O,H_2}$  is the binary diffusion coefficient for a mixture of  $H_2O$  and  $H_2$ ,  $\tau_a$  is the tortuosity factor of the hydrogen electrode, and  $\rho_a$  is the volume fraction porosity of the anode,  $p_{H_2}$  and  $p_{H_2O}$  are the partial pressure of hydrogen and water vapor in the hydrogen electrode. The tortuosity factor for the anode substrate by freeze-drying tape-casting process is about 2, as obtained from mercury intrusion method, while the value for the anode substrate made from other traditional methods is typically between 3 to 10 [59]. Therefore, the gas diffusion resistance from the anode fabricated by freeze-tape-casting process is much lower, thus leading to enhanced cell performance.

## 2.4 SUMMARY

We have prepared and evaluated a novel functionally graded anode supported solid oxide fuel cell. We have investigated and discussed the effects of process parameters such as solid loading, freezing bed temperature and pulling rate on the microstructure. The structure properties like porosity and tortuosity factor have been calculated with help of 3D X-ray microscopy images. The novel structured cell has shown significant enhancement on the cell electrochemical performance using the conventional cell materials, indicating an excellent cell performance at intermediate temperature (below

800 °C). The cell demonstrates a maximum power density of 1.28 Wcm<sup>-2</sup> and a polarization resistance of 0.166 Ω cm<sup>2</sup> at 800 °C with 3 % H<sub>2</sub>O humidified H<sub>2</sub> as fuel and ambient air as oxidant. These results indicate that the novel functionally graded anode significantly facilitates gas diffusion, thus decreasing the concentration polarization resistance and enhancing the cell performance.

# CHAPTER 3 HIERARCHICALLY ORIENTED MACROPOROUS ANODE-SUPPORTED SOLID OXIDE FUEL CELL WITH THIN CERIA ELECTROLYTE FILM

## 3.1 BACKGROUND

Low temperature solid oxide fuel cells (SOFCs) have attracted great attention as one of the most promising next generation energy conversion systems for stationary and portable applications due to the unique merits of high efficiency, low emissions and fuel flexibility[6]. Yttria stabilized zirconia (YSZ) electrolyte has been extensively used by most SOFC developers due to its superior chemical stability and almost pure oxygen-ionic conductivity over a wide range of temperature and oxygen partial pressure. Unfortunately, the ionic conductivity of YSZ becomes relatively low when the operation temperature is reduced, resulting in a substantial increase in the ohmic resistance from the electrolyte[60]. In addition, lowering the cell operation temperature will result into a rapid increase in the interfacial polarization resistance from the electrodes. However, reducing the operating temperature of SOFCs to the intermediate temperature range of 500-600 °C is significantly beneficial to lower the cost and improve the reliability of the SOFC systems. Therefore, it is critical to develop highly conductive electrolyte materials as well as optimize the electrode

microstructure so that the electrochemical process in both the electrolytes and electrodes can be enhanced.

Gd-doped ceria (GDC) is a promising electrolyte best suited for intermediate temperature (500-600 °C) SOFCs due to its much higher ionic conductivity compared to that of YSZ as well as chemical compatibility with the state-of-the-art electrode materials. One challenge to fabricate ceria thin film electrolyte in SOFCs is the densification problem. The stringent powder fabrication process limits its broad application of dense ceria film electrolyte in SOFCs. Most of the ceria powders used in those thin film preparations were nano-sized, made through chemical process such as hydrothermal[61], solution combustion[62] or co-precipitation[63]. Further, the densification of thin electrolyte layer deposited on anode substrate can be greatly influenced by the shrinkage of the anode substrate[64].

The traditional homogenous microporous anode substrates have been investigated extensively and proven to be beneficial for the densification of electrolyte or interconnector film by drop-coating[57, 65, 66]. However, such morphology is not ideal for gas diffusion because of the high tortuosity factor, consequently limiting SOFC cell performance. Although the pore structure could be modified by changing the morphology or packing of the pore-formers[67], the tortuous microstructure of the electrode still limits the cell performance[40]. Recently, freeze-drying tape-casting method has been developed as a novel technique to form hierarchically oriented channels/pores in the SOFC electrodes[44, 47, 68]. Further, the substrates prepared by freeze-drying tape-casting in this study have the following unique features[42, 68]: i) The green tapes have adequate mechanical strength to handle for the subsequent drop-

coating without the need of pre-sintering due to the existence of organic additives; ii) The shrinkage of the anode substrate is much higher upon sintering the green tape instead of the pre-sintered one, providing more compressive driving force to facilitate densification of ceria film; iii) The surface of the green tapes are porous after the freeze-drying step, making a good interlocking interface between the anode and the electrolyte during the drop-coating and co-firing process. All these merits allow the feasibility of fabrication of dense GDC thin film electrolyte on freeze-drying tape-casted substrates.

## 3.2 EXPERIMENTAL SECTION

### 3.2.1 Fabrication of anode substrates and cells

NiO (Sigma-Aldrich, USA),  $\text{La}_{0.6}\text{Sr}_{0.4}\text{Co}_{0.2}\text{Fe}_{0.8}\text{O}_3$  (LSCF) and  $\text{Gd}_{0.1}\text{Ce}_{0.9}\text{O}_2$  (GDC) powders were both purchased from Fuel Cell Materials (USA) in this study. NiO-GDC (mass ratio of 60:40) anode substrate was prepared by a freeze-drying tape-casting process as reported in our previous study.[68, 69] The GDC electrolyte slurry was directly deposited on the green NiO-GDC anode substrates by a drop-coating process. The electrolyte/anode bi-layer was then sintered at 1400, 1450 and 1500 °C for 12 h at a heating rate of 1 °C min<sup>-1</sup> before 600 °C and then at 2 °C min<sup>-1</sup> after 600 °C. LSCF-GDC (mass ratio of 1:1) cathode with an active area of 0.33 cm<sup>2</sup> was prepared on the GDC electrolyte surface by screen-printing and then fired at 1050 °C for 2 h. For comparison, NiO-GDC anode substrate with 20 wt% graphite was prepared by dry-pressing [65]. Anode supported cell using the anode by dry-pressing with the cell configuration of NiO-GDC|GDC|LSCF-GDC has also been fabricated and evaluated. The preparation method for electrolyte and cathode are kept the same.

### 3.2.2 Characterization

The surface of the GDC electrolyte film, anode substrate and cross-sectional view of the single cells were characterized using both scanning electron microscope (SEM) (FEI Quanta 200) and 3D X-ray computed tomography (XCT). The unique feature of 3D X-ray microscope is that this is nondestructive (as opposed to destructive techniques such as SEM/FIB-SEM) and hence allows following of specimen before and after any changes (such as reduction or loading). In-house Matlab code was developed to calculate porosity along the thickness direction and the tortuosity factor of the NiO-GDC anode substrate fabricated from the freeze-drying tape-casting process[51], similar shown in Chapter 2. Hydrogen (with 3 vol% H<sub>2</sub>O) was used as fuel while ambient air was used as oxidant. Hydrogen flow rate was controlled at 40 sccm using a mass flow controller (APEX, Alicat Scientific). The *I-V* and *I-P* curves as well as electrochemical impedance spectra (EIS) of the single cells were measured with a four probe method using a multi-channel Versa STAT (Princeton Applied Research) at the operating temperature from 500 °C to 600 °C. The electrochemical impedance spectra of cells were measured under open circuit voltage over a frequency range of 1 MHz to 0.01 Hz. The ohmic resistance ( $R_o$ ) was determined from the high frequency intercept of the impedance spectra with the real axis while the cell interfacial polarization resistance ( $R_p$ ) was determined from the difference between the low and high frequency intercepts of the impedance spectra with the real axis in the Nyquist plot.

### 3.3 RESULTS AND DISCUSSION

#### *3.3.1 Hierarchically oriented macroporous anode substrate through freeze-drying tape-casting*

During solidification of aqueous NiO-GDC slurry, formation of ice from water rejects not only organic additives but also inorganic ceramic powders[70]. Subsequent removal of ice crystals by sublimation during the freeze-drying process results in the formation of pores. The substrates obtained from freeze-drying tape-casting always show a graded porous structure due to the exaggerated growth of ice crystal[42, 71]. In the freeze tape-casting, ice crystals first nucleated on the surface of chilling polymer film (-70 °C in this study) and then grew upwards through the temperature gradient, causing the crystals to diverge, forming a continuous graded pores/channels, in which some of them spanned the entire thickness of the substrate, resulting in a less tortuous structure. Microscopic images in Figure 3.1 display the morphology of NiO-GDC substrate made through freeze-drying tape-casting after sintered at 1450 °C for 12 h.

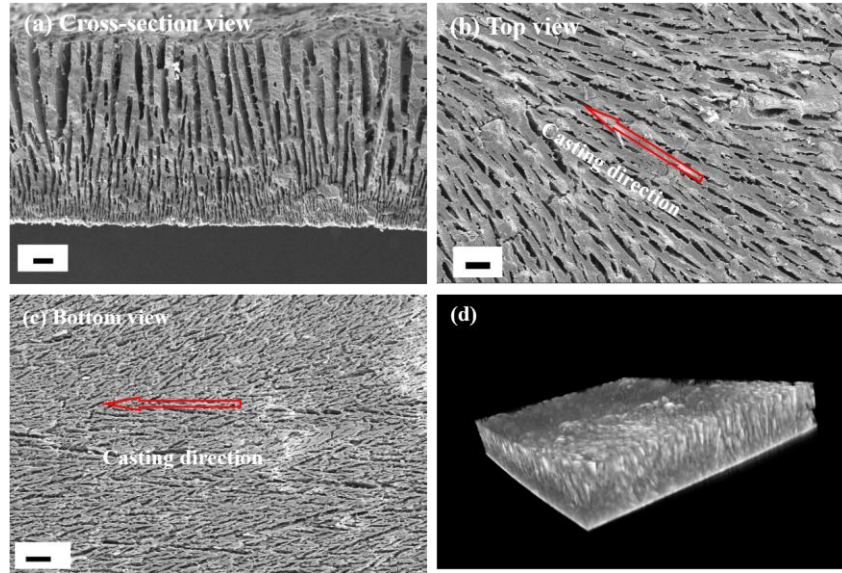


Figure 3. 1 (a) Typical cross-section view of sintered substrate made through freeze-drying tape-casting; (b) Surface view of the top part in (a); (c) Surface view of the bottom part in (a) (Bar=100  $\mu\text{m}$ ); and (d) 3-D X-ray microscopy image of the anode substrate with a dimension of 3.03mm\*3.72mm\*0.55 mm.

Figure 3.1 (a) shows the cross-section SEM view of the substrate, showing the typical structure with graded open pores/channels, similar to previous reports[42, 72]. The top part of the micrograph is the area away from the polymer film, where the NiO-GDC tape is exposed to the environment, while the bottom part is the area close to the polymer film in the casting bed, on which ice nucleation started. Figure 3.1 (b) and (c) show the surface views of top part and bottom part in Figure 3.1 (a), respectively. Both top and bottom surface show an acicular morphology of ice crystals/pores, typical feature for freeze-drying tape-casting[42]. The pore/channel size (width) is changing from about 10  $\mu\text{m}$  on the bottom part to 20  $\mu\text{m}$  on the top part of the NiO-GDC substrate shown in Figure 3.1 (a), indicating a gradient in size along the thickness direction. Figure 3.1 (d) displays the 3-D XCT of the anode substrate with a volume of 3.03mm\*3.72mm\*0.55 mm. The bottom part in Figure 3.1 (d) is the

area close to the chilling polymer film during the freeze tape-casting process, similar to that shown in Figure 3.1 (a).

To further study the NiO-GDC anode structure quantitatively, a 3D microstructure has been reconstructed by directly stacking the raw X-ray gray images along x axis in sequence. The interval step between images is  $4.53 \mu\text{m}$ , the same as the resolution of the image. Figure 3.2 (a), (b) and (c) show the reconstruction results for three different regions of the NiO-GDC substrate. To obtain the porosity distribution along the thickness direction (z axis as shown in Figure 3.2 (a, b, c)), 2D slices are extracted from the segmented 3D matrix perpendicular to the z axis, and then 2D stereological method is employed[73]. Local porosity is calculated as the number fraction of pore pixels in the 2D slice. Figure 3.2 (d) presents the porosity results, showing that local porosity is kept around 42 % distributed along the thickness direction, similar to our previous results (49.01 %) obtained from the mercury intrusion method[68].

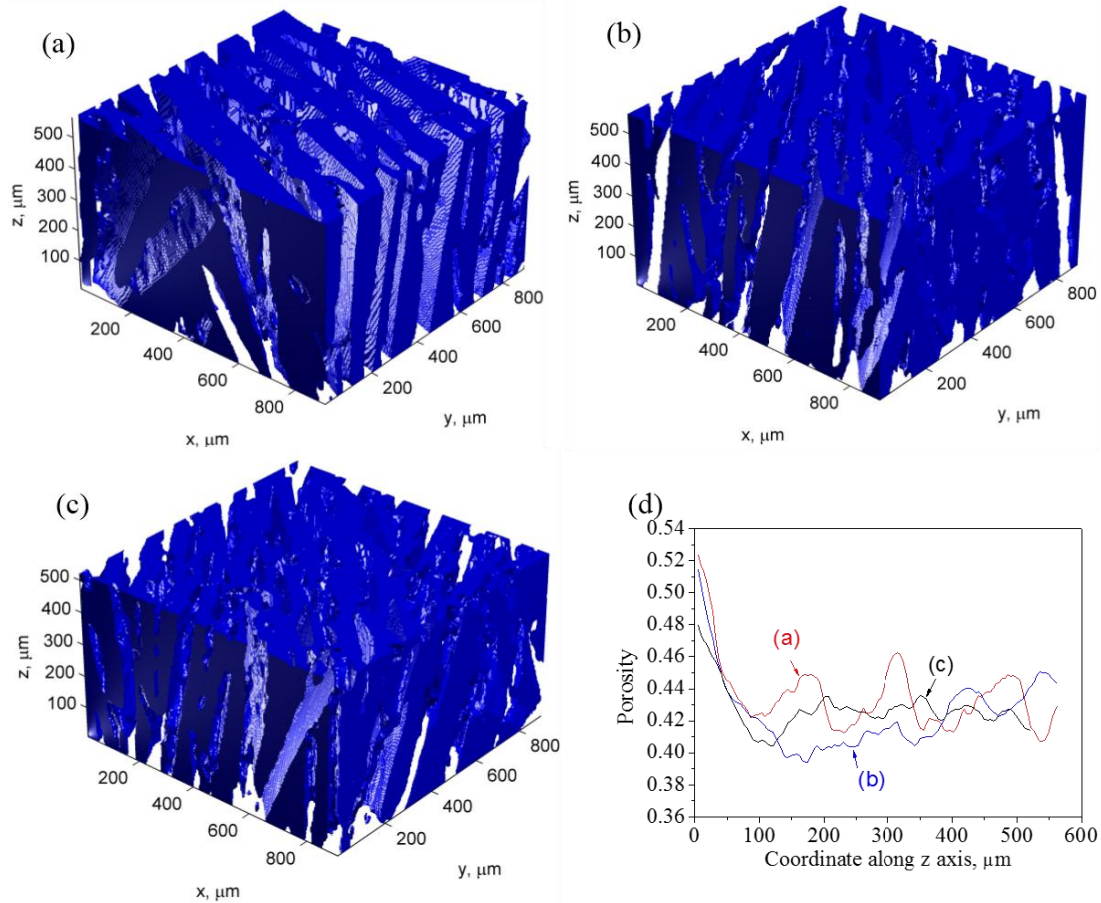


Figure 3. 2 Re-constructed 3D microstructure images from the three different subdomains (a, b and c) of porous NiO-GDC substrates. The blue/blank regions within the 3D images represent solid/pore phases. (d) Distribution of the local porosity along z axis for the three different subdomains (a), (b) and (c).

Three  $896 \mu\text{m} \times 896 \mu\text{m} \times 550 \mu\text{m}$  subdomains are extracted randomly from three different regions shown in Figure 3.2 (a), (b) and (c) for tortuosity factor calculation. Table 3.1 shows the calculation results of tortuosity factors for the three different subdomains. Along the thickness direction, a tortuosity factor of around 1.3 is obtained, which is much smaller than that for those sponge-like structured substrates (with a tortuosity factor value of 6-10).[74] From Table 3.1, it can also be seen that  $\tau_z < \tau_x < \tau_y$  for the pore phases. The x axis is the casting direction as shown in Figure 3.1. Although the

NiO-GDC composite electrode is geometrically anisotropic, different region shows similar porosity or tortuosity factor along the thickness direction. The tortuosity factor in this study along the thickness direction is smaller than any other direction. It is expected that the gas diffusion resistance along the thickness direction will be substantially reduced during the fuel cell operations.

Table 3.1 Tortuosity factors of pore phases along z, y, x axes. Three subdomains with a size of  $896 \mu\text{m} \times 896 \mu\text{m} \times 550 \mu\text{m}$  are extracted randomly from the scanning regions for calculation.

Sample No.	Pore Phase		
	$\tau_z$	$\tau_y$	$\tau_x$
#1	1.270	39.182	2.359
#2	1.328	7.464	4.767
#3	1.235	16.587	3.640

Figure 3.3 shows the shrinkage of the NiO-GDC substrates made through either freeze-drying tape-casting or the conventional dry-pressing method with thin GDC film after sintering at different temperatures. Insets are SEM images of the surface of GDC film on freeze-drying tape-casted anode substrate. The shrinkage was calculated by measuring the diameter of substrates before and after high-temperature co-sintering. As shown in Figure 3.3, for the half cell sintered at  $1450 \text{ }^\circ\text{C}$  for 12 h, the shrinkage of freeze-drying tape-casted substrate is about 19 %, while the shrinkage of dry-pressed substrate is only 12 %. Higher shrinkage of the anode substrate facilitates the densification of GDC film[64], confirmed by the higher open circuit voltage. The more shrunked cell shows an OCV value of 0.88 V at  $600 \text{ }^\circ\text{C}$ , much higher than that (0.79 V at  $600 \text{ }^\circ\text{C}$ ) for less shrunked cell under similar testing conditions. In addition, the porous surface of the green freeze-drying

tape-casted substrate makes the connection between anode and electrolyte much better during drop-coating and co-sintering. In this chapter, for cell preparation, GDC film was prepared by co-firing GDC green film on the green freeze-drying tape-casted NiO-GDC substrates at 1450 °C for 12 h.

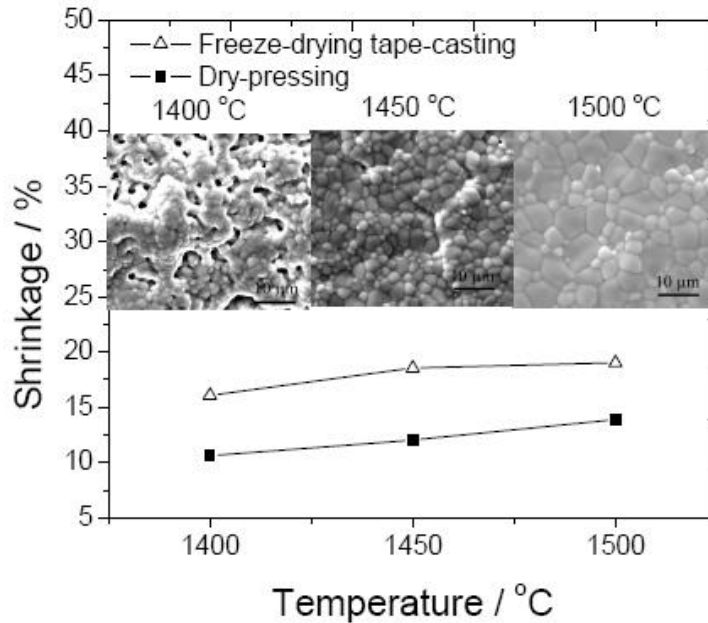


Figure 3.3 Shrinkage of GDC film on NiO-GDC sintered at different temperatures, with NiO-GDC substrates made by either freeze-drying tape-casting or dry-pressing. Insets are surface views of GDC film on freeze-drying tape-casted substrate sintered at different temperatures.

Figure 3.4 shows the microstructure feature of the cell after electrochemical performance measurement. The dense 30 μm-thick GDC electrolyte film is well adhered to both the anode (~550 μm) and the cathode (~30 μm). As shown in Figure 3.4, the hierarchically oriented straight pores/channels are expected to facilitate mass transport in the anode.

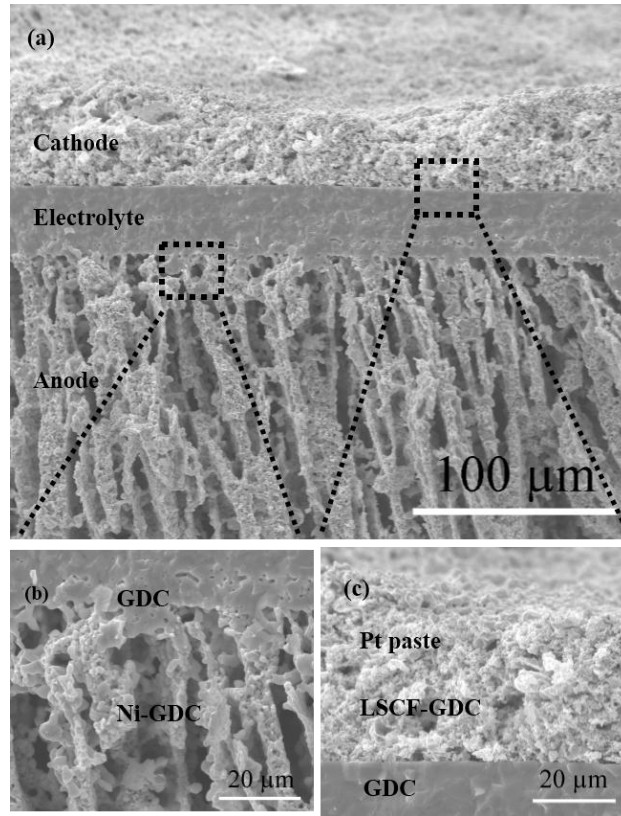


Figure 3. 4 SEM images of cross sectional views of the cell after fuel cell testing. (a) anode/electrolyte/cathode interfaces; (b) anode/electrolyte interface and (c) cathode/electrolyte interface.

Figure 3.5 (a) shows the cell voltage, current and power density curves of cells at different operating temperatures. The open circuit voltage (OCVs) of the cell are 0.929, 0.908 and 0.882 V at 500, 550 and 600 °C, respectively, which could be attributed to the minor electronic conduction of the GDC electrolyte due to the reduction of  $Ce^{4+}$  at the reducing atmosphere. But they are in good agreement with the values reported by others[40, 63]. By contrast, at same conditions, the OCV values (for example, 0.79 V at 600 °C) for those through dry-pressing are lower, indicating that the freeze-drying tape-casted cell has a better electrolyte film.

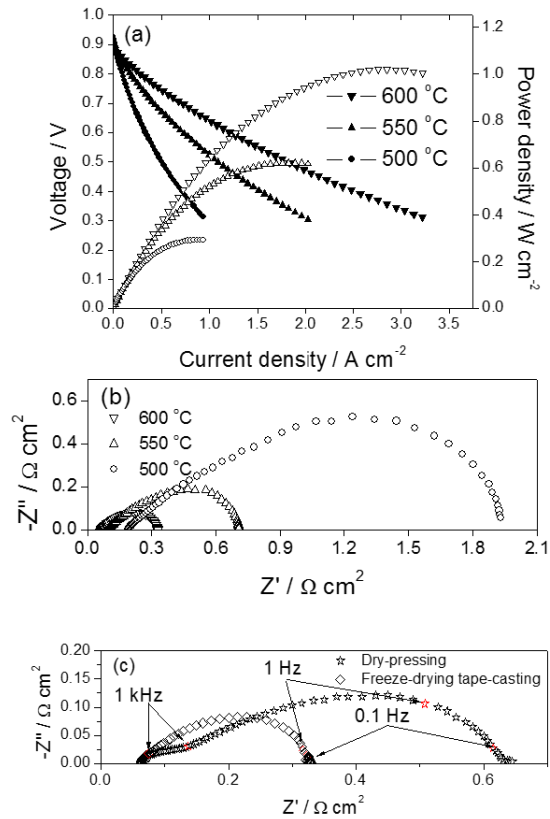


Figure 3.5 (a) *IV* and *IP* curves of cell measured at different operating temperature using hydrogen as fuel and ambient air as oxidant; (b) Impedance spectra of cells tested at different temperature under open circuit conditions; (c) Comparison of EIS for the cell with anode substrate through dry-pressing and freeze-drying tape-casting.

As shown in Figure 3.5 (a), the maximum cell power densities ( $P_{\max}$ ) achieved are 0.292, 0.622, and 1.021 Wcm<sup>-2</sup> at 500, 550 and 600 °C, respectively, almost two times higher than the values for either the dry-pressed cell (at 600 °C,  $P_{\max}$  for dry-pressed cell is only 0.489 W cm<sup>-2</sup>) or other reported cell performance with similar cell materials and under similar testing conditions but with the traditional sponge-like microstructure of the anode[63, 75]. The cell power output in this study using LSCF-GDC cathode is also comparable to the cell power output with Ba<sub>0.5</sub>Sr<sub>0.5</sub>Co<sub>0.8</sub>Fe<sub>0.2</sub>O<sub>3</sub> (BSCF) cathode[76],

Table 3. 2 Comparison of maximum cell power density and interfacial polarization resistance measured at 600 °C of anode supported cells based on GDC or Sm<sub>0.2</sub>Ce<sub>0.8</sub>O<sub>2</sub> (SDC) thin film electrolytes.

Cell configuration	$P_{max}$ / Wcm <sup>-2</sup>	$R_p$ / $\Omega$ cm <sup>2</sup>	Ref.
Ni-GDC/GDC(10 $\mu$ m)/LSCF-GDC	0.578	~0.7	[75]
Ni-SDC/SDC(20 $\mu$ m)/BSCF	1.01	--	[76]
Ni-GDC/GDC(16 $\mu$ m)/LSCF	0.65	--	[77]
Ni-GDC/GDC(19 $\mu$ m)/LSCF-GDC	0.39	0.50	[78]
Ni-GDC/GDC(3 $\mu$ m)/LSCF	0.99	--	[79]
Ni-GDC/GDC(30 $\mu$ m)/LSCF-GDC	0.489	0.64	this study (dry-pressing)
Ni-GDC/GDC(30 $\mu$ m)/LSCF-GDC	1.021	0.2675	this study (freeze-drying tape-casting)

which has been reported to have much higher catalytic activity than LSCF cathode, further demonstrating that high cell performance can be obtained by simple anode microstructure modification. Figure 3.5 (b) shows the electrochemical impedance spectra of cells measured at different temperature under open circuit conditions. The ohmic resistance is 0.189, 0.096 and 0.061  $\Omega$  cm<sup>2</sup> at 500, 550 and 600 °C, respectively. The interfacial polarization resistance is 1.743, 0.6108 and 0.2672  $\Omega$  cm<sup>2</sup> at 500, 550 and 600 °C, respectively. Both the cell power density and interfacial polarization resistance obtained in this work are much better than those reported by others using similar cell materials but with cells fabricated from different processes (shown in Table 3.2). For example, a maximum power density of only 0.578 Wcm<sup>-2</sup> and an interfacial polarization resistance of 0.7  $\Omega$ cm<sup>-2</sup> have been reported for SOFCs with a sponge-like porous Ni-GDC anode using the conventional uniaxial dry-pressing method, LSCF-GDC as cathode, and even much thinner GDC electrolyte film (10  $\mu$ m) [75]. For directly comparison, Ni-GDC anode supported cells with GDC film and LSCF-GDC cathode have also been prepared by dry-pressing, drop-coating and screen-printing. The composition and thickness for

anode, electrolyte and cathode are kept same. The only difference is the anode microstructure. At 600 °C, the dry-pressed cells only show a peak power density of 0.489 W cm<sup>-2</sup> and interfacial polarization resistance of 0.64 Ω cm<sup>2</sup> under same conditions.

Figure 3.5 (c) shows the difference of impedance spectra for the cell prepared by dry-pressing and freeze-drying tape-casting. It is generally accepted that the impedance in the high-frequency range corresponds to a combination of anode and cathode charge transfer processes[80], while the impedance in the low-frequency range is associated with a gas diffusion process[81]. Since the electrolyte and cathode are kept the same for the cells made by freeze-drying tape-casting and dry-pressing, the difference in the two cell impedance spectra could be attributed to the anode. The comparison of these two cell spectra provides further evidence that both the activation and concentration polarization resistances have been decreased by applying hierarchically oriented macroporous anode substrate made from the freeze-drying tape-casting process.

### 3.4 CONCLUSIONS

In summary, dense GDC film has been successfully fabricated on hierarchically oriented NiO-GDC substrate by simple and cost-effective combination of drop-coating and co-firing. The porosity distribution and tortuosity factor value along thickness direction have been determined both qualitatively and quantitatively from actual microstructure obtained nondestructively via 3D X-ray microscopy. This is new as traditionally such calculation could be only done based on either 2D microstructure or idealized 3D microstructure. The cells consisting of hierarchically oriented porous Ni-GDC anode, dense GDC thin film electrolyte and LSCF-GDC

cathode show a high cell power output of  $1.021 \text{ Wcm}^{-2}$  at  $600 \text{ }^\circ\text{C}$ , which is almost two times higher than the values previously reported for cells with similar cell materials but with different Ni-GDC anode microstructure. Hierarchically oriented pores/channels in the anode leads to a low interfacial polarization resistance and consequently high cell power output. The method to fabricate dense thin film on a hierarchically oriented porous substrate developed in this study can have broad applications in fuel cells and gas separation membranes.

## CHAPTER 4 LOW TEMPERATURE SOLID OXIDE FUEL CELLS WITH HIERARCHICALLY POROUS CATHODE NANO-NETWORK

### 4.1 BACKGROUND

As demonstrated in previous chapters, inexpensive materials can be used for interconnects, heat exchangers, manifolding and other structural components of the SOFC system[82] when the operation temperature can be reduced to low temperature. A lower operating temperature would also ensure greater overall system stability due to a reduction in the thermal stresses in the active ceramic structures, leading to a longer lifetime for the SOFC system. At the same time, lowering the operating temperature is expected to improve the SOFC durability since oxidation, corrosion, chemical interdiffusion and creep deformation will be alleviated at reduced operating temperatures. In addition, lowering the SOFC operation temperature can also offer quick start-up ability, which in turn can enable their use in applications such as transportable power sources and auxiliary power units for automobiles. However, by reducing operation temperature, the overall electrochemical performance of an SOFC system will be significantly decreased due to the increased polarization resistances of the electrode reactions. Further, the cathode has been the center of the focus in the electrode

development largely because oxygen reduction is more difficult to be activated in SOFCs operating at commercially relevant temperatures [83, 84]. Consequently, it is critically important to develop new cathode materials or novel cathode microstructures with low polarization loss to maintain sufficient high electrochemical activity to enable SOFC operating at temperatures of below 600 °C [39, 40].

Nanoscale materials have been widely developed as catalysts in SOFCs because of their advantageous catalytic properties related to the enhanced surface vacancy concentration and increased ionic and electronic conductivities [85-88]. The nano-structured SOFC electrodes made through ion-infiltration and/or liquid combustion could take advantage of both high electro-catalytic activity and extended TPB length[35]. The SOFC electrode catalyst precursor solution for infiltration normally includes a homogeneous mixture of raw materials with chelants/fuel at the atomic scale, which successfully overcomes the diffusion obstacle and ensures a lower synthesis temperature[89]. Although tremendous success has been made in synthesis and application of nano-oxides by liquid combustion method [89-91], the limitations for application in SOFCs such as particle agglomeration and phase impurities are also obvious. First, agglomerates form readily during the synthesis process since both the concentrated glycine-nitrate gel after water evaporation and the high flame temperature (1100 to 1450 °C) during combustion promote the growth of particle size[92]. Second, in the synthesis of complex oxides typically used as SOFC electrodes, impure phases are frequently observed in the primary products from the auto-combustion process. These impurities are due to the low conditional stability constant of glycine-metal chelates[93]. Pure perovskite phase was only obtained after a further heat treatment of the combustion synthesized primary powders at higher temperature[94],

however, which would result in a significant reduction in surface area and coarsening of powders.

In this chapter, we have fabricated a hierarchically porous  $\text{Sm}_{0.5}\text{Sr}_{0.5}\text{CoO}_3\text{-Gd}_{0.1}\text{Ce}_{0.9}\text{O}_{2-\delta}$  (SSC-GDC) cathode with SSC nano-network by a combination of freeze-drying and combustion of SSC-GDC precursors using glycine as the chelating agents (denoted as FC-G). Freeze-drying, based on the dehydration by sublimation of a frozen product under vacuum, is one of the most effective processes of water removal with final products of highest quality in food storage industry[95]. During freeze-drying, solid ice protects the primary structure and the shape of the products with high porosity and minimal reduction in volume. Inspired by this feature, SSC solution (with glycine as chelant) was first infiltrated and then frozen into GDC scaffold and then freeze-dried under vacuum. A solid macroporous glycine-nitrate matrix with minimal volume reduction after freeze-drying and a rough SSC nano-network after subsequently combustion has been formed. The single cells, consisting of Ni-GDC anode, GDC electrolyte and SSC-GDC cathode, have been fabricated. The microstructures of as-prepared SSC powder, electrodes and single cells, X-ray diffraction (XRD) of SSC-GDC composite cathode and SSC powder and single cell performance have been systematically evaluated.

## 4. 2 EXPERIMENTAL

### 4.2.1 Fabrication and characterization of powders

$\text{Co}(\text{NO}_3)_2 \cdot 6\text{H}_2\text{O}$ ,  $\text{Sm}(\text{NO}_3)_3 \cdot 6\text{H}_2\text{O}$  and  $\text{Sr}(\text{NO}_3)_2$  were purchased from Alfa Aesar in this study. Precursor solutions for SSC were prepared by mixing the desired mole ratio of three nitrates with de-ionized water for 12 h. For solutions with glycine, the ratio of

glycine/nitrate is 1:2. For convenience, the traditional-combustion processes with and without glycine was denoted as TC-G and TC, respectively, while the freeze-drying combustion processes with and without glycine were denoted as FC-G and FC, respectively. In traditional-combustion approaches (TC and TC-G), the SSC solution was dried in an oven at 80 °C for 12 h and then the nitrate salt was heat-treated at 1000 °C for 2 h. In freeze-drying combustion approaches (FC and FC-G), the precursor solutions for SSC were poured onto a frozen bed (-70 °C). After frozen, the solid SSC/ice crystals were moved into a freeze dryer under a vacuum of 100 mtor at -30 °C for 12 h and then at 30 °C for another 12 h. After water was sublimated, the SSC crystals were heated in a furnace at 1000 °C for 2 h.

The crystalline structure of SSC-GDC composite cathode and SSC powders was studied by X-ray diffraction (XRD) analysis over the  $2\theta$  range of 20-80 degree with a scanning rate of 1 degree  $\text{min}^{-1}$  on a D/MAX-3C X-ray diffractometer with graphite-monochromatized  $\text{CuK}\alpha$  radiation ( $\lambda=1.5418 \text{ \AA}$ ).

#### *4.2.2 Fabrication and characterization of solid oxide fuel cells*

NiO (Sigma-Aldrich, USA) and GDC ( $\text{Gd}_{0.1}\text{Ce}_{0.9}\text{O}_{2-\delta}$ , Fuel Cell Materials, USA) powders were purchased in this study. The NiO-GDC anode substrate and GDC cathode skeleton were fabricated by a freeze-drying tape-casting process[69, 96]. The GDC electrolyte slurry was directly deposited on the green NiO-GDC substrate by drop-coating. GDC substrate was then laminated on the GDC green film surface. The NiO-GDC anode|GDC electrolyte film|GDC cathode scaffold tri-layers were then co-fired at 1450 °C for 12 h at a heating rate of 1 °C  $\text{min}^{-1}$  before 600 °C and 2 °C  $\text{min}^{-1}$  after 600 °C. The SSC solutions were dropped into the GDC scaffold and then the scaffold was either

frozen on a freezing bed and freeze-dried or dried in an oven at 80 °C for 12 h. The skeleton with SSC nano particles and fuel cells were then heat-treated at 1000 °C for 2 h. The cycle was repeated several times until the mass ratio of SSC and GDC in the cathode is about 1:1. The diameters for the anode/electrolyte bilayer and the cathode are ~16 and ~9.5 mm, respectively. The SSC loading level can be determined by measuring the weight difference after each cycle. The skeletons with nano particles were also prepared and then ground for XRD measurement.

The microstructure of the fuel cells was characterized using a scanning electron microscope (SEM, Zeiss Ultra plus FESEM). High resolution transmission electron microscopy (HRTEM) image of cathode after 500 h stability measurement was acquired using a JEOL 2100F TEM equipped with a Schottky field-emission gun (FEG) with Cs=1.0 mm operated at 200 kV. The HRTEM morphology of SSC powders obtained from the four different approaches was characterized using JEOL 3000F with a point-to-point resolution of 0.17 nm operating at 300 kV. The BET surface areas and pore size distributions of the SSC powders obtained from the four different approaches were determined using a Quantochrome NOVA 2000 high-speed surface area and pore size analyzer. The current density-voltage curves as well as impedance spectra of the fuel cells were measured with a four probe method using a multi-channel Versa STAT (Princeton Applied Research) at an operating temperature range of 400-500 °C. Humidified (3 vol% H<sub>2</sub>O) hydrogen was used as fuel while ambient air was used as oxidant. Hydrogen flow rate was controlled at 40 sccm by a mass flow controller (APEX, Alicat Scientific). The electrochemical impedance spectra of cells were measured under open circuit voltage over a frequency range of 1 MHz to 0.1 Hz. The cell polarization

resistance ( $R_p$ ) was determined from the difference between the low and high frequency intercepts of the impedance spectra with the real axis in the Nyquist plot.

### 4.3 RESULTS AND DISCUSSION

Figure 4.1 shows the typical cell performance of the anode supported SOFCs (with a cell configuration of Ni-GDC|GDC|SSC-GDC) using humidified (3 vol% H<sub>2</sub>O) hydrogen as fuel and ambient air as the oxidant operated at temperatures of 400, 450 and 500 °C, respectively. The performance reported in this study was the one we most often obtained from several measurements under the same testing conditions. As indicated in Figure 4.1 (a), the open circuit voltages (OCVs) of cells are 0.943, 0.923 and 0.907 V at 400, 450 and 500 °C, respectively. The cell maximum power density  $P_{max}$  of 0.65 W cm<sup>-2</sup> was achieved at 500 °C. Figure 4.1 (b) shows the impedance spectra of the cells at 400, 450 and 500 °C, respectively, under open circuit conditions. The cell ohmic resistance, corresponding to the high frequency intercept of the impedance spectra with the real axis in the Nyquist plot, is 0.38, 0.21 and 0.14 Ω cm<sup>2</sup> at 400, 450 and 500 °C, respectively. The cell polarization resistance,  $R_p$ , determined from the difference between the high and low frequency intercepts of the impedance spectra with the real axis, is 1.06, 0.42 and 0.15 Ω cm<sup>2</sup> at 400, 450 and 500 °C, respectively. The cell performance is much better than those reported with similar cell materials set [69, 76, 97-99] in which the electrodes have the traditional sponge-like microstructure, as shown in Table 4.1. For example, the best ever reported  $P_{max}$  for similar cells (with sponge-like porous cathodes) by other group was 0.48 W cm<sup>-2</sup> at 500 °C[98], 26 % less than our current result at the same testing conditions. In that report, the electrolyte thickness is even thinner (only 9 μm) compared with that in this study (~30 μm). The cell performance in this work is even better than the

one reported with  $\text{La}_{0.8}\text{Sr}_{0.2}\text{Ga}_{0.83}\text{Mg}_{0.17}\text{O}_3$  (LSGM) electrolyte[90], in which the cell had an OCV of 1.11 V and  $P_{\text{max}}$  of  $0.47 \text{ W cm}^{-2}$  at  $500 \text{ }^\circ\text{C}$ , further indicating that the hierarchically porous SSC-GDC cathode in this study shows a superior oxygen reduction reaction (ORR) catalytic activity. In addition, the nano SSC-GDC hierarchically porous cathode in our study shows an impressive power output stability at  $400 \text{ }^\circ\text{C}$ , confirmed by the stability test for more than 500 h (Figure 4.1 (c)).

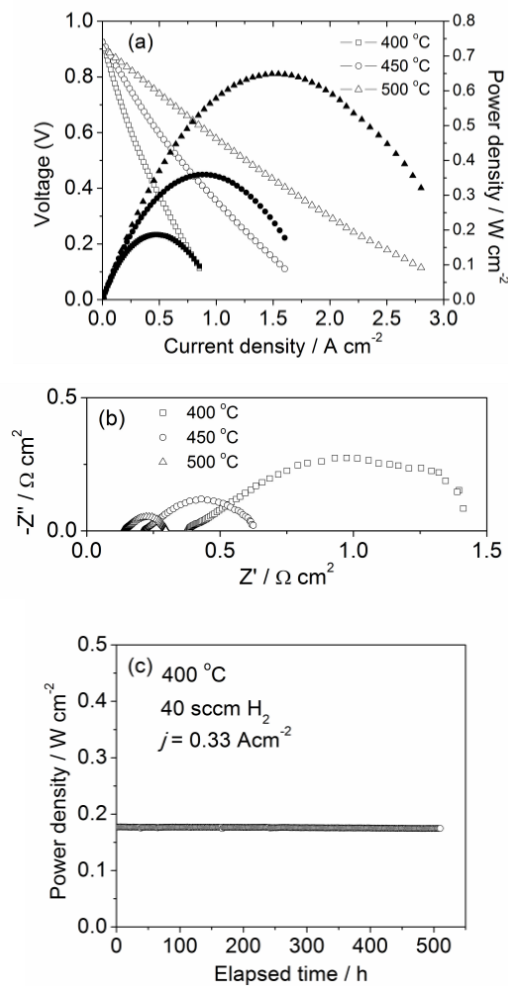


Figure 4.1 (a) Typical  $I-V$  and  $I-P$  curves and (b) Electrochemical impedance spectra for the cell with hierarchically porous rough SSC-GDC cathode nano-network prepared from the FC-G method at 400, 450 and 500 °C, respectively. (c) Power density as a function of time at 400 °C for the cell with SSC-GDC cathode made from the FC-G method operated at a constant current load of  $0.33 \text{ A cm}^{-2}$ .

Table 4. 1 Peak power density ( $P_{max}$ ) and polarization resistance ( $R_p$ ) at 500 °C for SOFCs with hydrogen as fuel.

Cell configuration	$P_{max}$ [Wcm <sup>-2</sup> ]	$R_p$ [Ω cm <sup>2</sup> ]	Ref.
Ni-GDC/GDC(20 μm)/SSC-GDC	0.15	0.68	[97]
Ni-SDC/SDC(9 μm)/SSC-GDC	0.48	0.26	[98]
Ni-SDC/SDC(20 μm)/BSCF	0.40	0.135	[76]
Ni-SDC/SDC(10 μm)/SSC-SDC	0.44	0.21	[99]
Ni-GDC/GDC(30 μm)/SSC-GDC	0.52	0.18	[69]
Ni-LSGM/LSGM(60 μm)/SSC-LSGM	0.47	--	[90]
Ni-GDC/GDC(30 μm)/SSC-GDC	0.65	0.15	This study

The enhanced cell performance could be ascribed to the novel microstructure of the cell, especially the SSC-GDC cathode, as indicated in Figure 4.2, which shows the X-ray microscopy, reconstructed 3D and scanning electron microscope (SEM) and high resolution transmission electron microscope (HRTEM) images for the cell and cathode made through freeze-drying combustion. The images were taken from the cell and the cathode after the cell performance stability test at 400 °C for more than 500 h. Figure 4.2 (a) shows the 3D X-ray microscopic image (a<sub>1</sub>) and cross-sectional view (a<sub>2</sub>) of the cell with cathode (top), electrolyte (middle) and anode (bottom) tri-layer. The dimension for the cell in (a) is around 4.43×4.43×0.74 mm. Figure 4.2 (b) shows the reconstructed 3D microstructure images for the cell with cathode (top), electrolyte (middle) and anode (bottom) from subdomain in (a). To the best of our knowledge, this is the first reconstructed 3D image for the entire cell with such dimensions. The detail about the reconstruction can be found in our previous study[96]. As shown in Figure 4.2 (c), the cell has a thick graded open porous Ni-GDC anode layer (~500 μm), a thin dense GDC electrolyte layer (~30 μm) and a thick graded open porous SSC-GDC cathode layer (~200 μm). Both the anode and cathode are well adhered to electrolyte. Figure 4.2 (d) shows a magnified image of the SSC-GDC cathode while Figure 4.2 (e) shows an enlarged view

for the SSC nano aggregates. Compared with the SEM images for the SSC-GDC cathode produced from the three other methods (i.e. traditional combustion method with and without glycine and freeze-drying combustion without glycine as the chelating agent, denoted as TC-G, TC and FC, respectively) (Figure 4.3), it can be seen that the SSC-GDC cathode made from FC-G contains fine and homogeneously distributed SSC particles linked together, forming a three dimensional (3D) nano-network. The unique graded porous Ni-GDC anode and SSC-GDC cathode microstructure is expected to facilitate mass and heat transport, while the novel 3D nano-sized SSC network will be beneficial for the electrochemical reduction of oxygen. It is worth mentioning that, as shown in Figure 4.2 (e), the SSC nano-aggregates (200-600 nm in size) consist of fine SSC particles (6-10 nm in diameter), as confirmed by HRTEM image in Figure 4.2 (f), which could be attributed to the limited contact between particles during freeze-drying and subsequent combustion. A lattice distance of around 0.25 nm has been revealed, consistent with the 0.25 nm distance between two (210) planes of SSC crystalline structure (space group Pnma) determined by the X-ray diffraction (XRD) analysis. The size of pores on the surface of SSC aggregates is around 10 nm, similar to a pore size of 6.67 nm obtained from Brunauer-Emmett-Teller (BET) analysis of the SSC powders made from the freeze-drying combustion of the SSC precursors using glycine as the chelating agent.

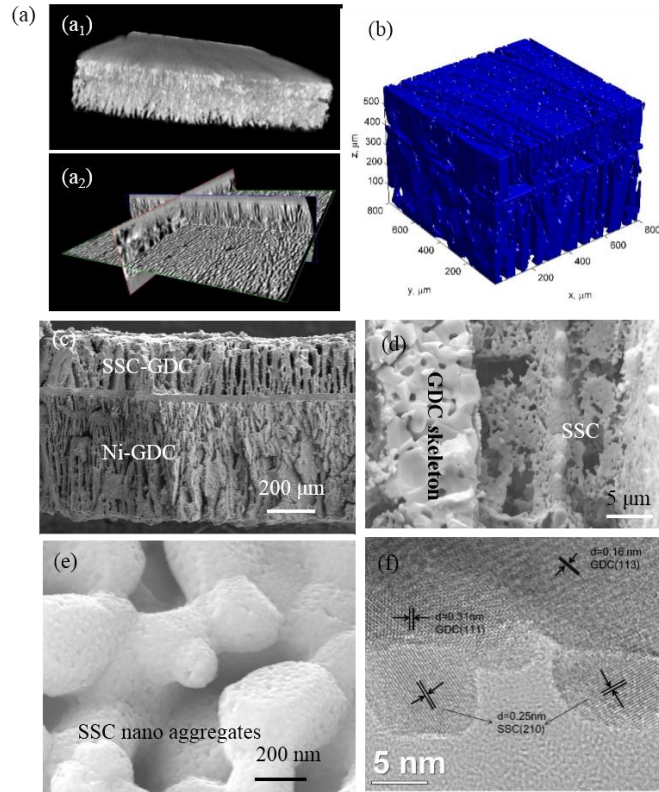


Figure 4.2 3D X-ray microscopic image (a) for the cell consisting of anode (bottom layer), electrolyte (middle layer) and cathode (top layer) (a<sub>1</sub>) and cross-sectional view of X-ray microscopic image showing internal gas diffusion channel (a<sub>2</sub>). Reconstructed 3D image for single cell (b), SEM images for the cross-section of the cell (c), the cathode (d,e), and high resolution TEM (HRTEM) image for the surface of SSC-GDC cathode after electrochemical measurement (f).

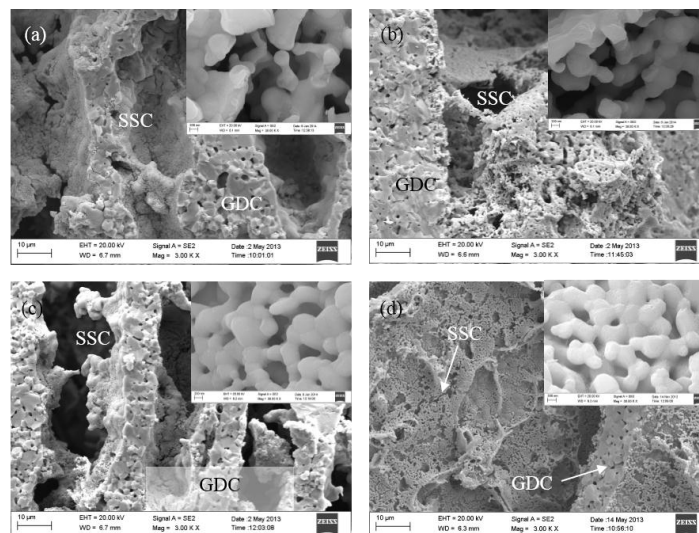


Figure 4.3 The SSC-GDC cathodes prepared by (a) traditional combustion method without glycine as the chelating agent (TC), (b) traditional combustion method with glycine as the chelating agent.

glycine as the chelating agent (TC-G), (c) freeze-drying combustion without glycine as the chelating agent (FC), and (d) freeze-drying combustion with glycine as the chelating agent (FC-G). Insets are enlarged SSC particles views respectively.

The tortuosity factors of pores in anode and cathode have been calculated by solving Laplace's equation with the 3D reconstructed structure. Figure 4.4 shows the solutions of a general field distribution within the pores domains of anode (a) and cathode (b), by using which the tortuosity factors for anode and cathode have been calculated as 1.3 and 1.4, respectively. The detail can be found in our previous report[48]. Inserting the tortuosity factor and other parameters into Equation (1.12) and (1.13) in Chapter 1, the diffusion resistances of anode and cathode have been calculated as 0.0128 and 0.0025  $\Omega\text{cm}^2$  at 500 °C, respectively. The unique microstructure of Ni-GDC anode and SSC-GDC cathode with high porosity (~50 vol%) and low tortuosity factor (~1.3 for the anode and 1.4 for the cathode, is expected to facilitate gas diffusion into the reaction area and increase surface reactant concentration, thus increasing the exchange current density  $i_0$  and limiting current density  $i_L$ , as estimated by the equations 1.5, 1.6 and 1.11 in Chapter 1. Therefore, the activation and concentration polarization loss can be decreased.

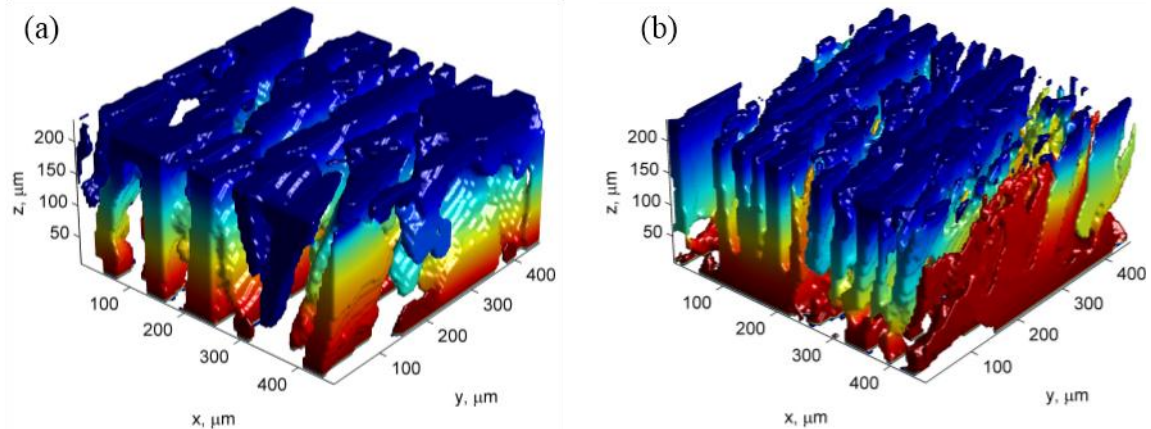


Figure 4. 4 Distributions of a general field within the 3D pore domains of anode (a) and cathode (b). Colors scale with the potential of the field.

The unique cathode microstructure could be attributed to the features obtained from both glycine and freeze-drying. The glycine can form stable complexes with metal ions to increase solubility and prevent precipitation of metal ions during water removal. Large volume of gases generated during the combustion process limit the inner-particle contact. Compared with traditional solution-combustion method, freeze-drying can form a glycine/nitrate solid macroporous matrix instead of a concentrated glycine-metal gel, further alleviating precipitation and agglomeration issues. Therefore, the precursor complex oxide ash obtained from combustion is generally composed of very fine and loose particles with desired stoichiometry linked together in a network. The cathode

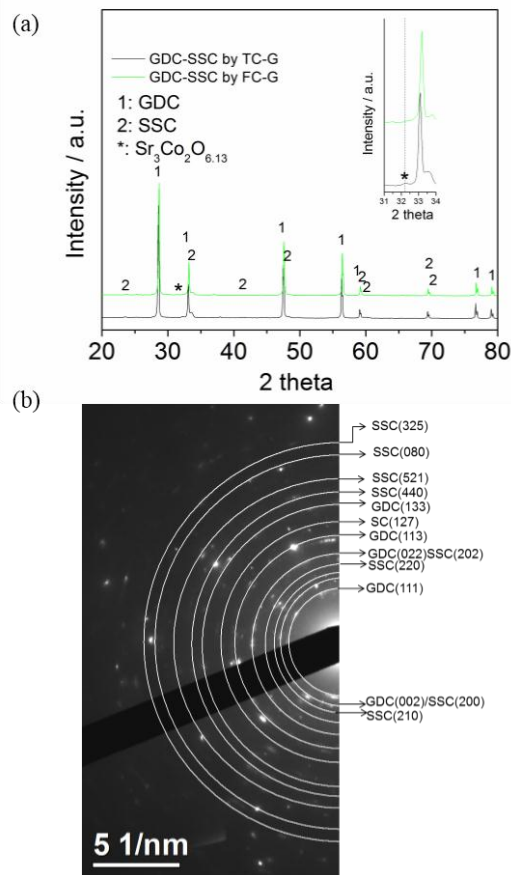


Figure 4. 5 (a) XRD pattern for SSC-GDC electrode heat-treated at 1000 °C and (b) Selected area electron diffraction (SAED) pattern for the SSC-GDC cathode particles heat-treated at 1000 °C.

(GDC skeleton and SSC nano particles) was fabricated through freeze-drying combustion (FC-G) and heat-treated at 1000 °C for 2 h for subsequent XRD measurement. As shown in Figure 4.5 (a), the XRD patterns indicated a good phase crystallinity of perovskite and fluorite structure. The XRD pattern for FC-G, shown in inset in Figure 4.5 (a), indicated that less impurities ( $\text{Sr}_3\text{Co}_2\text{O}_{6.13}$ , denoted as SC,  $2\theta \sim 32.20^\circ$ , PDF#83-0375, which can be easily found in SSC preparations [94, 100]), can be detected when compared with traditional combustion method (TC-G). Prior studies [94] on the synthesis of SSC by combustion method have demonstrated that such SC impurity phase can only be eliminated by sintering at least 1200 °C. However, calcination at such high temperature will have low porosity and microstructure not favorable as cathode materials. Selected area electron diffraction (SAED) pattern for the GDC/SSC composite cathode after calcination at 1000 °C was collected and shown in Figure 4.5 (b). The ring pattern was carefully measured and compared with JCPDS-PDF No. 75-0161 (GDC), No. 53-0112 (SSC) and No. 83-0375 (SC). It was found that most of the circles fitted well with the GDC and SSC respectively, only small contents of diffraction from SC (127) plane could be detected, consistent with XRD analysis (Figure 4.5 (a)). Therefore, it can be concluded that the freeze-drying combustion could provide an efficient approach to obtain SSC phase with less impurities.

To further study the advantageous properties of SSC powders prepared by such an approach (FC-G), SSC powders by other three approaches, i.e. TC, TC-G and FC were also prepared and characterized. XRD for SSC powders by FC-G was shown in Figure 4.6 (a), showing crystalline SSC structure (space group Pnma, PDF#53-0112). Compared with the XRD patterns for SSC powders prepared by the other methods (Figure 4.7),

XRD peak corresponding to  $\text{Sr}_3\text{Co}_2\text{O}_{6.13}$  (SC) (around  $32.40^\circ$ , PDF#83-0375) is not observable for SSC powders from FC-G method, which could be attributed to the high homogeneity of metal nitrates and glycine mixture obtained during the freeze drying

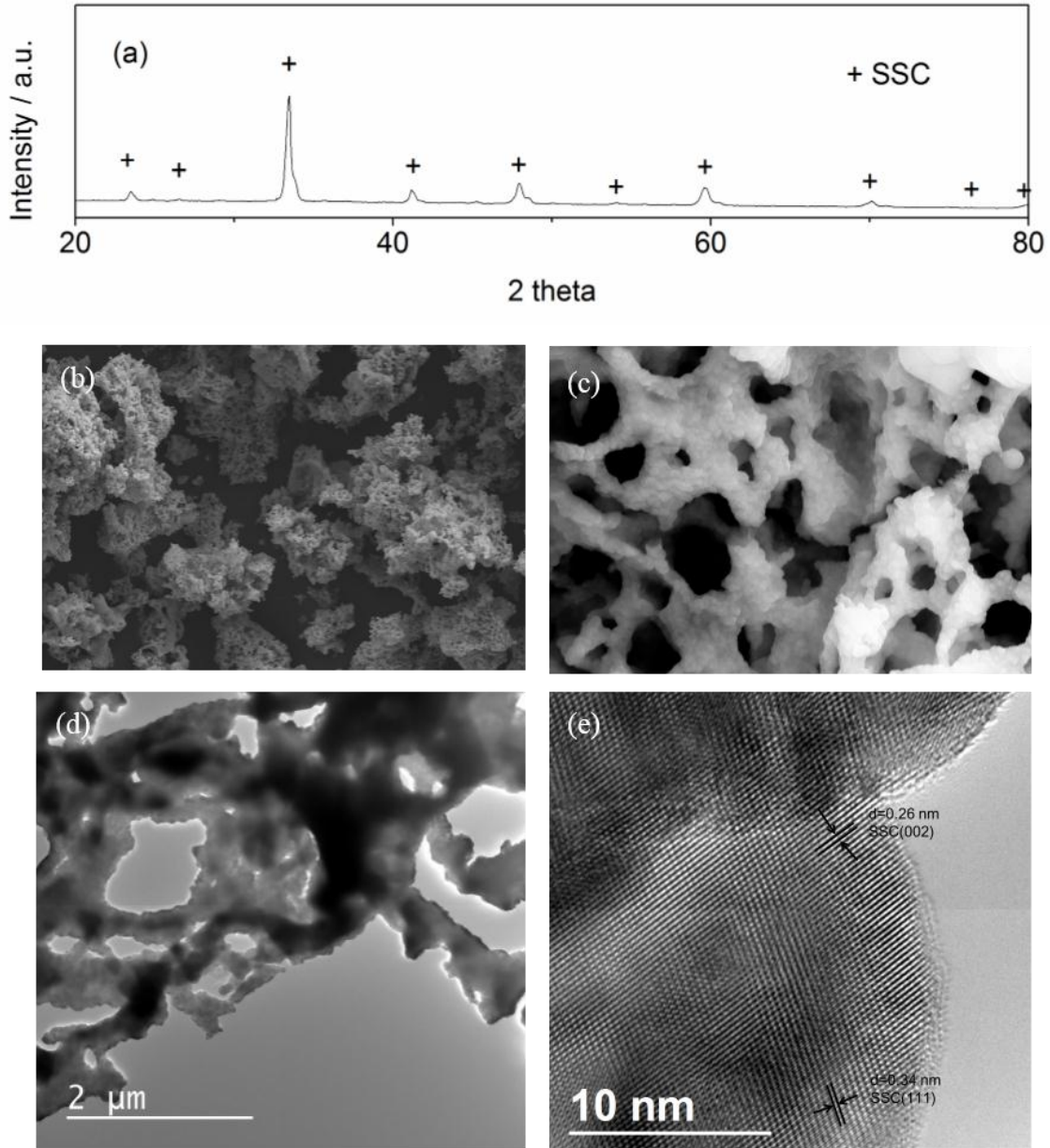


Figure 4. 6 (a) XRD pattern, (b) low magnification SEM, (c) high magnification SEM and (d) Bright field (BF) TEM and (e) High resolution TEM (HRTEM) for the SSC powder prepared by freeze-drying combustion method. The powder was heat-treated at  $1000^\circ\text{C}$  for 2 h.

process. Low magnification SEM image (Figure 4.6 (b)) reveals that the SSC powders made from the FC-G method are loose and porous agglomerates. The measured BET area for such SSC powders (after calcination at 1000 °C for 2 h) is 1.3690 m<sup>2</sup>g<sup>-1</sup>, higher than the SSC powders made from the TC-G method (0.7561 m<sup>2</sup>g<sup>-1</sup>) and the SSC powders prepared by self-rising method (0.56 m<sup>2</sup>g<sup>-1</sup>) that we reported earlier[101]. SSC powders made from the FC-G method show very fine particles (around 0.2 μm), smaller than those by the other three combustion methods (0.5-1 μm) (Figure 4.8), which could be attributed to the limited metal nitrate/particle contact during freeze-drying process and large volume of gases generated during the combustion process. Such a fine and porous microstructure is expected to provide efficient transport pathways to the SSC interior active surfaces. The porous microstructure and nano-sized particles of SSC powders made from the FC-G method are confirmed by transmission electron microscopy (TEM) images shown in Figure 4.6 (d), Figure 4.9. The HRTEM analysis of SSC powders made from the FC-G method has revealed a lattice spacing of 0.26, 0.34 nm (Figure 4.6 (e)), match well with the (002), (111) plane of the SSC crystalline structure respectively.

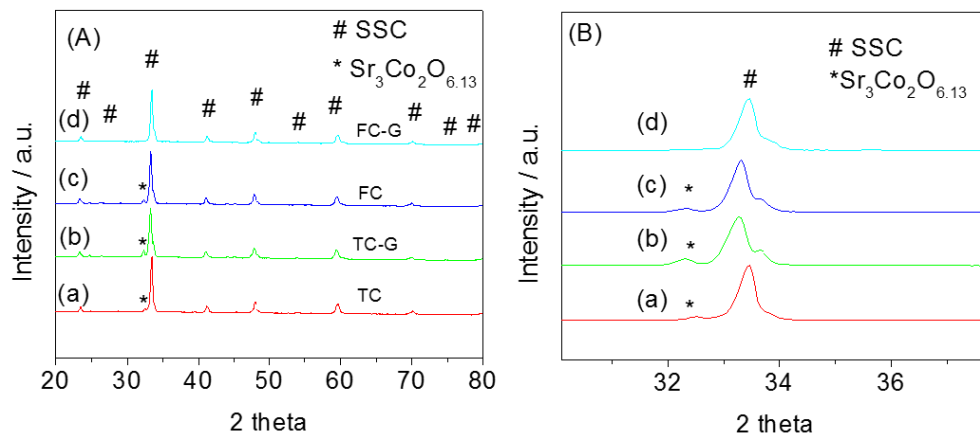


Figure 4. 7 XRD patterns for SSC powders prepared by (a) traditional combustion without glycine as the chelating agent (TC), (b) traditional combustion with glycine as

the chelating agent (TC-G), (c) freeze-drying combustion without glycine as the chelating agent (FC) and (d) freeze-drying combustion with glycine as the chelating agent (FC-G). The pattern (A) is from 20 to 80 degree. The pattern (B) is the zoomed area around the highest peak.

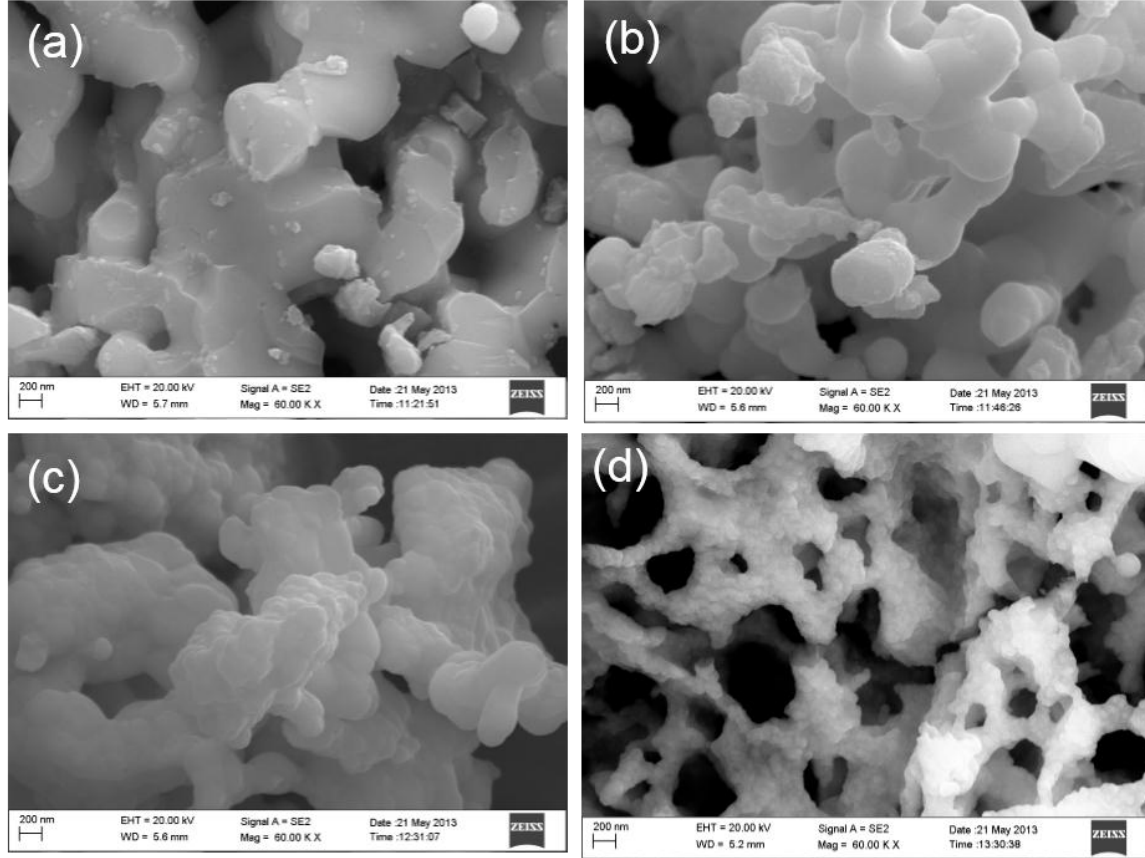


Figure 4. 8 SEM images (high magnification) for SSC powders (heat-treated at 1000 °C/2h ) by (a) traditional combustion without glycine as the chelating agent (TC), (b) traditional combustion with glycine as the chelating agent (TC-G), (c) freeze-drying combustion without glycine as the chelating agent (FC) and (d) freeze-drying combustion with glycine as the chelating agent (FC-G).

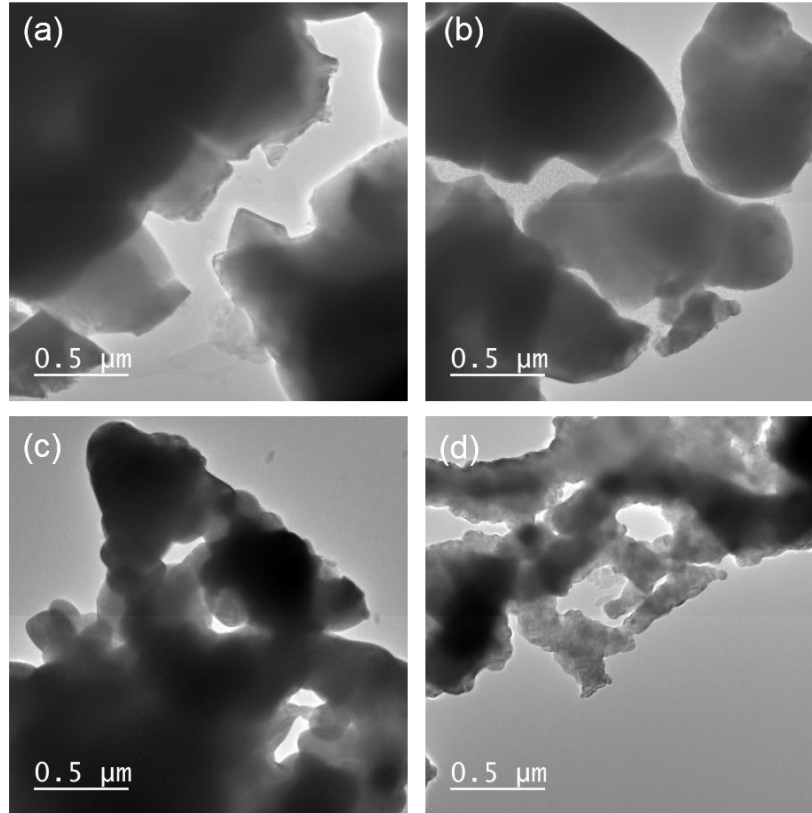


Figure 4.9 Bright field TEM images (high magnification) for SSC powder (heat-treated at 1000 °C/2h ) by (a) traditional combustion without glycine as the chelating agent (TC), (b) traditional combustion with glycine as the chelating agent (TC-G), (c) freeze-drying combustion without glycine as the chelating agent (FC) and (d) freeze-drying combustion with glycine as the chelating agent (FC-G).

The fuel cells with different SSC-GDC cathode microstructures made through the other three methods, i.e. TC, TC-G and FC have been characterized. Performance of the fuel cells using the porous SSC-GDC cathode with fine SSC particles of nano-network microstructure is much better than the others as shown in Figure 4.10 (A). For example, at 600 °C, cells with the SSC-GDC cathode made from the FC-G method show peak cell power output of 1.44 Wcm<sup>-2</sup>, while those by TC, TC-G and FC show a peak power output of 0.494, 0.987 and 0.732 Wcm<sup>-2</sup>, respectively. Figure 4.10 (B) displays the impedance spectra showing the total cell polarization resistance for the different cells. At 600 °C,

cells with SSC-GDC cathode made from the FC-G method have a cell polarization resistance as low as  $0.05 \Omega \text{ cm}^2$ , while those cells with SSC cathode made through TC, TC-G and FC show polarization resistance of around 0.30, 0.10 and  $0.22 \Omega \text{ cm}^2$ , respectively. Considering the only difference from those cells comes from the different method to fabricate the SSC-GDC cathode, such dramatic cell performance difference could be resulted from the different phase purities and microstructure of the SSC-GDC cathode. The impurity phases in SSC powders made from TC, TC-G and FC methods may block oxygen surface adsorption thus deteriorating the cathode performance[94]. The hierarchically porous SSC-GDC cathode with nano-sized SSC catalyst made by the FC-G method may significantly facilitate mass transport, extend the effective TPB length and increase reaction sites, thus accelerating oxygen reduction process.

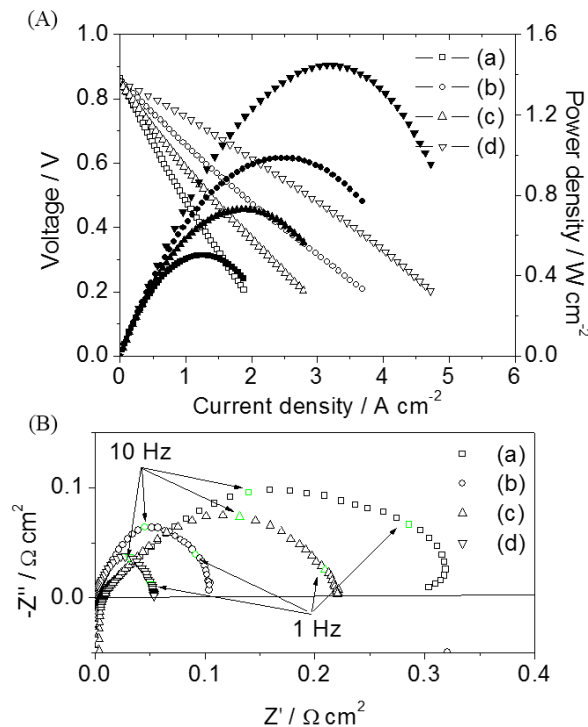


Figure 4.10 *I-V* and *I-P* curves (A) and Electrochemical impedance spectra curves (B) at  $600 \text{ }^\circ\text{C}$  for the cell with SSC-GDC cathode prepared by (a) traditional-combustion with

no glycine (TC), (b) traditional-combustion with glycine (TC-G), (c) freeze-drying combustion with no glycine (FC) and (d) freeze-drying combustion with glycine (FC-G) method, respectively

#### 4.4 CONCLUSIONS

In summary, a hierarchically porous SSC-GDC cathode with fine SSC particles has been successfully synthesized by a combination of freeze-drying and combustion approach. Compared with the traditional solution combustion synthesis methods, freeze-drying combustion is unique and more efficient to obtain three dimensional cathode networks with fine particles and high phase purity. Fuel cells with hierarchically oriented porous electrodes, GDC thin film, and nano-network SSC cathode catalyst show an excellent cell power output of  $0.65 \text{ W cm}^{-2}$  at  $500 \text{ }^\circ\text{C}$ , the highest cell power output ever achieved with the same cell materials. The presence of graded straight open pores facilitates mass transport while hierarchically porous cathode with SSC nano-network accelerates the electrochemical reduction of oxygen. The novel freeze-drying combustion approach could potentially be a general method to synthesize nano-network fine particles for application in catalysis and energy conversion and storage devices.

# CHAPTER 5 DIRECT-METHANE SOLID OXIDE FUEL CELL WITH HIERARCHICALLY POROUS Ni-BASED ANODE DEPOSITED WITH NANO CATALYST LAYER

## 5.1 BACKGROUND

SOFCs using oxide ion conducting electrolytes have been recognized as the most promising energy conversion device since in principle they can directly operate on fuels ranging from hydrogen to hydrocarbons and even biomass. However, direct operation of hydrocarbon fuels in SOFCs often leads to rapid coking of the state-of-the-art nickel cermet anodes [18, 102, 103]. Carbon adsorbs strongly on Ni surface and thus blocks the active site for electrochemical reactions[104], resulting in rapid performance degradation. The use of external steam reforming or partial oxidation of hydrocarbon fuel is an option, but that will lead to reduced system efficiency and additional cost and complexity of the SOFC system [105, 106]. Another strategy is to develop new anode materials such as perovskite oxides with improved coking resistance[104, 107]. Although these new materials are promising, the catalytic activity towards hydrocarbon fuel and electrical conductivity under anodic atmosphere are still much lower than those of the conventional Ni-based anodes.

Ni-based anodes are still the best choice for SOFCs in terms of low cost, high electrical conductivity, excellent catalytic activities, good manufacturability and chemical compatibility. Consequently, it will be scientifically significant and commercially valuable if Ni-based anodes can be modified to possess coking resistance. Zhan and Barnett first demonstrated that Ru-CeO<sub>2</sub> could be used as an anode catalyst reforming layer when deposited on the outer surface of Ni-yttria-stabilized zirconia (Ni-YSZ) anode and reform hydrocarbons to syngas to prevent coking[28]. Therefore, the direct exposure of Ni-YSZ anode to hydrocarbon fuels has been limited. The cell showed stable power output when operating on iso-octane-air-CO<sub>2</sub> mixture as fuel but had a drawback of gas diffusion through catalyst layer to the Ni-based anode. To avoid the gas diffusion issue, Sun et al have achieved enhanced cell performance through microstructure improvement using mesoporous flower-like Ru-CeO<sub>2</sub> as catalyst layer to Ni based anode[30]. However, the high loading of Ru makes it less economically attractive. Recently, Suzuki et al have applied pure CeO<sub>2</sub> as the catalyst reforming layer on the Ni-based anode surface for low temperature SOFCs operated on methane-H<sub>2</sub>O mixture as fuel[31]. The cell peak power density with reforming layer was more than 10 times higher than that without the reforming layer, confirming that the catalyst layer enhanced the catalytic activity of the steam reforming of methane. However, limitations of introducing this reforming layer are obvious. The poor thermal-mechanical compatibility between catalyst layer and anode layer often caused delamination during thermal cycling, making it less practically feasible[108]. Further, it is challenging to collect current in the anode due to the poor electrical conductivity of the CeO<sub>2</sub> catalyst layer.

Recently, novel microstructured substrates with straight open pores/channels (5-200 μm

in size) have been prepared by freeze-drying tape-casting[50] and developed as solid oxide fuel cell electrodes[42, 43, 47, 68, 69]. The open pores/channels not only facilitate gas diffusion but also function efficiently as catalyst support. In this chapter, for the first time, we have deposited a thin nanoscale catalyst layer on the inner wall surface of Ni-based anode gas diffusion channel via a combination of freeze-drying tape-casting and vacuum-free infiltration. Infiltration has been considered as a strategy to alleviate the issues associated with thermal expansion and conductivity mismatch[86, 109, 110]. Therefore, such a novel combination provides much more freedom to select high performance catalysts even with poor thermal compatibility with the Ni-based anode or with limited electrical conductivity. The continuously graded macro pores/channels with porosity of around 50 vol % and tortuosity factor of  $\sim 2$ [42, 68], are not only beneficial for gas delivery in the electrodes but also for facile solution penetration during infiltration. Through infiltration, ceria solution would first soak in the gas diffusion channel and ceria particles would finally be formed on the surface of the Ni-based channel wall upon drying and combustion. Taking the advantages of the unique microstructure of the Ni-based anode substrate and catalyst infiltration, a thin nanoscale samaria doped ceria (SDC) catalyst layer has been uniformly deposited in the Ni-based anode gas diffusion scaffold. Button cells consisting of Ni-YSZ anode (with and without SDC catalyst layer), thin YSZ electrolyte and  $(\text{La}_{0.80}\text{Sr}_{0.20})_{0.95}\text{MnO}_{3-\delta}$ -YSZ (LSM-YSZ) cathode have been fabricated and evaluated using methane as fuel and ambient air as oxidant. The mechanism for the enhanced anti-coking ability of the anode with deposited nanoscale SDC layer has been investigated. The novel anode design we demonstrated in this chapter can enlarge the selection of catalyst materials for high performance electrochemical devices for various

applications.

## 5.2 EXPERIMENTAL

### 5.2.1 Fabrication of substrates and single cells.

NiO (Sigma-Aldrich, USA), LSM (Fuel Cell Materials, USA) and YSZ (TZ-8YS, Tosoh Company, Japan) powders were purchased in this study. Aqueous based NiO-YSZ (mass ratio of 6:4) slurry was prepared with an ammonium polyacrylate dispersant (Darvan C-N, R.T. Vanderbilt Co., Inc., USA), a thickener (Vanzan, R.T. Vanderbilt Co., Inc., USA), and an acrylic latex emulsion binder system (Duramax HA-12, Rohm & Haas, USA). Solid loading of 25 vol%, freezing bed temperature of  $-70\text{ }^{\circ}\text{C}$ , and Mylar-tape pulling rate of  $48\text{ mm min}^{-1}$  were adopted in this work. The details about NiO-YSZ substrates fabrication can be found in our previous publication[68]. The NiO-YSZ substrate pellets were first pre-sintered at a constant heating rate of  $1\text{ }^{\circ}\text{C min}^{-1}$  to  $600\text{ }^{\circ}\text{C}$  and then at  $2\text{ }^{\circ}\text{C min}^{-1}$  to  $1100\text{ }^{\circ}\text{C}$ . YSZ electrolyte film was then prepared on the pre-sintered NiO-YSZ substrate by a combination of air-brushing and drop-coating method. The NiO-YSZ substrate with electrolyte layer was then co-sintered at  $1350\text{ }^{\circ}\text{C}$  for 5 h. A 0.5 M aqueous solution of  $\text{Ce}(\text{NO}_3)_3 \cdot 6\text{H}_2\text{O}$  (Alfa Aesar, USA) and  $\text{Sm}(\text{NO}_3)_2 \cdot 6\text{H}_2\text{O}$  (Alfa Aesar, USA) mixed with glycine (mole ratio of glycine to cation is 1.5) was dropped on the surface of the NiO-YSZ substrate through infiltration, followed by drying in a oven at  $80\text{ }^{\circ}\text{C}$  for 12 h and firing at  $800\text{ }^{\circ}\text{C}$  for 2 h. The loading of SDC on the NiO-YSZ substrate was determined by weight difference before and after each infiltration/heat-treatment cycle. For X-ray microscope scanning, the NiO-YSZ(anode)|YSZ with and without SDC catalyst layer were reduced at  $800\text{ }^{\circ}\text{C}$  for 12 h under 3 vol% humidified  $\text{H}_2$ . The LSM-

YSZ composite cathode with an active area of  $0.33 \text{ cm}^2$  was prepared on the YSZ surface by screen-printing and then sintered at  $1100 \text{ }^\circ\text{C}$  for 2 h.

### 5.2.2 Characterization.

The microstructure of Ni-YSZ(anode)|YSZ(electrolyte) half cells with and without SDC catalyst layer were characterized using 3D X-ray microscope (MicroXCT-400, Xradia). The cells with and without nano SDC layer were characterized with scanning electron microscope (SEM, Zeiss Ultra plus FESEM). High resolution transmission electron microscopy (HRTEM) image of SDC-deposited anode after stability measurement using methane was acquired using a JEOL 2100F TEM equipped with a Schottky field-emission gun (FEG) with  $C_s=1.0 \text{ mm}$  operated at  $200 \text{ kV}$ . Raman spectra were obtained with a Nomadic Raman Microscope (Bayspec Inc). The  $785 \text{ nm}$  line of a diode laser was used as the exciting radiation. The current density-voltage curves as well as the impedance spectra of the cells were measured with a four probe method using a multi-channel Versa STAT (Princeton Applied Research) at the operating temperatures ranging from  $700 \text{ }^\circ\text{C}$  to  $800 \text{ }^\circ\text{C}$ . During cell measurement, hydrogen or methane (with  $3 \text{ vol}\% \text{ H}_2\text{O}$ ) was used as fuel while cathode side was exposed to ambient air. Gas flow rate was controlled at  $40 \text{ sccm}$  by a precision volume flow controller (APEX, Alicat Scientific). The cell polarization resistance ( $R_p$ ) was determined from the difference between the low and high frequency intercepts of the impedance spectra with real axis in the Nyquist plot.

## 5.3 RESULTS AND DISCUSSION

The microstructure of half cell Ni-YSZ|YSZ with nano SDC catalyst layer on the internal gas diffusion channel, denoted as Ni-YSZ(SDC)|YSZ, is quantitatively analyzed

using 3D X-ray microscope combining with an in-house Matlab code. 3D X-ray microscope allows nondestructive virtual sectioning of the electrodes to reveal internal 3D morphology, advantageous to characterize the porous anode than the sectioning and 3D microstructure reconstructing using the conventional focused ion beam/scanning electron microscopy (FIB/SEM) method[111, 112]. 3D X-ray microscope can provide a much larger field of view than any 2D methods such as SEM and TEM. The spatial resolution of X-ray Computed Tomography (XCT) in this work is set as  $4.53\ \mu\text{m}$  to reconstruct the entire Ni-YSZ(SDC)|YSZ microstructure of its thickness dimension ( $\sim 744\ \mu\text{m}$ ). Figure 5.1 (a) and (b) display the 3D X-ray microscopy image and cross-section view for half cell Ni-YSZ(SDC)|YSZ. Figure 5.1 (c) shows the reconstructed 3D microstructure image for a domain with a size of  $400\ \mu\text{m} \times 400\ \mu\text{m} \times 650\ \mu\text{m}$ . The morphology is similar to that for the anode without SDC layer (Figure 5.02(a)). Figure 5.1 (d) shows the porosity distribution of the Ni-YSZ(SDC)|YSZ in the thickness direction, also similar to that of blank anode (Ni-YSZ without SDC catalyst layer) (Figure 5.2 (b)), indicating that the SDC layer has no adverse impact on gas diffusion. The tortuosity factor of pores in the thickness direction is calculated to be 1.47, similar to that for blank anode ( $\sim 1.3$ ) but much smaller than that for the conventional sponge-like anode (e.g., 3~10) [51]. The details about calculations of porosity and tortuosity can be found in our previous report[48]. Figure 5.1 (e) shows the distribution of a general field (e.g. fuel concentration) within the porous channels of the anode substrate, when the field is conducted along the thickness direction. As can be seen, the potential is smoothly evolved from the bottom side to the top side, indicating a low tortuosity for gas diffusion. The less tortuous anode substrates could create favorable conditions for the enhanced

heat and mass transfer and are of special interest in heterogeneous catalytic process determined by heat or mass transfer. The fluent gas delivery and reaction would alleviate the issues such as temperature gradients and the load response behavior during methane reforming process.

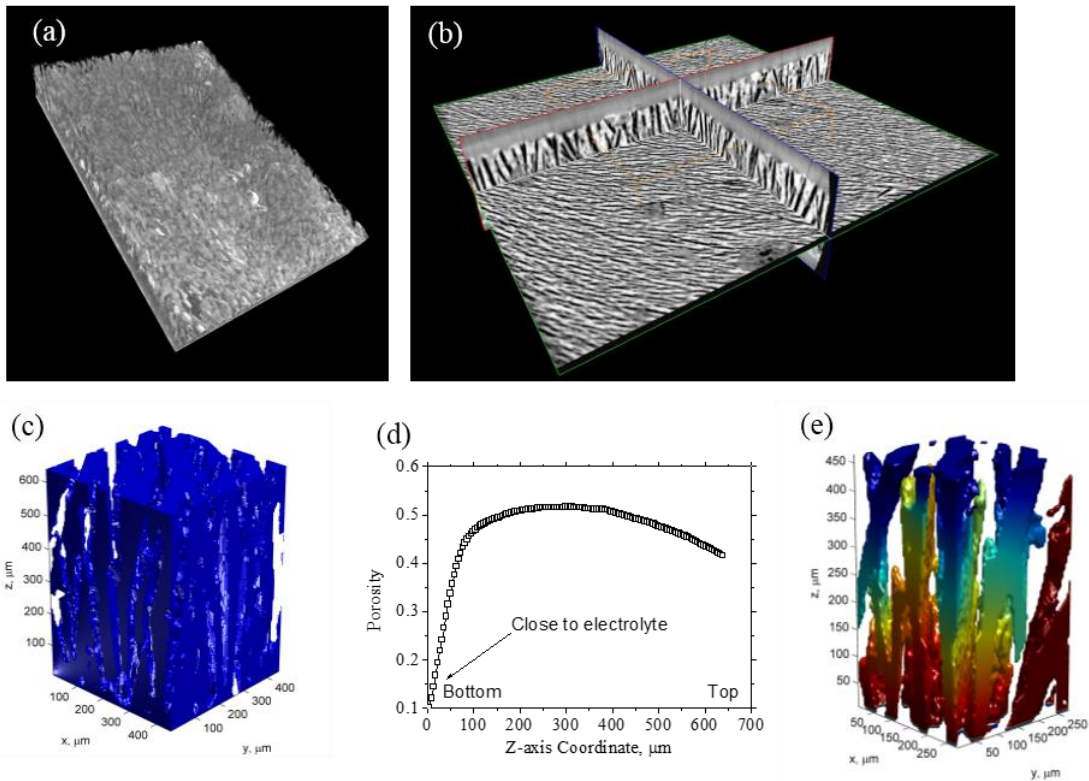


Figure 5. 1 (a) 3D X-ray microscopy image (with a dimension of 3.20mm\*3.80mm\*0.74 mm); (b) cross-sectional image; (c) reconstructed 3D microstructure, The blue/blank regions represent solid/pore phase; (d) porosity distribution of the porous Ni-YSZ(SDC)|YSZ; (e) Visualization of a general field within the porous channels of the Ni-YSZ(SDC)|YSZ, when the field is conducted along the thickness direction. Colors from red to blue proportionally represent the field potential from high to low.

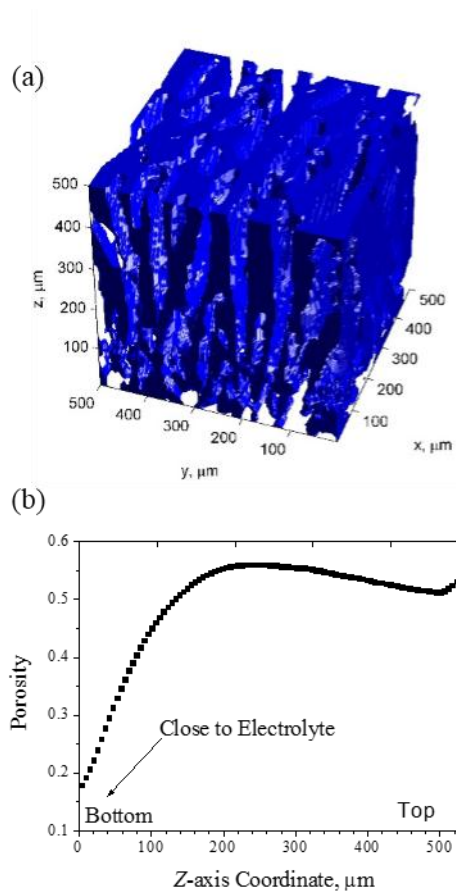


Figure 5. 2 (a) Reconstructed 3D microstructure of porous Ni-YSZ anode substrate. The blue/blank regions represent solid/pore phase; (b) Porosity distribution of the Ni-YSZ anode substrate along the thickness direction

Figure 5.3 displays the SEM images for the cell with the anode deposited with nanoscale SDC catalyst layer. The cell has a thick Ni-YSZ gas transport layer with straight open pores/channels, a thin dense electrolyte and thin porous LSM-YSZ cathode layer with thickness of round 600 μm, 30 μm and 40 μm, respectively, as shown in Figure 5.3 (a) and (b). The novel anode structure is expected to facilitate the heat and mass transfer, thus increasing the reforming efficiency of methane[113] and decreasing thermal stress[114]. After two infiltration cycles, SDC layer with thickness of ~400 nm has been deposited on the gas diffusion channel wall with a loading of approximately 4 wt% of the

anode, which normally can be obtained after 7 infiltration cycles for the sponge-like electrode[65]. The higher infiltration efficiency demonstrates the advantage of straight open electrodes, which could simplify the process and reduce cost. Figure 5.3 (c) and (d) show the images for area adjacent to the electrolyte. Compared with the anode without SDC layer (Figure 5.4), it can be seen that the anode particles in this area have been almost completely covered by SDC layer (thinner than that in bulk), which is very challenging to achieve for the conventional sponge-like electrodes due to high capillary force[115]. The thin nanoscale SDC catalyst layer in the effective working zone (about 10  $\mu\text{m}$  adjacent to the electrolyte[116, 117]) covers and protects anode, generating an ion-conducting network thus enlarging TPB length[35, 118]. Figure 5.3 (e) and (f) show the SEM images for the anode bulk away from the electrolyte (gas diffusion layer). As shown in Figure 5.3 (e) and (f), the width for mass transport channel is several tens of microns. In this area, the porous SDC catalyst layer with thickness of only several hundred nanometer, well attaching to the channel wall surface where mass transport and electrochemical reaction take place, is expected to have no adverse impact on mass transport, confirmed by the porosity distribution shown in Figure 5.1 (d) and Figure 5.2 (b) and similar tortuosity factors (1.47 and 1.3 for anode with and without SDC layer). The SDC catalyst layer in the bulk might not increase TPB length but may function as a protection layer for Ni-YSZ cermet anode from direct contacting with methane, thereby prevent coking upon direct oxidation of methane fuel.

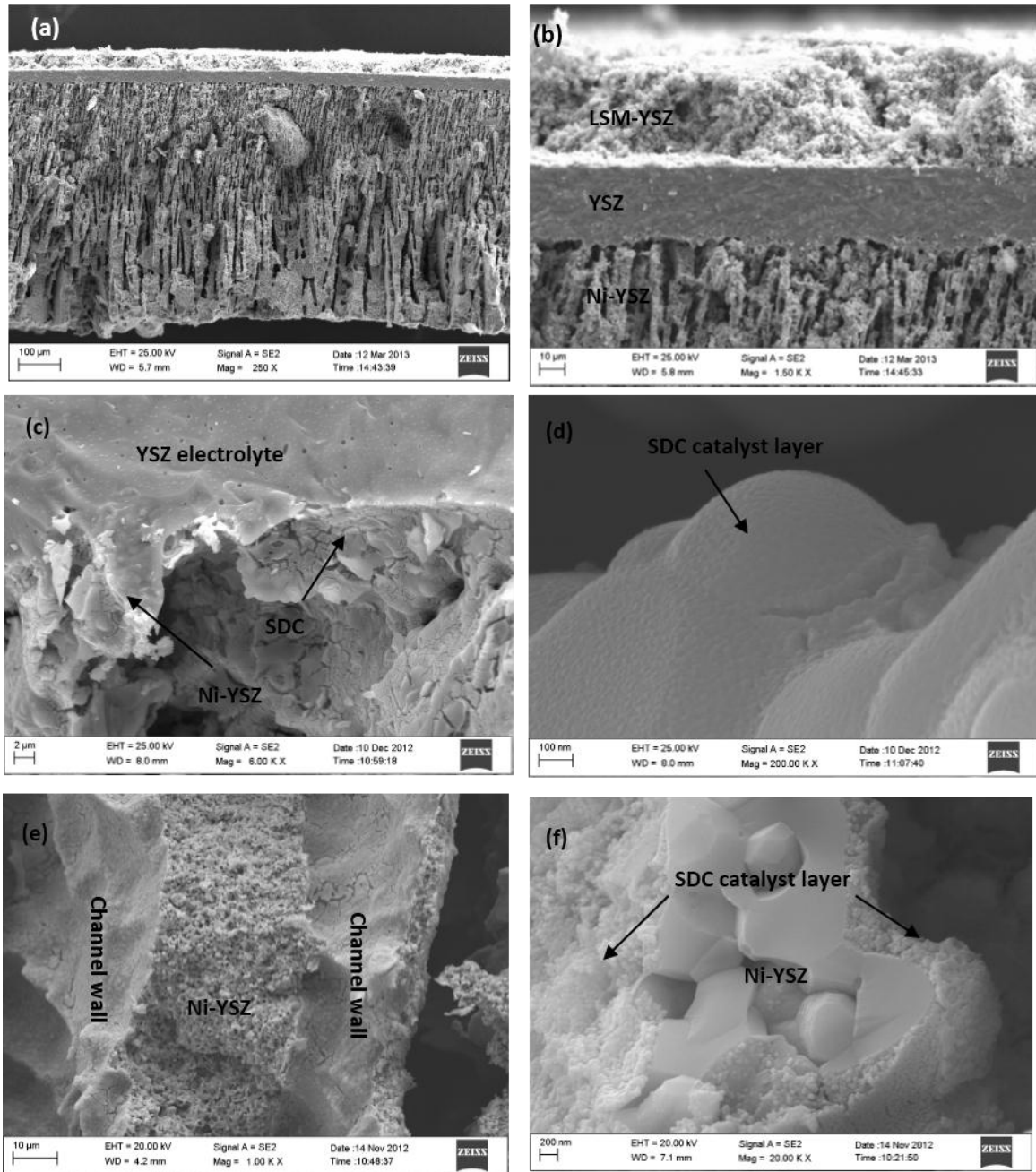


Figure 5. 3 SEM images of cell after measurement (a, b) and SDC-covered anode (c, d, e and f). The (c) and (d) show images for the area near electrolyte while (e) and (f) show images for the anode bulk.

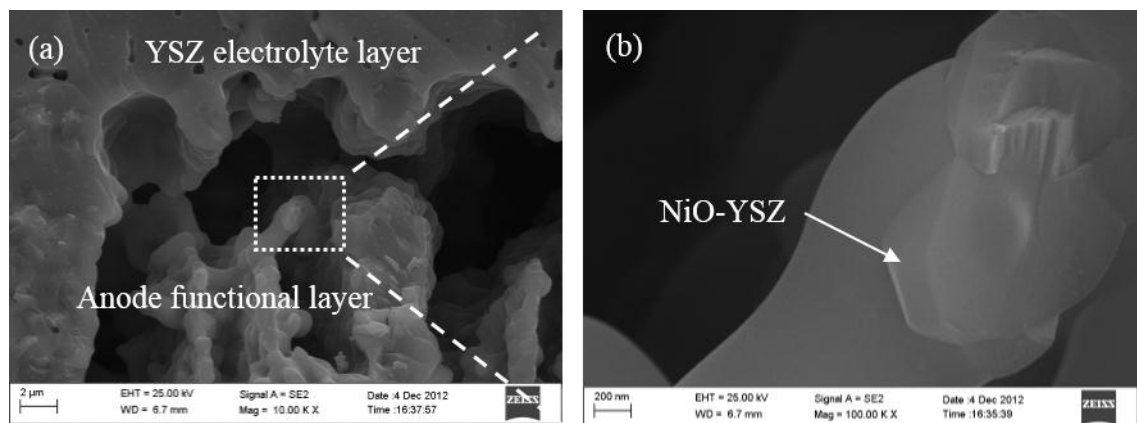


Figure 5. 4 SEM images for the anode (without SDC layer) adjacent to electrolyte (a) and (b) the NiO-YSZ particles in the square area in (a)

As shown in Figure 5.5 (a), the open circuit voltage (OCV) for the cell without SDC catalyst layer can be stabilized at 1.08 V when hydrogen was used as fuel but decreased dramatically to 0.84 V when the fuel was switched to CH<sub>4</sub>. However, the OCV can be recovered to original value when the fuel was switched back to H<sub>2</sub> again. The theoretical OCV is determined by the oxygen partial pressure difference between the anode and cathode. The lower OCV for Ni-YSZ anode using methane could be attributed to the different kinetics of reaction over the anode[108]. The anode site might be deactivated by adsorbed carbon species or the fuel composition might be changed. Normally, on porous Ni cermets with the conventional sponge-like microstructure, coking formation can lead to fracture of the Ni cermet anode in several minutes under open circuit condition[23, 26], due to the formation of nickel carbide (Ni<sub>3</sub>C) [119]. The cells in this study still maintain integrity after operating under open circuit voltage conditions for 12 h, indicating that the stress induced by coking, nickel carbide or temperature gradient might be released through the novel columnar anode structure. Figure 5.5 (b) shows the OCV curve for the

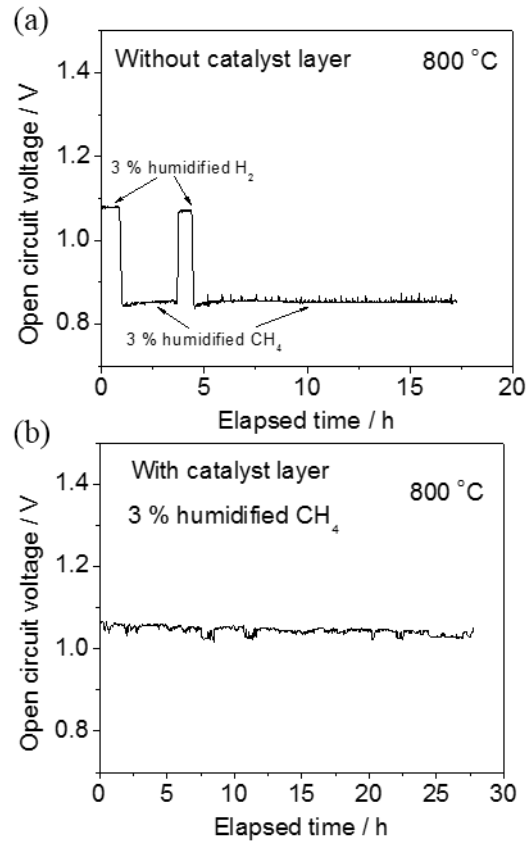


Figure 5. 5 Open circuit voltage (OCV) curve for the cell without catalyst layer (a) and with catalyst layer (b) when operated with either 3 vol% humidified H<sub>2</sub> or CH<sub>4</sub>.

cell with anode deposited with SDC catalyst layer when operated with 3 vol% H<sub>2</sub>O humidified methane. The OCV can be kept at around 1.05 V for 28 h at 800 °C, indicating that the anode displays good catalytic activity toward CH<sub>4</sub> and the nanoscale SDC layer can protect the anode from deactivating under open circuit conditions. There have been a few reports of OCV curves for SOFCs without and with SDC catalyst layer of the conventional Ni cermet anode since high current are normally required to avoid coking or failure of the Ni-based anode[25]. Liu et al have reported an OCV value of 1.17 V at 800 °C for Ni-YSZ anode[26]. However, their OCV was obtained by immediately measuring the *V-I* curve after operating the cell at a constant voltage load of 0.6 V. There was severe coking to cause the cell to crack after 10 min at 800 °C when their cell was

under OCV condition, behaving similarly to the dry-pressed cells we tested, indicating that the novel columnar anode structure and nanoscale SDC layer can significantly enhance the coking resistance of the conventional Ni cermet anode.

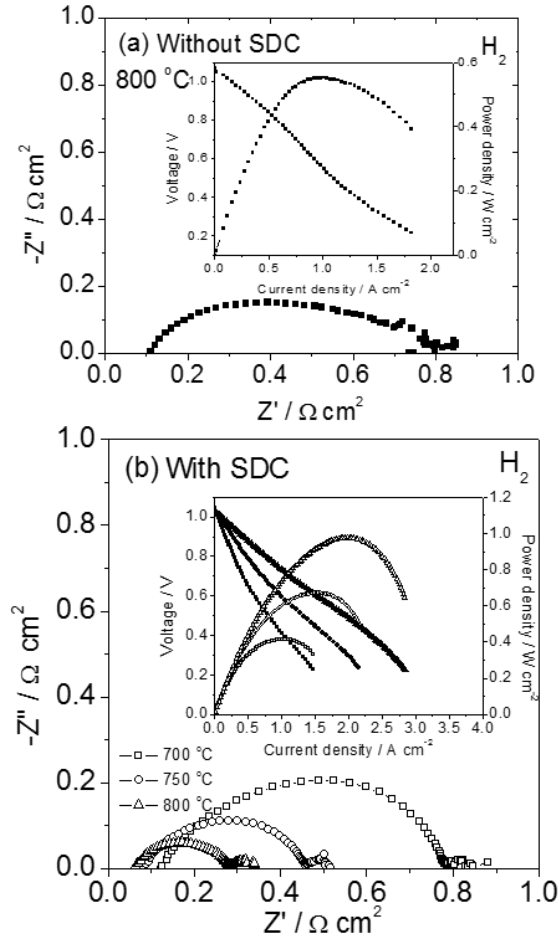


Figure 5. 6 Cell performance of cell without (a) and with (b) SDC catalyst layer. Inset in (a) are the IV and IP curves for cell at 800 °C. Inset in (b) are the  $I$ - $V$ - $P$  curves for cell at 700, 750 and 800 °C, respectively. The  $\text{H}_2$  flow was controlled at 40 sccm while the oxidant was ambient air.

Figure 5.6 shows the cell performance for the cell without (a) and with (b) SDC layer when using  $\text{H}_2$  as fuel and ambient air as oxidant. The cell shows almost doubled cell output with help of nano SDC layer. For example, the cell without SDC shows a peak power density of  $\sim 0.55 \text{ W cm}^{-2}$ , while the cell with SDC layer shows a peak power

density of  $\sim 1 \text{ W cm}^{-2}$  at  $800 \text{ }^\circ\text{C}$  using  $\text{H}_2$  as fuel and ambient air as oxidant. The total interfacial polarization resistance for cell without SDC layer is  $\sim 0.75 \text{ } \Omega\text{ cm}^2$ , while the one for cell with SDC layer is as low as  $\sim 0.26 \text{ } \Omega\text{ cm}^2$  at  $800 \text{ }^\circ\text{C}$  under open circuit conditions. The SDC in anode could increase the triple phase boundary (TPB) length[35, 118, 120], enhancing catalytic ability of anode for  $\text{H}_2$  electrochemical oxidation.

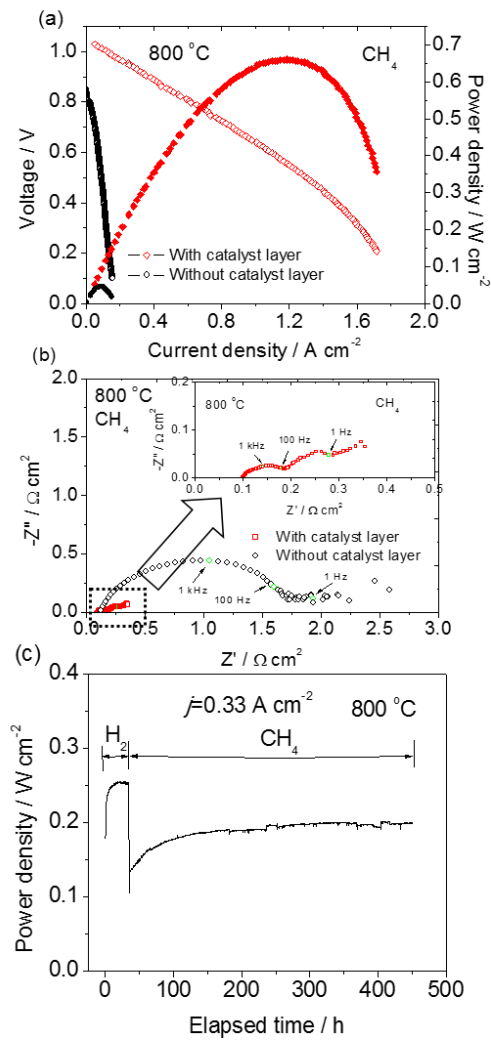


Figure 5. 7  $I$ - $V$  and  $I$ - $P$  curves (a), electrochemical impedance spectroscopy of cells with anode deposited with (red) and without (black) SDC catalyst layer (b) and stability measurement of cell with SDC catalyst layer when using  $\text{H}_2$  or methane as fuel (c).

Figure 5.7 shows the typical cell performance for the anode with and without SDC catalyst layer when using 3 vol% H<sub>2</sub>O humidified CH<sub>4</sub> at 800 °C. As shown in Figure 5.7 (a), the cells without the SDC catalyst layer only show a maximum power density ( $P_{max}$ ) of 0.045 Wcm<sup>-2</sup>, while the cells with the SDC catalyst layer show a  $P_{max}$  of as high as 0.65 Wcm<sup>-2</sup>, more than one order of magnitude improvement. Such a dramatic improvement can be attributed to the excellent catalytic activity of the SDC catalyst layer towards methane reforming[31], which can be further confirmed by the electrochemical impedance spectra measurement (as shown in Figure 5.7 (b)). The interfacial polarization resistance for the cells has been greatly decreased from ~2 Ω cm<sup>2</sup> to ~0.25 Ω cm<sup>2</sup> when the anode was deposited with the SDC catalyst layer. The nanoscale SDC catalyst layer can not only be effective in protecting Ni anode but also improve the catalytic activity of the anode for CH<sub>4</sub> reforming. The nanoscale SDC covered on the wall surface of the anode especially in the functional area (~10 μm adjacent to the electrolyte) will increase the anode TPB length, thus enhancing the electrode activity[33, 63], manifested by the doubled cell output when using H<sub>2</sub> as fuel for the cells with SDC catalyst layer compared with those without SDC layer (shown in Figure 5.6). When using methane as fuel, the cell performance is comparable to those reported for cells with Ni-based anode with noble metal catalyst layer, which is normally screen-printed on the outer surface of the anode. For example, Zhan et al applied Ru-CeO<sub>2</sub> as catalyst on Ni-YSZ anode to reform C<sub>8</sub>H<sub>18</sub>-air-CO<sub>2</sub> mixture using YSZ as electrolyte and LSM-YSZ as cathode. The  $P_{max}$  at 770 °C could be as high as 0.60 W cm<sup>-2</sup>[28]. Wang et al have prepared 3 % Ru-Al<sub>2</sub>O<sub>3</sub> catalyst layer on the surface of Ni-YSZ anode and the cell using YSZ as electrolyte and LSM-YSZ as cathode delivered a cell output of ~0.7 Wcm<sup>-2</sup> at 800 °C when using

methane and H<sub>2</sub>O mixture (volume ratio of 2:1) as fuel[29]. However, as mentioned by Zhan et al[28], the catalyst layer was expected to increase gas diffusion resistance and Ru is expensive, limiting the further commercialization with that design. In comparison, the novel design in this study avoids these two limitations and allows using non-precious metal catalyst that can be cost-effectively deposited on the internal gas diffusion channel surface of the anode. Figure 5.7 (c) shows the stability measurement for the cell with the SDC catalyst layer when operated with 3 vol% H<sub>2</sub>O humidified methane under a constant current density of 0.33 Acm<sup>-2</sup> at 800 °C for about 400 h. The cell shows much higher power output and better stability compared with the cell without the SDC catalyst layer in which the cell output power decreased rapidly to 0 under similar testing conditions. It has been reported that SDC nanoparticles on Ni-based composite not only decrease methane decomposition temperature but also increase methane conversion ratio[121], indicating that the deposited SDC layers are catalytically active for direct oxidation of methane. In addition, SDC coating layer has high oxygen storage capacity (OSC) and can potentially suppress coking at the anode by supplying more oxygen ions[18].

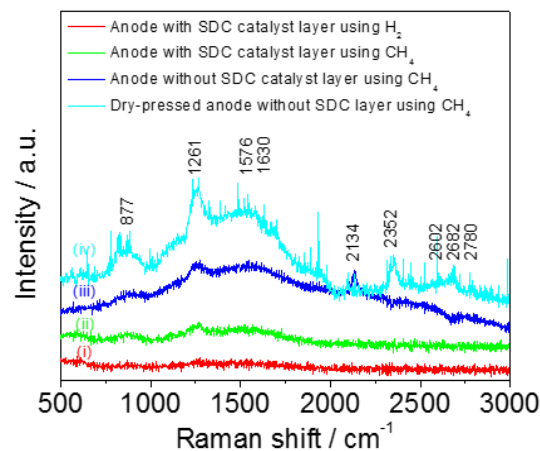


Figure 5.8 Raman spectra of different anodes after electrochemical measurement using either H<sub>2</sub> or CH<sub>4</sub> as fuel. The anodes in spectra (i), (ii) and (iii) were fabricated by freeze-drying tape-casting, while anode in spectrum (iv) was fabricated by dry-pressing.

Figure 5.8 displays the Raman spectra for different anode after the cell stability test using either H<sub>2</sub> or CH<sub>4</sub> as fuel. The anode deposited with the SDC catalyst layer shows similar spectra when using CH<sub>4</sub> as fuel (spectra ii) to that using H<sub>2</sub> (spectra i). The differences are the two weak peaks located at ~877 cm<sup>-1</sup> and ~1261 cm<sup>-1</sup>. The first peak could be assigned to ν(C-O-C), while the second peak could be assigned to ν(C-C) alicyclic or aliphatic chain vibrations[122]. It is shown that there were no bands at ~1576 cm<sup>-1</sup> or 1630 cm<sup>-1</sup>, which can be attributed to ν(C-C) aromatic ring chain vibration or graphite-like carbon[123-125]. However, the spectrum for freeze-drying tape-casted anode (iii) and dry-pressed anodes (iv) without the deposited SDC catalyst layer shows all the four peaks aforementioned after operation with methane. In addition, the peaks at 2100 cm<sup>-1</sup> indicates the vibration of ν(C≡C) [126, 127]. All other bands (between 2100-3000 cm<sup>-1</sup>) in spectra (iv) indicated the formation of various carbonaceous species such as olefinic, polyolefinic, aromatic, polyaromatic and pregraphite species[128]. Therefore, it can be concluded that the novel structured anode deposited with the SDC catalyst layer can effectively inhibit or remove carbon species when using methane as fuel.

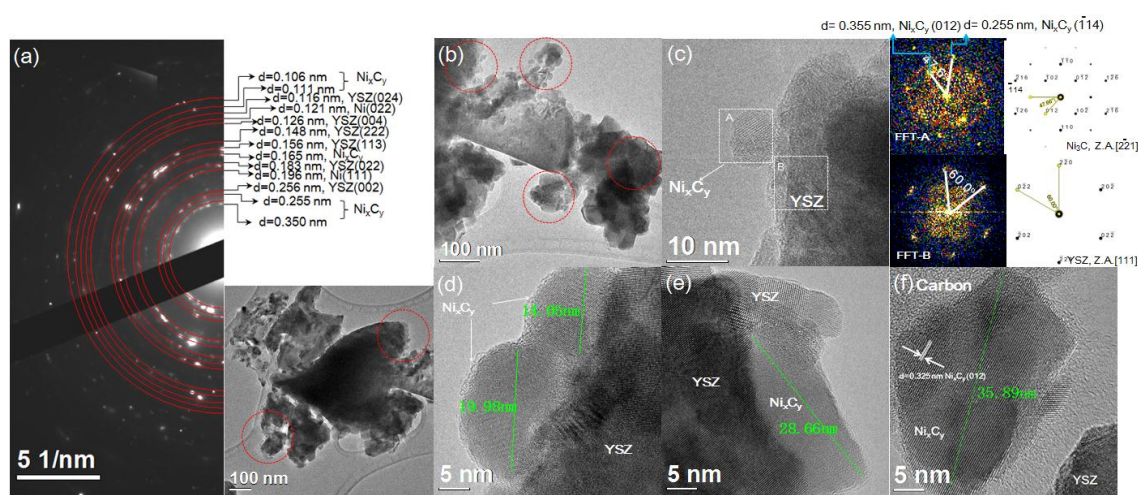


Figure 5. 9 (a) The SAED patterns for the blank Ni-YSZ anode (without SDC layer) after treatment with CH<sub>4</sub> (Inset is the Bright Field (BF) image of the area selected for the

SAED); (b) BF image of the anode aggregates (Red circled area showed small nano  $\text{Ni}_x\text{C}_y$  particles on the big YSZ particles); (c) HRTEM-image of one single crystalline  $\text{Ni}_x\text{C}_y$  particle sitting on YSZ particle and the corresponding Fast Fourier Transform (FFT) images for the selected A and B regions (Simulation of SAED using  $\text{Ni}_3\text{C}$  and YSZ were also shown for comparison); (d) and (e) HRTEM-images of other  $\text{Ni}_x\text{C}_y$  particles with different sizes sitting on the YSZ particle in different area; (f) HR-image for one single  $\text{Ni}_x\text{C}_y$  particle dropped from the YSZ particle.

Figure 5.9 shows the high resolution transmission electron microscopy (HRTEM) results for the Ni-YSZ anode without the SDC catalyst layer after operation with  $\text{CH}_4$ . Comparing the obtained selected area electron diffraction (SAED) data (Figure 5.9 (a)) with the Inorganic Crystal Structure Database (ICSD), the presence of three phases of  $\text{Ni}_3\text{C}$  (#17005), YSZ (#75316) and Ni (#41508) can be clearly identified. The formation of nickel carbide ( $\text{Ni}_x\text{C}_y$ ) phases can be further confirmed since the measured lattice spacing groups are mostly similar to those from the  $\text{Ni}_3\text{C}$  rather than YSZ or Ni. As nano-sized Ni particles have been experimentally found to be extruded from the YSZ lattice during the reduction of Ni-YSZ anode in  $\text{H}_2$  at high temperature[129], these nano Ni particles are susceptible to the formation of  $\text{Ni}_x\text{C}_y$  nano particles when directly exposed to  $\text{CH}_4$  (3%  $\text{H}_2\text{O}$ ) during the fuel cell operations. This is consistent to our results that the  $\text{Ni}_x\text{C}_y$  phases are mostly found in the range of 10~35 nm and sitting on the surface of the YSZ particles (Figure 5.9 (c-e)). However, some individual  $\text{Ni}_x\text{C}_y$  particles can also be found separately as shown in Figure 5.9 (f). The actual Ni/C ratio in the  $\text{Ni}_x\text{C}_y$  phases may be smaller than 3/1 as their d-spacing is larger than  $\text{Ni}_3\text{C}$ . The formation of such phases will introduce a sever expansion strain, which origins from the very large lattice volume changing from  $41.06 \text{ \AA}^3$  for Ni to  $231.95 \text{ \AA}^3$  for  $\text{Ni}_3\text{C}$ , accounting for the quick crack/decay (in less than half an hour) for the Ni cermet with traditional microstructure during the SOFC operation in  $\text{CH}_4$ [119, 130].

The unstable carbides caused reconstruction of Ni particles and subsequently partially decomposed into filamentous carbon[131]. It is generally accepted that the Ni catalyst particle is located at the filament head and has been carried away from the support surface during the coking growth process[132]. The catalyst is encapsulated with a layer of carbon, resulting in catalyst deactivation. In the steady-state coking growth period, the carbon atoms produced by the surface reaction diffuse rapidly through the surface carbide. A gradient is therefore maintained, causing migration of carbon atoms to the rear end of the catalyst particle where they segregate on the interface between filament and Ni particle[133, 134]. Therefore, for SOFC application, it is highly important to control or avoid the initial formation of nickel carbide in the anode substrate[134]. The OCV for the blank cell (without SDC layer) is low when using methane as fuel, indicating that the anode has been deactivated. However, compared with the cracked cells prepared by dry-pressing and reported by others[26, 119, 130], the cell is still in its integrity, demonstrating the formation of nickel carbide or filamentous carbon has been inhibited or can be removed by the efficient heat exchange and gas transport, resulting from the novel anode structure. However, the coking is still obvious from SEM image, as shown in Figure 5.10.

Figure 5.11 shows the SEM (a), Bright Field (BF) (b and c) and HRTEM (d, e) images for the Ni-YSZ anode with SDC catalyst layer after stability test with CH<sub>4</sub> for ~400 h. The structure of the Ni-YSZ anode with the SDC catalyst layer are kept well after the long term fuel cell operation in CH<sub>4</sub> (3% H<sub>2</sub>O) (Figure 5.11 (a)). The SDC nano particles are still well adhered to the Ni-YSZ anode (Figure 5.11 (b) and (c)). Coking can be rarely seen from the SEM image (Figure 5.11 (a)) compared with the anode without the SDC

layer (Figure 5.10) and EDX results (Figure 5.12), which is also consistent with the Raman results (Figure 5.8), indicating the impressive coking resistance of the Ni-YSZ anode with the nanoscale SDC layer upon operating in CH<sub>4</sub> (3% H<sub>2</sub>O).

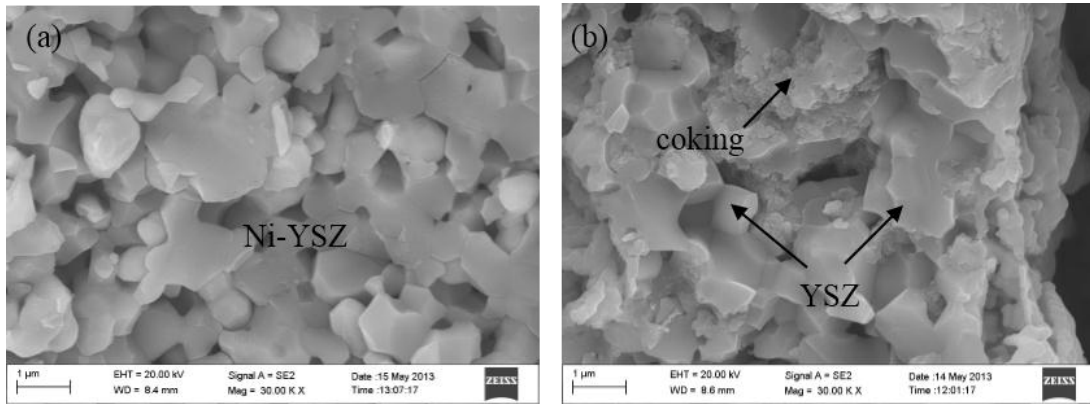


Figure 5. 10 (a) Cross-section SEM image for Ni-YSZ anode bulk with gas diffusion channel deposited without the SDC catalyst layer after operation on H<sub>2</sub>; (b) SEM image for anode without the SDC catalyst layer on channel wall after operation on CH<sub>4</sub>.

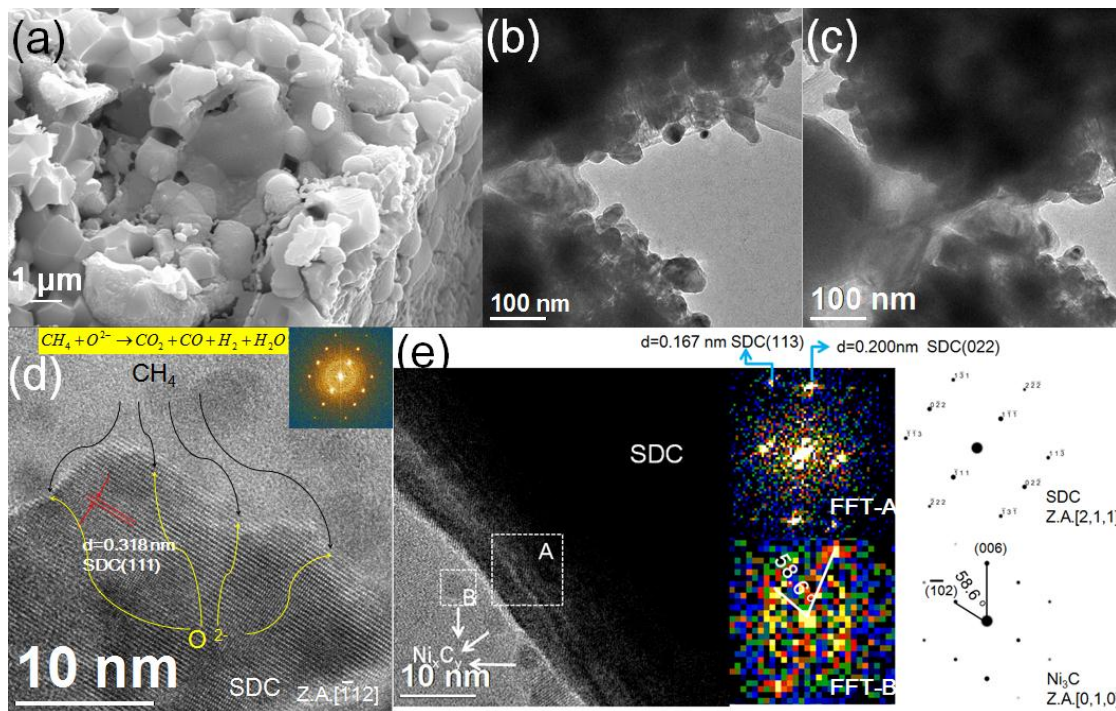


Figure 5. 11 The SEM (a), Bright Field (BF) image (b and c) of the Ni-YSZ anode with nanoscale SDC catalyst layer after operating in CH<sub>4</sub> (3% H<sub>2</sub>O) for 400 h, the HRTEM image of the surface of the SDC nano particles (d and e) (The corresponding FFT images and simulation SAED based on SDC and Ni<sub>3</sub>C in similar zone axis were also shown)

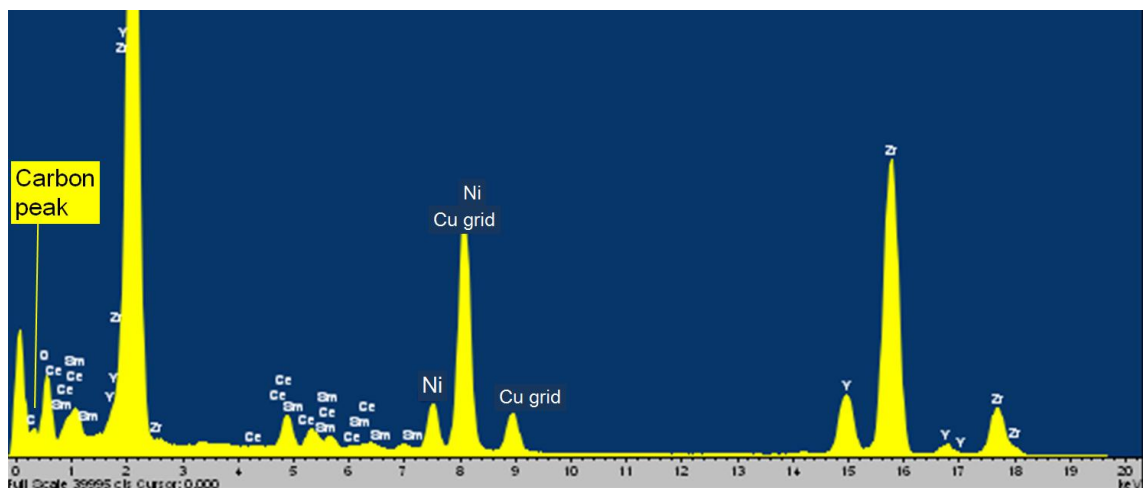
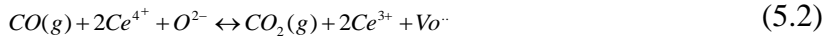
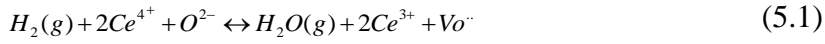


Figure 5. 12 EDX results for the Ni-YSZ anode with SDC layer after operation with CH<sub>4</sub> (3% H<sub>2</sub>O) at 800 °C for 400 h.

Most of the SDC and Ni surfaces kept good crystallinity and were clean without formation of large area of coke on their surface after the long term operation (Figure 5.11 (d)). The d-spacing of SDC (111) was slightly increased from 0.313 nm for SDC (unreduced) to 0.318 nm (after operation in CH<sub>4</sub>), indicating the O<sup>2-</sup> transportation in SDC during the application of the current had little influence on the original SDC lattice. For Ni-YSZ anode, the active sites towards CH<sub>4</sub> conversion were found to be near the Ni surface. The precipitation of nano-sized Ni particles from the YSZ lattice has been found to contribute significantly to the total catalytic activity towards methane partial oxidation[129]. Such nano Ni particles will be further poisoned to form Ni<sub>x</sub>C<sub>y</sub> intermediate phases as shown in our results due to their high catalytic ability towards CH<sub>4</sub> reforming (Figure 5.09 (c-f)). On the other side, *in-situ* study of the Ni-ceria catalyst layer during the fuel cell operation in CH<sub>4</sub> has revealed that the ceria surface is the active site towards the oxidation of CH<sub>4</sub>[135]. Therefore, in this study, SDC may first contact with methane and function as the active site towards methane reforming.

The nanoscale SDC catalyst layer can release and provide  $O^{2-}$  due to the reversible  $Ce^{3+}/Ce^{4+}$  transition, which is helpful in removal carbon.  $CO_2$  or  $H_2O$  would be a potential oxidant capable of filling in oxygen vacancies of ceria via the following reactions[136]:



The ceria surface covered with more  $H_2O$  and  $CO_2$  would lead to high O/C ratio, thus beneficial for carbon removal. Furthermore, the SDC layer would also function as a diffusion barrier to reduce the diffusion rate of steam or  $CO_2$  out of local Ni-YSZ anode and increase local ratio of O/C, enhancing the selectivity of internal reforming reactions toward  $H_2$  and  $CO$  and suppressing coke formation[28]. Moreover, only very small sizes  $Ni_xC_y$  (3-5 nm) nano particles were found on the TEM grid, as shown in Figure 5.11 (e) and Figure 5.13), rather than on any type of grains, which were different compared to the much larger  $Ni_xC_y$  particles on the YSZ grains from the blank Ni-YSZ anode (without the SDC catalyst layer). Such small  $Ni_xC_y$  particles were confirmed based on not only the TEM measurements but also SAED simulations (Figure 5.11 (e)). Thus, the deposition of the nanoscale SDC catalyst layer has successfully inhibited formation of large nickel carbide particles, resulting in significant improvement on the OCV and performance stability in the long term operation with  $CH_4$  (3 vol%  $H_2O$ ).

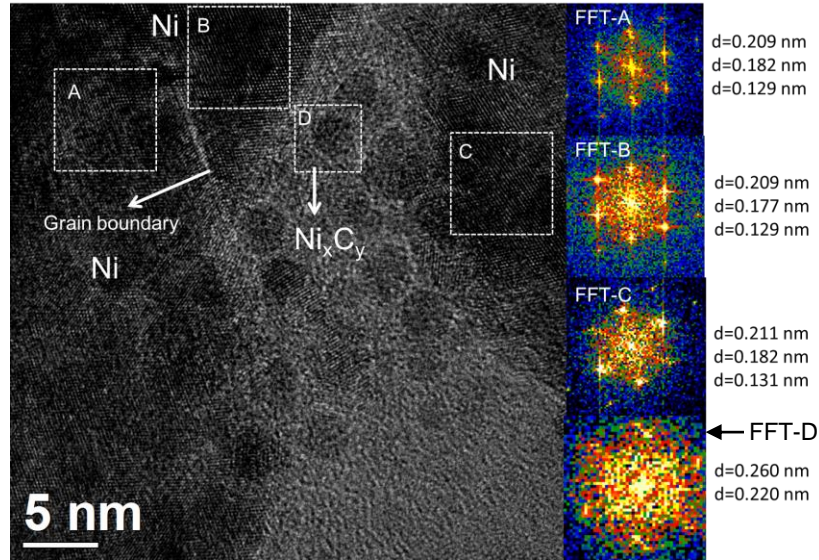


Figure 5. 13 (a) HRTEM image for the Ni particles zone from the Ni-YSZ anode with SDC as catalyst layer after operating in CH<sub>4</sub> (3% H<sub>2</sub>O) for 400 h. (FFT images and corresponding d-spacing in different area were also shown at left).

#### 5.4 CONCLUSIONS

In summary, we have demonstrated an innovative design for enhancing the coking resistance of the conventional nickel cermet SOFC anode. A nano SDC catalyst layer has been deposited onto the surface of internal hierarchically porous gas diffusion channel. Both the novel anode structure and nano SDC layer here could be helpful in removal the onset coking formation, thus limiting subsequent growth of nickel carbide and filamentous carbon, accounting for the excellent performance and structure stability. This novel anode design can broaden catalyst choice by infiltrating appropriate catalyst onto substrate internal diffusion channel surface, potentially capable of directly utilizing any kind of hydrocarbon fuels in SOFCs.

## FUTURE WORK

### 1. Solid Oxide Fuel Cells Fabricated by a Modified Freeze-tape Casting Process with Higher Infiltration Efficiency.

Infiltration /impregnation have been proven to be a valid method to modify the electrode microstructure. However, this method introduces additional process and sintering steps to achieve an optimal loading of catalyst, which definitely increases the preparations steps and cost. Further, infiltration of metal salt solution by capillary force could also be an issue for a thick electrode. The infiltrated catalyst can always be found in the area far away from the electrode/electrolyte interface, especially in the anode support cell. Therefore, the catalyst distribution in the anode is not homogeneous. We have measured the performance stability for the cell we prepared in Chapter 5 when using H<sub>2</sub> containing 50 ppm H<sub>2</sub>S as fuel. The cell output was continuously dropping with time. The reason can be probably attributed to the fact that most of catalyst is on the channel wall rather than the anode surface. The catalyst can not protect all the reaction sites.

Therefore, we propose a modified freeze-drying tape-casting technique to get catalyst homogeneously distributed on anode surface. The nitrate solution instead of water will be used as solvent in the slurry preparation. When the slurry is frozen on the freezing bed, the nitrate will be frozen together with anode particles. The distribution of catalyst is

expected to be more homogenous. The efficiency of infiltration will be improved. The cell will be evaluated on H<sub>2</sub>S.

## 2. Nanocrystals-Based Macroporous Materials Synthesized by Freeze-drying Combustion

Nanoscale materials have been widely developed as catalyst in energy conversion devices such as solid oxide fuel cells (SOFCs) since their advantageous catalytic properties, resulting from the high surface vacancy concentration and enhanced ionic and electronic conductivities, can facilitate the electrochemical reactions. Various wet chemical approaches have been developed to synthesize nanoparticles, such as hydrothermal, co-precipitation and liquid combustion. The powders prepared by aforementioned methods are usually composed of very small nanocrystals, which are beneficial for the sintering process to achieve higher density at lower sintering temperatures when they are used as electrolyte. The extreme fine and loose powder shows high surface area, which would facilitate the electrochemical reactions when they are applied as electrode/catalysts. However, stringent powder fabrication process limits its broad commercialization. Glycine-nitrate process (GNP) is one of the most commonly used liquid combustion approach in preparation of nanoscale materials/electrodes for SOFC applications. The metal nitrates dissolved in water are mixed at atomic scale and chelated by glycine, which are expected to guarantee the yield of desired stoichiometry networked structure. However, during the water removal by heating the solution, the stability of gel is an issue and some metal precipitates selectively, producing the agglomerate oxide powder mixture with some minor impurities. The impurities can be eliminated by high temperature calcination, however, which will result in a significant reduction in surface area and coarsening of the powders. Further, this approach deals

with water-based solution and can not be readily scaled up for large quantity preparations. Therefore, a liquid-free method that can produce large scale nanoparticles for various materials is of great significance.

Freezing has been developed as an effective path to build complex porous composite. In sea ice, the various impurities (salt, biological organisms, etc.) originally present in sea water are expelled from the forming ice and entrapped within tiny channels between the ice crystals. The impurities are all concentrated in the interstices between ice platelets. Inspired by this natural principle, we freeze nitrate solution and use ice as the template or cage to fix glycine-metal mixture, preventing aggregation/agglomeration and enhancing the complex stability. After sublimation of ice by freeze drying under vacuum, the metal/glycine mixtures are distributed in a macroporous scaffold whose microstructure is a negative replica of the ice. Afterwards, glycine acts as fuel during combustion reaction, being oxidized by the nitrate ions. Both the ice and glycine in this solid state combustion process helps in the formation of extremely fine oxide powder by impeding the internal complex/particles contact. Meanwhile, the powders are expected to show great homogeneous elemental distribution.

Ceria based materials have been considered as the most promising electrolyte for low temperature SOFC due to the higher oxygen ion conductivity at 400-600 °C compared to yttria-stabilized zirconia (YSZ). We propose to synthesize macroporous  $\text{Sm}_{0.2}\text{Ce}_{0.8}\text{O}_{1.9}$  (SDC) powders through solid state combustion by using ice/glycine as template. The solid state combustion method offers a simple way to produce porous solid powders directly in large scales. The as-prepared powders are extremely loose, making it easier to obtain thin films using co-pressing and co-sintering. Further, the very small nano-crystals

facilitate the sintering activity of SDC. The elemental distribution in ceria lattice is expected to be homogeneous and will be characterized by HRTEM analysis.

## REFERENCES

- [1] A.B. Stambouli, E. Traversa, *Renew Sus Energy Rev*, 6 (2002) 433-455.
- [2] R.P. O'Hayre, S.-W. Cha, W. Colella, F.B. Prinz, *Fuel Cell Fundamentals*, John Wiley & Sons New York, 2006.
- [3] L. Carrette, K.A. Friedrich, U. Stimming, *ChemPhysChem*, 1 (2000) 162-193.
- [4] L.J. Blomen, M.N. Mugerwa, *Fuel cell systems*, Springer, 1993.
- [5] B.C.H. Steele, A. Heinzl, *Nature*, 414 (1999) 345.
- [6] S.C. Singhal, *Solid State Ionics*, 152-153 (2002) 405-410.
- [7] S. Jiang, *J Mater Sci*, 43 (2008) 6799-6833.
- [8] O. Yamamoto, *Electrochimica Acta*, 45 (2000) 2423-2435.
- [9] S. Singhal, *High-temperature Solid Oxide Fuel Cells: Fundamentals, Design and Applications: Fundamentals, Design and Applications*, Elsevier, 2003.
- [10] S.H. Chan, K.A. Khor, Z.T. Xia, *J Power Sources*, 93 (2001) 130-140.
- [11] A. Leonide, V. Sonn, A. Weber, E. Ivers-Tiffée, *J. Electrochem. Soc.*, 155 (2008) B36-B41.
- [12] M. Granovskii, I. Dincer, M.A. Rosen, *J Power Sources*, 165 (2007) 307-314.
- [13] S. Wright, A. Pinkelman, *Int. J. Energy Res.*, 32 (2008) 612-622.
- [14] Y. Matsumura, T. Nakamori, *Appl. Catal. A: General*, 258 (2004) 107-114.

- [15] N.Q. Minh, *J. Am. Ceram. Soc.*, 76 (1993) 563-588.
- [16] M. Gong, X. Liu, J. Trembly, C. Johnson, *J. Power Sources*, 168 (2007) 289-298.
- [17] S. Zha, Z. Cheng, M. Liu, *J. Electrochem. Soc.*, 154 (2007) B201-B206.
- [18] E.P. Murray, T. Tsai, S.A. Barnett, *Nature*, 400 (1999) 649-651.
- [19] L. Yang, S. Wang, K. Blinn, M. Liu, Z. Liu, Z. Cheng, M. Liu, *Science*, 326 (2009) 126-129.
- [20] N. Laosiripojana, S. Assabumrungrat, *J. Power Sources*, 163 (2007) 943-951.
- [21] X.J. Chen, K.A. Khor, S.H. Chan, *Electrochem. Solid-State Lett.*, 8 (2005) A79-A82.
- [22] G.J. Offer, J. Mermelstein, E. Brightman, N.P. Brandon, *J. Am. Ceram. Soc.*, 92 (2009) 763-780.
- [23] S. McIntosh, R.J. Gorte, *Chem. Rev.*, 104 (2004) 4845-4866.
- [24] M. Pillai, Y. Lin, H. Zhu, R.J. Kee, S.A. Barnett, *J. Power Sources*, 195 (2010) 271-279.
- [25] Y. Lin, Z. Zhan, J. Liu, S.A. Barnett, *Solid State Ionics*, 176 (2005) 1827-1835.
- [26] J. Liu, S.A. Barnett, *Solid State Ionics*, 158 (2003) 11-16.
- [27] T. Horita, K. Yamaji, T. Kato, H. Kishimoto, Y. Xiong, N. Sakai, M.E. Brito, H. Yokokawa, *J. Power Sources*, 145 (2005) 133-138.
- [28] Z. Zhan, S.A. Barnett, *Science*, 308 (2005) 844-847.
- [29] W. Wang, R. Ran, Z. Shao, *Int. J. Hydrogen Energy*, 36 (2011) 755-764.
- [30] C. Sun, Z. Xie, C. Xia, H. Li, L. Chen, *Electrochem. Commun.*, 8 (2006) 833-838.
- [31] T. Suzuki, T. Yamaguchi, K. Hamamoto, Y. Fujishiro, M. Awano, N. Sammes, *Energ. Environ. Sci.*, 4 (2011) 940-943.
- [32] D. Ding, W. Zhu, J. Gao, C. Xia, *J. Power Sources*, 179 (2008) 177-185.

- [33] S.P. Yoon, J. Han, S.W. Nam, T.-H. Lim, S.-A. Hong, *J. Power Sources*, 136 (2004) 30-36.
- [34] H.C. Yao, Y.F.Y. Yao, *J. Catal.*, 86 (1984) 254-265.
- [35] D. Ding, X. Li, S.Y. Lai, K. Gerdes, M. Liu, *Energ. Environ. Sci.*, 7 (2014) 552-575.
- [36] C. Jin, C. Yang, F. Chen, *J. Membrane Sci.*, 363 (2010) 250-255.
- [37] C. Yang, C. Jin, F. Chen, *Electrochem. Commun.*, 12 (2010) 657-660.
- [38] T. Werber, *Solid State Ionics*, 42 (1990) 205-211.
- [39] T. Suzuki, Z. Hasan, Y. Funahashi, T. Yamaguchi, Y. Fujishiro, M. Awano, *Science*, 325 (2009) 852-855.
- [40] M.H.D. Othman, N. Droushiotis, Z. Wu, G. Kelsall, K. Li, *Adv. Mater.*, 23 (2011) 2480-2483.
- [41] J.-W. Kim, A.V. Virkar, K.-Z. Fung, K. Mehta, S.C. Singhal, *J. Electrochem. Soc.*, 146 (1999) 69-78.
- [42] S.W. Sofie, *J. Am. Ceram. Soc.*, 90 (2007) 2024-2031.
- [43] T.L. Cable, S.W. Sofie, *J. Power Sources*, 174 (2007) 221-227.
- [44] P. Gannon, S. Sofie, M. Deibert, R. Smith, V. Gorokhovskiy, *J. Appl. Electrochem.*, 39 (2009) 497-502.
- [45] M.D. Gross, J.M. Vohs, R.J. Gorte, *Electrochem. Solid-State Lett.*, 10 (2007) B65-B69.
- [46] Z. Wang, N. Zhang, J. Qiao, K. Sun, P. Xu, *Electrochem. Commun.*, 11 (2009) 1120-1123.
- [47] T.L. Cable, J.A. Setlock, S.C. Farmer, A.J. Eckel, *Int. J. Appl. Ceram. Tec.*, 8 (2011) 1-12.

- [48] Y. Chen, Y. Zhang, J. Baker, P. Majumdar, Z. Yang, M. Han, F. Chen, ACS Appl. Mater. Interfaces, 6 (2014) 5130-5136.
- [49] C.H. Yang, A. Coffin, F.L. Chen, Int. J. Hydrogen Energy, 35 (2010) 3221-3226.
- [50] S. Deville, E. Saiz, R.K. Nalla, A.P. Tomsia, Science, 311 (2006) 515-518.
- [51] Y. Zhang, C. Xia, M. Ni, Int. J. Hydrogen Energy, 37 (2012) 3392-3402.
- [52] Y.J. Leng, S.H. Chan, K.A. Khor, S.P. Jiang, Int. J. Hydrogen Energy, 29 (2004) 1025-1033.
- [53] W. Zhu, C. Xia, J. Fan, R. Peng, G. Meng, J. Power Sources, 160 (2006) 897-902.
- [54] L. Zhang, S.P. Jiang, W. Wang, Y. Zhang, J. Power Sources, 170 (2007) 55-60.
- [55] X. Xin, Z. Lü, X. Huang, X. Sha, Y. Zhang, W. Su, J. Power Sources, 159 (2006) 1158-1161.
- [56] L. Zhang, J. Gao, M. Liu, C. Xia, J. Alloy Compd., 482 (2009) 168-172.
- [57] Y. Chen, F. Chen, W. Wang, D. Ding, J. Gao, J. Power Sources, 196 (2011) 4987-4991.
- [58] A.V. Virkar, J. Chen, C.W. Tanner, J.-W. Kim, Solid State Ionics, 131 (2000) 189-198.
- [59] A.A. Asfour, AIChE J., 31 (1985) 523-523.
- [60] B.C.H. Steele, Solid State Ionics, 129 (2000) 95-110.
- [61] M.-Y. Cheng, D.-H. Hwang, H.-S. Sheu, B.-J. Hwang, J. Power Sources, 175 (2008) 137-144.
- [62] R. Tian, F. Zhao, F. Chen, C. Xia, Solid State Ionics, 192 (2011) 580-583.
- [63] D. Ding, B. Liu, Z. Zhu, S. Zhou, C. Xia, Solid State Ionics, 179 (2008) 896-899.

- [64] T. Yamaguchi, T. Suzuki, S. Shimizu, Y. Fujishiro, M. Awano, *J. Membrane Sci.*, 300 (2007) 45-50.
- [65] Y. Chen, J. Bunch, C. Jin, C. Yang, F. Chen, *J. Power Sources*, 204 (2012) 40-45.
- [66] Y. Chen, F. Chen, D. Ding, J. Gao, *Fuel Cells*, 11 (2011) 451-458.
- [67] A. Sarikaya, V. Petrovsky, F. Dogan, *Int. J. Hydrogen Energy*, 38 (2013) 10081-10091.
- [68] Y. Chen, J. Bunch, T. Li, Z. Mao, F. Chen, *J. Power Sources*, 213 (2012) 93-99.
- [69] Y. Chen, Q. Liu, Z. Yang, F. Chen, M. Han, *RSC Adv.*, 2 (2012) 12118-12121.
- [70] J.P. Terwilliger, S.F. Dizon, *Chem. Eng. Sci.*, 25 (1970) 1331-1349.
- [71] S.W. Sofie, F. Dogan, *J. Am. Ceram. Soc.*, 84 (2001) 1459-1464.
- [72] P. Wei, S. Sofie, Q. Zhang, A. Petric, *ECS Transactions*, 35 (2011) 379-383.
- [73] D.L. Sahagian, A.A. Prousevitch, *J. Volcan. Geothermal Res.*, 84 (1998) 173-196.
- [74] E.L. Cussler, *Diffusion: mass transfer in fluid systems*, Cambridge University Press, 2009.
- [75] Y.J. Leng, S.H. Chan, S.P. Jiang, K.A. Khor, *Solid State Ionics*, 170 (2004) 9-15.
- [76] Z. Shao, S.M. Haile, *Nature*, 431 (2004) 170-173.
- [77] C. Ding, H. Lin, K. Sato, K. Amezawa, T. Kawada, J. Mizusaki, T. Hashida, *J. Power Sources*, 195 (2010) 5487-5492.
- [78] Y.D. Zhen, A.I.Y. Tok, S.P. Jiang, F.Y.C. Boey, *J Power Sources*, 178 (2008) 69-74.
- [79] C. Ding, T. Hashida, *Energ. Environ. Sci.*, 3 (2010) 1729-1731.
- [80] W. Lai, S.M. Haile, *J. Am. Ceram. Soc.*, 88 (2005) 2979-2997.
- [81] S.P. Yoon, S.W. Nam, J. Han, T.-H. Lim, S.-A. Hong, S.-H. Hyun, *Solid State Ionics*, 166 (2004) 1-11.

- [82] Q.L. Liu, K.A. Khor, S.H. Chan, *J. Power Sources*, 161 (2006) 123-128.
- [83] J.M. Ralph, A.C. Schoeler, M. Krumpelt, *J Mater. Sci.*, 36 (2001) 1161-1172.
- [84] S. Jiang, *J. Solid State Electrochem.*, 11 (2007) 93-102.
- [85] T.Z. Sholklapper, H. Kurokawa, C.P. Jacobson, S.J. Visco, L.C. De Jonghe, *Nano Lett.*, 7 (2007) 2136-2141.
- [86] Z. Jiang, C. Xia, F. Chen, *Electrochim. Acta*, 55 (2010) 3595-3605.
- [87] A. Tsch öpe, R. Birringer, *J. Electroceram.*, 7 (2001) 169-177.
- [88] J. Van herle, T. Horita, T. Kawada, N. Sakai, H. Yokokawa, M. Dokiya, *J. Eur. Ceram. Soc.*, 16 (1996) 961-973.
- [89] D. Ding, X. Li, S.Y. Lai, K. Gerdes, M. Liu, *Energ. Environ. Sci.*, (2013).
- [90] H. Da, X. Liu, F. Zeng, J. Qian, T. Wu, Z. Zhan, *Sci. Rep.*, 2 (2012).
- [91] Z. Zhan, D.M. Bierschenk, J.S. Cronin, S.A. Barnett, *Energ. Environ. Sci.*, 4 (2011) 3951-3954.
- [92] L.A. Chick, L.R. Pederson, G.D. Maupin, J.L. Bates, L.E. Thomas, G.J. Exarhos, *Mater. Lett.*, 10 (1990) 6-12.
- [93] R.N. Basu, F. Tietz, E. Wessel, H.P. Buchkremer, D. St över, *Mater. Res. Bull.*, 39 (2004) 1335-1345.
- [94] N.P. Bansal, Z. Zhong, *J. Power Sources*, 158 (2006) 148-153.
- [95] C. Ratti, *J. Food Eng.*, 49 (2001) 311-319.
- [96] Y. Chen, Y. Zhang, J. Baker, P. Majumdar, Z. Yang, M. Han, F. Chen, *ACS Appl. Mater. Interfaces*, (2014).
- [97] C. Xia, M. Liu, *Solid State Ionics*, 144 (2001) 249-255.
- [98] L. Zhang, F. Chen, C. Xia, *Int. J. Hydrogen Energy*, 35 (2010) 13262-13270.

- [99] F. Zhao, Z. Wang, M. Liu, L. Zhang, C. Xia, F. Chen, J. Power Sources, 185 (2008) 13-18.
- [100] C. Xia, W. Rauch, F. Chen, M. Liu, Solid State Ionics, 149 (2002) 11-19.
- [101] Q. Liu, F. Chen, J. Nanosci. and Nanotech., 10 (2010) 4317-4321.
- [102] X.-M. Ge, S.-H. Chan, Q.-L. Liu, Q. Sun, Adv. Energy Mater., 2 (2012) 1156-1181.
- [103] P.I. Cowin, C.T.G. Petit, R. Lan, J.T.S. Irvine, S. Tao, Adv. Energy Mater., 1 (2011) 314-332.
- [104] L. Yang, S. Wang, K. Blinn, M. Liu, Z. Liu, Z. Cheng, M. Liu, Science, 326 (2009) 126-129.
- [105] J. Liu, S. Zhang, W. Wang, J. Gao, W. Liu, C. Chen, J. Power Sources, 217 (2012) 287-290.
- [106] W. Sangtongkitcharoen, S. Assabumrungrat, V. Pavarajarn, N. Laosiripojana, P. Praserthdam, J. Power Sources, 142 (2005) 75-80.
- [107] Y. Huang, R.I. Dass, Z. Xing, J.B. Goodenough, Science, 312 (2006) 254-257.
- [108] W. Wang, C. Su, Y. Wu, R. Ran, Z. Shao, Chem. Rev., 113 (2013) 8104-8151.
- [109] F. Zhao, R. Peng, C. Xia, Mater. Res. Bull., 43 (2008) 370-376.
- [110] D. Ding, M. Liu, Z. Liu, X. Li, K. Blinn, X. Zhu, M. Liu, Adv. Energy Mater., 3 (2013) 1149-1154.
- [111] J.R. Wilson, J.S. Cronin, A.T. Duong, S. Rukes, H.-Y. Chen, K. Thornton, D.R. Mumm, S. Barnett, J. Power Sources, 195 (2010) 1829-1840.
- [112] J.R. Wilson, J.S. Cronin, S.A. Barnett, Scripta Mater., 65 (2011) 67-72.
- [113] J. Meusinger, E. Riensche, U. Stimming, J. Power Sources, 71 (1998) 315-320.
- [114] P.-W. Li, M.K. Chyu, J. Power Sources, 124 (2003) 487-498.

- [115] S. Park, R.J. Gorte, J.M. Vohs, J. Electrochem. Soc., 148 (2001) A443-A447.
- [116] M. Brown, S. Primdahl, M. Mogensen, J. Electrochem. Soc., 147 (2000) 475-485.
- [117] Y. Zhang, C. Xia, Electrochim. Acta, 56 (2011) 4763-4769.
- [118] Z. Liu, B. Liu, D. Ding, M. Liu, F. Chen, C. Xia, J. Power Sources, 237 (2013) 243-259.
- [119] H. Kim, S. Park, J.M. Vohs, R.J. Gorte, J. Electrochem. Soc., 148 (2001) A693-A695.
- [120] S.P. Jiang, Mater. Sci. Eng.: A, 418 (2006) 199-210.
- [121] B. Liu, Z. Liu, S. Wang, C. Xia, M. Xie, Z. Cheng, Y. Li, Int. J. Hydrogen Energy, 37 (2012) 8354-8359.
- [122] S.A. Overman, G.J. Thomas, Biochem., 38 (1999) 4018-4027.
- [123] D. Eisenbach, E. Gallei, J. Catal., 56 (1979) 377-389.
- [124] J. Li, G. Xiong, Z. Feng, Z. Liu, Q. Xin, C. Li, Microporous and Mesoporous Mater., 39 (2000) 275-280.
- [125] K.S. Blinn, H. Abernathy, X. Li, M. Liu, L.A. Bottomley, M. Liu, Energ. Environ. Sci., 5 (2012) 7913-7917.
- [126] M.L. Patterson, M.J. Weaver, J. Phy. Chem., 89 (1985) 5046-5051.
- [127] H. Feilchenfeld, M.J. Weaver, J. Phy. Chem., 93 (1989) 4276-4282.
- [128] C. Li, P.C. Stair, Coke formation in zeolites studied by a new technique: ultraviolet resonance Raman spectroscopy, in: S.-K.I. Hakze Chon, U. Young Sun (Eds.) Studies in Surface Science and Catalysis, Elsevier, 1997, pp. 599-606.
- [129] D.L. King, J.J. Strohm, H.-S. Roh, C. Wang, Y.-H. Chin, Y. Wang, Y. Lin, R. Rozmiarek, P. Singh, J. Catal., 258 (2008) 356-365.

- [130] H. Kim, C. Lu, W.L. Worrell, J.M. Vohs, R.J. Gorte, J. Electrochem. Soc., 149 (2002) A247-A250.
- [131] C.M. Chun, J.D. Mumford, T.A. Ramanarayanan, J. Electrochem. Soc., 147 (2000) 3680-3686.
- [132] R.T.K. Baker, M.A. Barber, P.S. Harris, F.S. Feates, R.J. Waite, J. Catal, 26 (1972) 51-62.
- [133] I. Alstrup, J. Catal., 109 (1988) 241-251.
- [134] A. Lanzini, P. Leone, C. Guerra, F. Smeacetto, N. Brandon, M. Santarelli, Chem. Eng. J., 220 (2013) 254-263.
- [135] V. Papaefthimiou, M. Shishkin, D.K. Niakolas, M. Athanasiou, Y.T. Law, R. Arrigo, D. Teschner, M. Hävecker, A. Knop-Gericke, R. Schlögl, T. Ziegler, S.G. Neophytides, S. Zafeiratos, Adv. Energy Mater., 3 (2013) 762-769.
- [136] F. Sadi, D. Duprez, F. Gérard, A. Miloudi, J. Catal., 213 (2003) 226-234.